Neutral Current Electroweak Interactions and the Structure of the Proton

Harald Peter Wilhelm Jochen Borner
The Queen's College

Department of Nuclear Physics
University of Oxford

Thesis submitted for the degree of Doctor of Philosophy
in the University of Oxford

Michaelmas 1990

Neutral Current Electroweak Interactions and the Structure of the Proton

Harald Peter Wilhelm Jochen Borner
The Queen's College

Department of Nuclear Physics
University of Oxford

Abstract

In this thesis we investigate the scattering of neutrinos and antineutrinos off free protons in the deep inelastic region via the neutral weak current. In the BEBC experiment, a hybrid detector consisting of a large liquid hydrogen bubble chamber and electronic counters for muon and hadron identification, has been exposed to the CERN wide band beam of neutrinos with energies up to 300 GeV. The detector provides the possibility to discriminate efficiently between hadron-induced and neutrino-induced muonless events.

We are interested in the structure of the proton as it is resolved by the neutral carrier Z^0 of the electroweak force. The kinematical scaling variable $x_{(Bj)}$ that represents information about the proton structure cannot be reconstructed in an experiment using a hydrogen target. Thus the $x_{(Bj)}$ dependence of the cross section for free protons has so far not been accessible. We construct a method that links the measurable distribution in a new variable w, that incorporates the hadronic momentum longitudinal and transverse to the beam, to the one in $x_{(Bj)}$, in a model-independent way. It is shown that even with the statistics of about a thousand events it is possible to recover the $x_{(Bj)}$ dependence fo the neutrino proton cross-section with appreciable precision.

This method is then applied to the data that consists of 2200 neutrino and 1060 antineutrino neutral current events, after correcting for various backgrounds and cuts. We observe a neutral current proton structure that is consistent with the notion of parton universality. The results are compared to two other investigations which employ isoscalar heavy targets, and we find agreement in as far as they are comparable.

Furthermore we study the connection between the neutral current structure functions and distributions in the hadronic scaling variable w. It is found that they are related by simple formulae which do not incorporate any dependence on further kinematical variables, in the scaling approximation. We advocate the use of the w dependence of the neutral current cross section as an important piece of information that can provide access to some quantities that are measured only indirectly in charged current and electromagnetic scattering, and to the behaviour of the structure functions at small values of their argument.

Thesis submitted for the degree of Doctor of Philosophy
in the University of Oxford

Michaelmas 1990

for my parents

So bleibt die einfache Tatsache der Übereinstimmung der Denkgesetze mit den Naturgesetzen als ein ewig wunderbares Geheimnis bestehen, dessen Reiz den forschenden Menschengeist unaufhörlich zu Bemühungen antreiben wird, seinen Inhalt der Anschauung näherzubringen. (M. Planck) [1]

[1] 'Thus the simple fact of the correspondence between the laws of thinking and the laws of Nature remains an eternal miraculous secret, which will incessantly stimulate our enquiring mind to strive to bring its content closer to our visualisation and perception.'

Acknowledgements

It is a great pleasure to thank my supervisor, Dr. Gerald Myatt, for his guidance and encouragement, with which he introduced me to the secrets of particle physics, and to the beauty of multinational large scale experiments. Having this patient teacher as a constant source of sound advice during my years in Oxford and at CERN in Geneva has been an invaluable experience.

For the opportunity to work in this Department, and for his interest in my work, I would like to thank Prof. D. H. Perkins, who let me participate in two experiments, DELPHI and BEBC, that have been at the adolescent and the mature stages of their long 'life', respectively. I always enjoyed his demonstrations of how lively (to say the least) a departmental seminar can be.

I am grateful for generous support from the 'Studienstiftung des deutschen Volkes' in form of a 'Doktor anden stipendium', and from a 'European Florey Studentship' at 'The Queen's College', Oxford. Without these scholarships I could not have met the costs of the studies here.

The research presented in this thesis would have been impossible without the expertise of many members of the staff. As more stimulating and valuable even than their competent help, I shall remember the friendly, informal and cooperative atmosphere of the whole department. I thus feel indebted to everybody under the roof of 1, Keble Road, for receiving and assisting a foreigner with such kind openness.

For numerous helpful discussions on electronics, software and physics, my thanks go to John Bibby, Peter Ratoff, Craig Buttar, Peter Renton, Alan Segar, Dusan Radojicic, Wolfgang Wittek, Per Olof Hulth, and all others who must remain unmentioned due to the lack of space. John, Nick, Ian and Adib, backbone of our computing service, gave innumerable hints to make the computer do what I wanted it to do.

The daily life in the office and in or around Oxford would not have been the colourful experience that it was without the many friends who shared the pleasant as well as the tough periods. Thank you Tom, Jerry, Clifton, Slimane, Hans-Peter, James, Phil, Nigel, Gedtan, Andrew, Christine, Jawn, Simon, Guy, for cheering me up with your jokes and mischieves. I hope I was able to return some of the pleasure to you. Special thanks go to Emilios, Christoph, and Diana, who gave all kind of selfless help in the final stages of preparing this thesis. College life became valuable due to Peter, Sophie, Rachel, Heather, Juan, Barbara, Jean-Pierre, Sergej, Nancy, Dimitris and Javid. I am very happy that my long term camarades kept our friendship alive, thank you for all your lovely efforts Reinhard, Anke, Stephan, Jochen, Jürgen, and of course, Iveta.

It is impossible to phrase with so few words what the unrelenting support of my parents meant for me during this time. Without their love and participation from 'overseas' the following pages would not have been written.

Preface

The deep inelastic scattering of neutrinos and antineutrinos off a proton can provide insights into its structure as probed by the charged and neutral electroweak current. We investigate here the interaction of (anti)neutrinos with protons as mediated by the *neutral* carrier of the weak force, the intermediate vector boson Z^0. The question whether the proton structure is independent of whether it is resolved by the neutral weak, charged weak, or electromagnetic current ('parton universality'), is of crucial importance to our understanding and evaluating of subnuclear phenomena. Whereas this independence is supported so far by numerous experiments comparing the charged weak and electromagnetic proton structure, very little evidence exists as to the neutral current sector. In particular, the proton structure could not be extracted for protons which are not *bound* into a nuclear environment. The construction of a method that enables this structure of *free* protons to be measured, as well as an analysis based on it, is the subject of this thesis.

In chapter 1 we present briefly the more important experimental developments that led to the description of the neutrino as a massless neutral particle, interacting with matter only via the weak force, and to the gauge theory of weak interactions. The unified electroweak theory is outlined and we focus on the neutral current sector that predicts the coupling of the Z^0 boson to matter.

Chapter 2 introduces the BEBC experiment at CERN where the 400 GeV proton synchrotron has been used to generate an intense neutrino beam with a wide-band energy spectrum. The various parts of the hybrid detector are explained with view to their relevance for the later analysis.

A new method that aims at extracting the (anti)neutrino NC $x_{(Bj)}$ distribution is offered in chapter 3. We introduce a kinematical scaling variable w that is related to $x_{(Bj)}$ and $y_{(Bj)}$ in a simple way in the Bjorken limit and investigate the connection between the $x_{(Bj)}$ and w distributions of the cross section. It is shown that the measurement of the w distribution and the knowledge of the helicity structure of the NC interaction is sufficient for the reconstruction of the NC $x_{(Bj)}$ distributions, which are determined uniquely via the analytic solution of an integral equation. The fact that the measured distributions are subject to the cuts imposed in an analysis turns out to be advantageous in this context. We demonstrate the applicablity of the method with simulated events in BEBC.

Chapter 4 investigates more closely which direct connections exist between the $x_{(Bj)}$- and the w-distributions when the helicity structure of the neutral current, as it follows from very general principles like the Lorentz invariance of the cross section, is assumed to hold. We shed some light on the application of crossing symmetry to the neutral current channel and find some useful consequences in relation with the use of the w distribution.

An analysis of data from the BEBC Hydrogen experiment is contained in chapter 5. The isolation of a largely pure neutral current event sample is possible through the combination of the bubble chamber with electronic detectors that provide a timing structure with narrow timeslots, as well as an efficient identification of hadrons and muons entering or leaving the bubble chamber. Thus the two main backgrounds, neutral hadron induced events, and misidentified charged current events, can be accurately evaluated and corrected for. The resolution in w allows a meaningful measurement of the w distributions from the data.

Finally, the measured w distributions are used in chapter 6 as input to the method we presented, and $x_{(Bj)}$ distributions of free protons as probed by the weak neutral current are obtained. We compare them to the few existing measurements and comment on the degree to which these different results can be compared. We close with the interpretation of our result in the framework of a parton picture of the proton. The conclusions in chapter 7 contain some comments about the further prospects for the investigation of the NC channel.

Contents

Chapter 1

Electroweak Theory of Neutral Currents

1.1 Weak Interactions and Neutrinos

'I have come upon a desperate way out regarding the [...] continuous β-spectrum, in order to save the 'alternation law' of statistics and the energy law. To wit, the possibility that there could exist in the nucleus electrically neutral particles ... ' (W. Pauli, 1930)

'Bohr ... (well, you know that he absolutely does not like this chargeless, massless little thing!) thinks that continuous β-spectra is compensated by the emmition of gravitational waves which play the role of neutrino but are much more physical things. (G. Gamow, 1934)

1.1.1 Pauli's 'neutron'

The history of weak interactions is very closely tied to the properties of processes involving neutrinos. Electron emitting nuclear processes (called β^--decays) like $He^6 \to Li^6 + e^-$ had shown a continuous distribution of electron momenta, a fact that was incompatible with a decay described by two-body kinematics, in which a monoenergetic electron should emerge. Furthermore, in cases where the recoil nucleus was observable, its momentum was not always coplanar with that of the electron. Three excape routes, none of which was welcome by the community, emerged:

- Energy-momentum conservation does not always hold in nuclear processes

- The nuclear states (prior to the decay) are not discrete
- A third, unseen particle is emitted along with the electron

The last alternative is Pauli's postulate [1] of the existence of a light, neutral particle inside the nucleus, which at the time was still thought of as consisting of protons and electrons. Thus his 'neutron' (the name 'neutrino' was not introduced until 1933 [2]) was supposed to be bound to nuclear matter and had to interact electromagnetically, which led Pauli to propose it to possess a magnetic dipole moment.

It was not until the discovery of (what is now called) the neutron by Chadwick in 1932 that further advances were possible. With the existence of the neutron the neutrino no longer had to play a role in explaining the constitution of the nucleus. Secondly, nuclear β-decay could now be viewed as the transformation of a neutron into a proton under emission of an electron and a neutrino:

$$n \longrightarrow p + e^- + \overline{\nu} \tag{1.1}$$

Theoretically it was soon realised that the language of quantised fields provided a suitable description of the process. Here the neutrino need no longer be viewed as existing inside the nucleus prior to the interaction, but as being created out of the vacuum in the interaction process itself. The same applies to the electron (actually, although it was a matter of convention at the time, conservation of electron number tells us that the emitted neutral particle is an antineutrino, so that the interaction operator annihilates a neutrino and creates an electron).

1.1.2 Fermi Theory and its Extensions

Inspired by the field theoretical description of the Compton scattering process, Fermi proposed [3] a theory for nuclear β-decay that was modelled in close analogy to quantum electrodynamics, where the interaction of charged matter with light was described by an operator $j_\mu(x)A^\mu(x)$. The electron probability current operator j_μ couples to the electromagnetic field A^μ resulting in the possibility of emission and absorption of light quanta by electrons. Fermi replaced A^μ by the Lorentz invariant bilinear operator $\bar{e}\gamma_\mu\nu$, where e, ν are second quantised Dirac bispinors for the electron and neutrino fields, $\bar{e} = e^\dagger\gamma_0$, and the γ_μ span a four dimensional matrix representation of the Dirac-Clifford algebra $\{\gamma_\mu, \gamma_\nu\} = 2g_{\mu\nu}$. [1] The matter current was assumed to be an analogue of the static, non-relativistic electromagnetic case, where $j_0 = \rho = e\delta(\vec{x} - \vec{x}_0)$, and took the form $G_F\tau_\pm\delta(\vec{x} - \vec{x}_0)$, with the dimensionful Fermi coupling constant G_F and with the isospin raising/lowering operators $\tau_\pm$ to account for the transition of a neutron into a proton or vice versa, which Heisenberg had introduced for his theory of nuclear forces [4]. Thus the Fermi interaction was given by

$$\mathcal{L}_{int} = G_F[\tau_+\bar{e}\gamma_\mu\nu + \tau_-\bar{\nu}\gamma_\mu e] \tag{1.2}$$

where all fields are evaluated at the same spacetime point $(\vec{x}_0, t)$. The reason for modelling the interaction as pointlike was the extremely short range of the weak force. The Hamiltonian acts on nucleon wave functions in the two dimensional isospin space spanned by the proton and the neutron. The second term in (1.2) is responsible for positron emission (β^+-radioactivity) processes that had indeed been observed by Joliot and Curie, as well as for antineutrino-induced β^+ decay which later provided the first direct experimental evidence for the existence of (anti)neutrinos in 1956 [7].

Immediate fruits arising from the Fermi theory were the possibility to calculate rates for other processes related to β-decay such as electron capture: $e^- + p \longrightarrow n + \nu$ [5]. The ocurrence of such a process was a prediction of the theory which was subsequently confirmed in an experiment by Alvarez [6].

[1] We employ the metric $g^{00} = 1, g^{11} = g^{22} = g^{33} = -1$

In the two years after Fermi's proposal, it became generally accepted that Dirac fields can be used even for the heavy nucleons. This paved the way for the first current-current form of the weak interaction Hamiltonian in which we find a product of nucleonic and electronic quantum transition currents. By then it was obvious that the most general description should contain all the possible bilinear covariants of von Neumann in addition to the Lorentz vector $\Gamma_V = \gamma_\mu$:

$$\mathcal{L}_{int} = \sum_i g_i \, (\bar{p}\Gamma_i n) \, (\bar{e}\Gamma_i \nu) \;+\; \text{hermitian conjugate}, \; i = S, P, V, A, T \tag{1.3}$$

$$\Gamma_S = 1_4, \;\; \Gamma_P = \gamma_5, \;\; \Gamma_A = \gamma_\mu\gamma_5, \;\; \Gamma_T = \sigma_{\mu\nu}. \tag{1.4}$$

where $\sigma_{\mu\nu} = \frac{i}{2}[\gamma_\mu, \gamma_\nu]$. Of the couplings g_i the Fermi constant G_F corresponds to g_V. The scalar (S) and vector (V) parts give rise to the angular momentum conserving ('Fermi') transitions present in the original theory, whereas the axial (A) and tensor (T) parts correspond to ('Gamow-Teller') transitions in which the angular momentum of the nucleon changes by one unit. The question with which proportion each of the operators S,V,A and T takes part in the weak interaction was not settled until the 1950's, when decays of the particles discovered meanwhile, the muon, the pion and the Kaon, were investigated. Early data selected one alternative out of each pair S,V and A,T, and they were subsequently found to be the V and A parts.

So far the two surviving terms in (1.3) are Lorentz scalars, reflecting the widespread belief that parity was conserved in all interactions. This had to be readjusted after the discovery [8] of parity violation in weak interaction (1956), first suggested by Lee and Yang [9] , which necessitated pseudoscalar terms to be added to the Hamiltonian. The fact that neutrinos are proven to occur in one helicity state only, neutrinos being left-handed, whereas antineutrinos are right-handed (maximal) parity violation), then led to the following form of the Fermi interaction:

$$\mathcal{L}_{int} = \frac{G_F}{\sqrt{2}}[\bar{p}\gamma^\mu(g_V - g_A\gamma_5)n\ \bar{e}\gamma_\mu(1-\gamma_5)\nu] \tag{1.5}$$

Thus the leptonic current is of the V-A form, whereas the nucleon current is a mixture of V and A depending on the values of vector and axial coupling.

1.1.3 The V-A Theory and the Need for a Gauge Theory

In 1957, the main facts about the weak interaction established by experiment were the universality of the Fermi coupling, lepton number conservation, and a two component neutrino. They lead to the universal V-A interaction

$$\mathcal{L}_{int} = \frac{G_F}{\sqrt{2}} J^\mu(x) J^+_\mu(x) \tag{1.6}$$

formulated [10] as a point self-coupling of a current that includes a leptonic and a hadronic part

$$J^\mu = J^\mu_\ell + J^\mu_h \tag{1.7}$$

and gives rise to purely leptonic (e.g. $\mu^- \to e\nu_\mu\bar{\nu}_e$), semileptonic (e.g. $n \to pe^-\bar{\nu}_e$) and hadronic interactions (e.g. $\Lambda \to p\pi^-$). The lepton current J^μ_ℓ is of V-A form and automatically preserves lepton number, whereas the hadron J^μ_h is a mixture of V and A as in (1.5). In taking matrix elements of J^μ_ℓ between lepton states the current can be regarded as containing free field operators. The result $g_V \simeq 1$, i.e. that the coupling strength is the same, for instance, for muon and neutron decay, needed explanation, since it is not at all clear that strong interactions leave unaffected the weak charge of the nucleon that is not a bare free particle like the muon in muon decay. Thus it was proposed [11] that the vector part of J^μ_h is a component of a triplet of flavour isospin currents $I^\mu_j, j = 1,2,3$ that are conserved under the strong interaction, for which flavour isospin is known to be a good quantum number. Then

$$(J^\mu_h)_V \ = \ (I^\mu_1 + iI^\mu_2) \tag{1.8}$$

$$(J^{\mu}_{h})^{+}_{V} = (I^{\mu}_{1} - iI^{\mu}_{2}) \tag{1.9}$$

$$j^{\mu}_{EM} = I^{\mu}_{3} , \tag{1.10}$$

and the weak and electromagnetic charges of the hadrons remain unrenormalized by the strong interaction. This hypothesis was extended by Cabibbo to apply to strangeness-changing reactions by using flavour SU(3) of the quark classification model [13].

However, the dimensionful pointlike coupling G_F involved in all formulations so far is inherently problematic because it must lead to a violation of partial wave unitarity at high energies; since a pointlike interaction is pure s-wave, and since the upper bound on the intensity of each partial wave falls like $\frac{\pi}{2E^2}$, the high energy total cross-section which must behave like $G_F^2 E^2$ on dimensional grounds, violates the bound at $E^4 = \frac{\pi^2}{8G^2}$. This is not remedied by considering corrections of higher order in G_F, which, on the contrary, turn out to be divergent, signalling a potential non-renormalisability of the theory. Both troubles indicated the need for a theory without pointlike four-fermion couplings. If one introduces charged intermediate vector bosons $W^{\pm}$ as carriers of the weak force, analogous to the photon in electromagnetism, the high energy behaviour (for reactions like $\nu_e + e \rightarrow e + \nu_e$) becomes finite since the coupling is now replaced by $\frac{G}{\sqrt{2}} \rightarrow \frac{g^2}{q^2 - M_W^2}$. However there are immediately new problems associated with processes involving the longitudinal polarisation states of the $W^{\pm}$, allowed for massive gauge bosons, for instance $\nu_e \bar{\nu}_e \rightarrow W_L^+ W_L^-$. They indicated a motivation [2] for the inclusion of a third, neutral vector boson Z^0 as carrier of a neutral weak force. The Z^0 amplitude contributes to the same channel and cancels the divergence. We observe that we have thus introduced for the first time a self-coupling of force carriers, as in the channel above,

[2] This is not the only possible way out. an off-shell heavy lepton connecting the two $\nu - W$ vertices is a further alternative that has however not found experimental confirmation. Note that despite the improved high energy behaviour after the introduction of a Z^0 boson, there remains a violation of s-wave unitarity at energies of the order $10^9 M_W$.

for instance, at the vertex $Z^0 W_L^+ W_L^-$. This hints in the direction of a non-abelian theory in which such self-couplings arise naturally due to the non-commutativity of the symmetry transformations.

1.2 Gauge theory of the weak interaction

1.2.1 Geometrical motivations

It still remains a mystery that the geometrical analysis which led to such a deep understanding of gravitation has no success elsewhere in physics.
(F. Dyson, 1965 [16]).

The rise of gauge theory owes as much to its physical significance in predicting the gauge interactions of the weak force and in providing a consistent framework for the removal of quantum field theory infinities, as to the fact that a general mathematical model exists that bases the topological properties of gauge theory on a fruitful ground. It led to the realisation that gauge theory is a geometrical, i.e. coordinate-free theory. This guarantees the following symmetry properties that are required of any viable candidate theory which aims to be a nonlinear generalisation of Maxwell electromagnetism:

- 'external' symmetries under the Lorentz and Poincare groups.
- 'internal' symmetries under Lie groups like SU(2).
- covariance to allow a generalistion to curved spacetime and thus a coupling to gravitation.

In this section a geometrical approach is chosen to demonstrate in a convenient way the mechanism of a gauge theory. Non-abelian phase rotations were first investigated by Yang and Mills in 1956 [12] The essential idea of a gauge theory is the fusion of the (Minkowski) spacetime $M = \mathcal{M}^4$ in which a particle multiplet moves, and an 'isospace' G in which its internal variables (generalised phases) live, that specify the particle substate within the multiplet, into a 'total' space P. More accurately, the latter are specifying, for each $x \in M$, a particular transformation $\mathrm{g}(x)$ belonging to a continuous (Lie) symmetry group $G = SU(n)$, say, under which the theory is invariant. The associated conserved current and additive quantum numbers (Noether's theorem) correspond to Casimir invariants of the multiplet ('isospin(s)'). The number d of independent variables in isospace is equal to the number of generators of G, which belong to the Lie algebra $L(G)$ and can be represented by skew Hermitean $m \times m$ matrices $\mathbf{T}^a$, $a = 1, ..., d$. Their size m is determined by the dimensionality of the matter multiplet that spans the representation, denoted by $V_{\mathbf{T}^a}$. [3]

The *gauge principle* now states that any local transformation

$$\mathbf{g}(x) = \exp[-i\mathbf{T} \circ \Theta(x)] \tag{1.11}$$

in isospace must lead to an equivalent description of the same physical reality. [4] Thus there is no preferred choice of isopoints at each spacetime location that could be distinguishable physically. [5] The gauge principle is reflected in an *affine* transformation law for the gauge potential we are going to construct, meaning that there is no absolute local unity operator in the space of gauge transformations. This corresponds to an arbitrariness in a local rescaling of the potential in classical electromagnetism.

Now the question arises naturally of when we say that a particle multiplet moves in spacetime, along a curve from x to $y = x+\delta x$, without changing its direction in isospace, i.e. its isospin components. Due to the arbitrariness outlined above, the answer can only be given *relative* to a *chosen* gauge that is fixed by specifying a gauge potential $\underline{\mathbf{A}}(x)$ at each isopoint: it provides the connection between adjacent

[3]To specify completely a particle substate requires the knowledge of the eigenvalues of the r commuting generators in $L(G)$, where r is the rank of $L(G)$. For $G = SU(n)$, $d = n^2-1$, $r = n-1$. Incidentally, r is at the same time the number of independent invariants in the set of polynomials on $V_{\mathbf{T}^a}$.

[4]We denote summations over the Lie degrees of freedom $a = 1, ..., d$ by $\circ$, and by $\cdot$ scalar products in spacetime. Matrix representations induced by fermion multiplets are boldface. 1-Forms are underlined, and tangent vectors are overlined.

[5]This fact is represented mathematically in the construction of a principal fibre bundle, where the fibres G_x (isospace at x) are copies of G which have however 'lost the memory' which of their elements is the unit transformation. Once an isopoint $\mathbf{g}_0$ is chosen one can reach any isopoint $\mathbf{g}$ by an appropriate $h \in G$, since G is a group: there always is a $\mathbf{h}$ such that $\mathbf{h}\mathbf{g}_0 = \mathbf{g}$ (at fixed x).

isospaces G_x, G_y by fixing pairs of isopoints which are to be identified with each other. Thus once a gauge has been chosen, we know how to *parallel-transport* a particle multiplet in P; this is possible since one can prove that the *connnection form* in P

$$\underline{\omega} = \mathbf{g}^{-1}\, \underline{d}\mathbf{g} + \mathbf{g}^{-1}\underline{\mathbf{A}}\mathbf{g}\ , \quad \mathbf{g} = \mathbf{g}(x) \tag{1.12}$$

uniquely determines 'vertical' (pure gauge rotations) and 'horizontal' (parallel transport) directions in P. For this to hold everywhere in P, any pure gauge transformation (at any base point $x \in M$, $(x, \mathbf{g}) \to (x, \mathbf{g}') = (x, \mathbf{h}^{-1}\mathbf{g})$ must leave $\underline{\omega}$ invariant, from which one immediately deduces the transformation law for the gauge potential:

$$\underline{\mathbf{A}}' = \mathbf{h}^{-1}\, \underline{d}\mathbf{h} + \mathbf{h}^{-1}\underline{\mathbf{A}}\mathbf{h}. \tag{1.13}$$

This shows the expected affine structure, $\underline{\mathbf{A}}$ is not a tensor under G. Since points $p \in P$ in total space can be written locally as $p = (x, \mathbf{g}(x))$, we have in local coordinates

$$\underline{\mathbf{A}} = \mathbf{T} \circ A(x) \cdot \underline{d}x = \mathbf{A}_\mu(x)\underline{d}x^\mu = \mathbf{T}^a A^a_\mu(x)\underline{d}x^\mu, \tag{1.14}$$

where the generators satisfy $[\mathbf{T}^a, \mathbf{T}^b] = if^{abc}\mathbf{T}^c$ with f^{abc} the structure constants of the gauge group. $\underline{\mathbf{A}}$ is at the same time a field of 1-forms in spacetime and an operator in the internal space and has $4d$ degrees of freedom at each $p \in P$. The direction tangent to P associated with parallel transport is given by the *covariant derivative*

$$\overline{\mathbf{D}} = \mathbf{I}\overline{\frac{\partial}{\partial x}} + A(x)\mathbf{T} \circ \left(\mathbf{g}\overline{\frac{\partial}{\partial \mathbf{g}}}\right) = \mathbf{I}\overline{\frac{\partial}{\partial x}} - iA(x)\mathbf{T} \circ \overline{\frac{\partial}{\partial \Theta}} \tag{1.15}$$

where the matrices $\mathbf{T}$ are normalised to $2\ tr(\mathbf{T}^2) = 1$. The covariant derivative is determined precisely by the requirement that it be annihilated by the connection form $\underline{\omega}$. This establishes the constraint on the dynamics in the total space, for in order to keep the phase (i.e. direction in isospace) of the multiplet parallel with respect to the given connection, the way it moves through spacetime has to be correlated with the change in the gauge potential along the path, as dictated by $< \underline{\omega}|\overline{\mathbf{D}} >= \mathbf{0}$. The parallel transport ensures that the fields describing the multiplet along the path in M remain a solution of the equations of motion, where the 'normal' derivative is replaced by the covariant derivative (1.15), thus incorporating the minimal coupling prescription that is now based on a geometrical principle.

To a fictitious observer in the internal 'inertial' space, a movement of the multiplet in spacetime would reveal itself as a rotation of the isopoint in the presence of the potential $\underline{\mathbf{A}}$. Since this correlation is prescribed locally only, a finite movement of the multiplet along a closed path in spacetime need not reproduce the original orientation in isospace. The amount of mismatch caused by the distortion of the total space P due to $\underline{\mathbf{A}}$ is described by the *gauge field* or curvature:

$$\underline{\underline{\mathbf{F}}} = \underline{d}\,\underline{\mathbf{A}} + \underline{\mathbf{A}} \wedge \underline{\mathbf{A}} \quad \text{,or} \tag{1.16}$$

$$\mathbf{F}_{\mu\nu} = \partial_{[\mu}\mathbf{A}_{\nu]} + [\mathbf{A}_\mu, \mathbf{A}_\nu] \tag{1.17}$$

where all forms are evaluated at the same point $x \in M$. Unlike the gauge potential, the gauge field does transform as a tensor under G: $\underline{\underline{\mathbf{F}}}' = \mathbf{h}^{-1}\underline{\underline{\mathbf{F}}}\mathbf{h}$, and depends on two directions in M. [6]

Finally, we have found the distortion of the total space linked to a field which is a geometrical object, similar to the way distortions in the geometry of spacetime are linked to the gravitational field. Equation (1.16) shows that the gauge field depends non-linearly on its potential, and that for a non-abelian case it will in general be impossible to satisfy an integrability condition $\underline{\underline{\mathbf{F}}} = \underline{d}\,\underline{\mathbf{H}}$ for some $\underline{\mathbf{H}}$, not even locally. This is the mathematical origin of non-abelian phases a system can acquire when moving around a closed path in total space.

[6] As required, the action $S = -\int_M tr(\underline{\underline{\mathbf{F}}} \wedge^{*} \underline{\underline{\mathbf{F}}})$ is invariant under the gauge group G, where $^{*}\mathbf{F}$ is the dual of $\mathbf{F}$.

1.2.2 The electroweak theory

I would prefer a model with as few arbitrary coupling constants as possible. There is a free parameter θ_W in the Weinberg model and, more seriously, there is nothing which makes you quantise charge - the average charge of each multiplet is fixed by hand; I would be rather disappointed if that model turned out to be correct.
(Theoretician at the Bonn Electron Photon Symposium, Aug. 1973)

The electroweak gauge theory is based on the direct product

$$G_{EW} = SU(2)_{t_L} \otimes U(1)_y \tag{1.18}$$

of two simple groups, introduced by Glashow [14]. [7] It is a *'chiral'* theory since transformations of $SU(2)_{t_L}$ affect left-handed fields only, and hence it regards different helicity states of the same fermion as separate physical entities. On the other hand, different physical particles are assigned to multiplets of definite $SU(2)_{t_L} \otimes U(1)_y$ quantum numbers. More specifically, experimental input led to a classification as follows: $\nu_{e,L}, e_L, u_L, d_L$ enter two doublets (ν_L, e_L) and (u_L, d_L), whereas all right-handed degrees of freedom e_R, u_R, d_R enter weak isospin singlets, and similarly for the second and third generation families ν_μ, μ, c, s and ν_τ, τ, t, b.

The product structure of G_{EW} is reflected in the presence of two independent couplings g and g' for $SU(2)_{t_L}$ and $U(1)_y$, respectively. This is sometimes taken as an argument against the theory having achieved a true unification. However, the fact that weak and electromagnetic processes occur at comparable strength at sufficiently high energy vindicates its interpretation as a unifying description. The quantitative condition to be met is the requirement that the ratio

$$\frac{g'^2}{g'^2 + g^2} = \sin^2\theta_W \equiv s^2 \equiv 1 - c^2 \tag{1.19}$$

be significantly different from both 0 and 1, which is fulfilled by the experimental value of $\sin^2\theta_W \sim 0.23$. Since the $SU(2)$ of G_{EW} is a rank one group and U(1)

[7] We shall denote by $t(t+1)$ the eigenvalue of the operator $\hat{t}_L \circ \hat{t}_L$.

is abelian, we have two quantum numbers - namely the weak-isospin t and weak-hypercharge y - to specify completely a fermion multiplet F of definite helicity σ, $(t, y)_{F,\sigma}$. The dimensions of the two factor groups are 3 and 1, respectively, which gives three weak-isospin gauge potentials $\mathbf{W}^{1,2,3}$ and one weak-hypercharge gauge potential B: the minimum freedom necessary to accommodate the electromagnetic and the three $W^{\pm}$ and Z^0 force fields, which were motivated in section 1.1.3.

The interaction Lagrangian is composed of four terms:

$$\mathcal{L} = \mathcal{L}^F + \mathcal{L}^B + \mathcal{L}^S + \mathcal{L}^{FS} \tag{1.20}$$

where F, B, S denote the fermion, vector boson and scalar degrees of freedom. Their interactions are contained in the $SU(2) \otimes U(1)$ covariant derivative

$$\mathbf{D}_\mu = \mathbf{I}\partial_\mu - ig\frac{\boldsymbol{\tau}}{2} \circ W_\mu - ig'\mathbf{I}\frac{y}{2}B_\mu \tag{1.21}$$

which acts on any fermion (F) or scalar (Φ) multiplet of given t, y. The number of components in the multiplet determines the dimension of the representation $\mathbf{T}$ of the generators of $SU(2)_{t_L}$. For our case one may choose $\mathbf{T}^a = \boldsymbol{\tau}^a/2$ with the Pauli matrices $\boldsymbol{\tau}^a$. Summing over all contributing multiplets F of definite helicity, we have

$$\mathcal{L}^F = \sum_F \bar{F}(x) i D_\mu \gamma^\mu F(x) \ \ , \ x \in \mathcal{M}^4 \tag{1.22}$$

which comprises the kinetic terms for the fermions and their coupling to the gauge bosons. For singlets ($\sigma = R$) we might define $t_{(R)} = 0$. The kinetic term for the gauge bosons is contained in

$$\mathcal{L}^B = -\frac{1}{4} tr(\mathbf{G}_{\mu\nu} \circ \mathbf{G}^{\mu\nu}) - \frac{1}{4} B_{\mu\nu} B^{\mu\nu} \tag{1.23}$$

with the gauge field strengths $B_{\mu\nu} = \partial_{[\mu} B_{\nu]}$ and $G^a_{\mu\nu} = \partial_{[\mu} W^a_{\nu]} - ig[W^b_\mu, W^c_\nu]$ and it includes tri- and quadrilinear self-couplings of the gauge bosons $W^{1,2,3}$. The scalar sector

$$\mathcal{L}^S = (D^\mu \Phi)^+ (D_\mu \Phi) - \mu^2 \Phi^+ \Phi - \lambda (\Phi^+ \Phi)^2, \quad \mu^2 < 0 \tag{1.24}$$

introduces a two-component complex field $\Phi \in \mathcal{C}^2$ and is responsible for the gauge symmetry to be hidden. The vacuum expectation value $< 0|\Phi^+\Phi|0 >^2 = -\mu^2/2\lambda \equiv v^2/2$ that minimizes the classical energy density of the scalar field is not gauge invariant, but gauge transformations do not change the energy of the vacuum. The spontaneous symmetry breaking [17] supplies four degrees of freedom for the longitudinal polarisation states of the W_μ^a and B_μ which are thereby allowed to acquire a mass proportional to vg^2 and $y_\Phi^2 vg'^2$, respectively. Choosing the *unitary gauge* which is defined by fixing the vacuum field to be of the form $\Phi = (0, v/\sqrt{2})^T$ and assigning $y_\Phi = -1$ ensures that the vacuum is electromagnetically neutral and that the photon remains massless. Three scalar degrees of freedom give longitudinal polarisation states and mass terms to the physical $W^\pm$ and Z^0 fields, $M_W = vg/2, \;\; M_Z = M_W/\cos\theta_W$, whereas the remaining fourth degree of freedom gives rise to the so-called Higgs field, a scalar boson of mass $\sqrt{-2\mu^2}$. In perturbation theory, the only way to increase the number of degrees of freedom is the introduction of further fields to the Lagrangian, however it might turn out that the gauge symmetry is hidden non-perturbatively through dynamical effects involving existing degrees of freedom, like a condensate of bound heavy fermion-antifermion pairs.

Finally, $\mathcal{L}^{FS}$ is responsible for the description of the fermion masses through linear Yukawa interactions of the G_{EW}-multiplets with the fields Φ and $\tau_2\Phi^*$, that give mass to the $t^3 = -1/2$ ('d') and $t^3 = -1/2$ ('u') fermions, respectively. However, the states F, f that diagonalise these Yukawa interactions of the form $(\bar{F}'^L\Phi)f_d'^R$ and $(\bar{F}'^L\sigma_2\Phi^*)f_u'^R$ are not the electroweak eigenstates, but emerge from them through a unitary transformation, parametrised in terms of a mixing matrix [18]. By convention, one can choose only the 'd' type quarks to be mixed in that way, and that is why table 1.1 (next section) shows the Yukawa mass eigenstates for the 'u' type quarks. No mixing in the lepton sector seems to be justifiable to date.

1.3 Neutral Currents in the Standard Model

There is now, for the first time, positive evidence of neutral currents in neutrino reactions. Viewed in the context of the Weinberg-Salam theory the leptonic and semi-leptonic results are not incompatible. (G. Myatt, Bonn 1973)

We now focus on neutral current interactions within the electroweak theory as they are in the center of interest of the work presented thereafter. The proven absence of strangeness-changing neutral currents and the intrinsic difficulty to isolate an unambiguous NC signal delayed the recognition of their existence until well after the first NC events were probably recorded in the first neutrino beam experiments. Higher energies and a thourough understanding of the neutron background, $(n) + N \to X$ faking $(\nu) + N \to (\nu) + X$ (unseen particles in brackets), led to the discovery at CERN of neutral currents in 1973 [25] both in the exclusive $\overline{\nu}_\mu + e^-$ *to* $\overline{\nu}_\mu + e^-$ and in the inclusive $(\nu) + N \to (\nu) + X$ channel, using a freon (CF_3Br) heavy liquid bubble chamber. In the standard model, the weak neutral current interactions occur through the coupling in $\mathcal{L}^F$ of currents J^0_μ and J^y_μ to the neutral gauge potentials via

$$
\begin{aligned}
\mathcal{L}^{NC}_\mu &= (gcJ^3_\mu - g's J^y_\mu)\, Z^\mu && (1.25)\\
&= \frac{g}{c}(c^2 J^3_\mu - s^2 J^y_\mu)\, Z^\mu, && (1.26)\\
\text{where } J^0_\mu &= \sum_F \bar{F}\gamma^L_\mu \frac{\tau^3}{2} F && (1.27)\\
&= \sum_{f,\sigma} \bar{f}\gamma^L_\mu t^3_f f \delta_{\sigma,L} && (1.28)\\
\text{and } J^y_\mu &= \sum_{f,\sigma} \bar{f}\left(\gamma^L_\mu \frac{y^L_f}{2}\delta_{\sigma,L} + \gamma^R_\mu \frac{y^R_f}{2}\delta_{\sigma,R}\right) f. && (1.29)
\end{aligned}
$$

Note the appearance of t^3_f when recasting the sum over F into a sum over the individual fermions f and helicities σ. [8] The orthogonal complement $(gsJ^3_\mu + g'cJ^y_\mu)$ couples to the electromagnetic gauge potential A_μ and yields the unification

[8] It is noteworthy at this point that the normalisation of the non-abelian generators is constrained by the non-linear commutation relations, whereas in the abelian case the gauge potentials can couple with any strength.

condition

$$|e| = g \sin\theta_W \tag{1.30}$$

We can write (1.25) as a sum over the physical fermion degrees of freedom:

$$J_\mu^{NC} = \frac{g}{c}\sum_f \bar{f}\left(t_f^3\gamma_\mu^L - s^2 Q(\gamma_\mu^L + \gamma_\mu^R)\right) f \;\; Z^\mu \tag{1.31}$$

using $Q = t^3 + \frac{y}{2}$. [9] Here it is seen that the (weak) isovector component of the neutral current is of pure V-A structure, whereas the isoscalar component is a pure Lorentz vector, and the relative couplings ensure that neutrino currents remain pure V-A. Decomposing J_μ^{NC} into terms of definite spacetime structure one obtains with $\gamma_\mu^{L,R} = \gamma_\mu P^{L,R}$, $P^{L,R} = \frac{1\mp\gamma_5}{2}$ and $2\gamma_\mu^{L,R} = \gamma_\mu \mp \gamma_\mu\gamma_5 = \gamma^V \mp \gamma^A$:

$$J_\mu^{NC} = \frac{g}{2c}\sum_f \;\bar{f}\left(\gamma^V v_f - \gamma^A a_f\right) \tag{1.32}$$

$$v_f = [t_f^3(1-s^2) - \frac{s^2}{2}(y_f^L + y_f^R)] \tag{1.33}$$

$$a_f = [t_f^3(1-s^2) - \frac{s^2}{2}(y_f^L - y_f^R)] \tag{1.34}$$

This has to be distinguished carefully from a decomposition using (strong interaction) flavour quantum numbers I, Y in situations involving u,d quarks only: often used is then the identification $t^3 = I^3$, and with the prescription $Q = I^3 + Y/2$, where the strong hypercharge Y is defined in terms of baryon number B and strangeness S as $Y = B + S$, one obtains ($S = 0$)

$$J_\mu^{NC} = \frac{g}{2c}\sum_f \bar{f}\left(\gamma^V[I^3(1-2s^2) - s^2 Y] - \gamma^A I^3\right) f\,. \tag{1.35}$$

The constants arising from eqn.(1.31) are called *chiral couplings* and have the values:

$$c_f^L = t_f^3 - s^2 Q_f \;\text{ and }\; c_f^R = -s^2 Q, \tag{1.36}$$

They have opposite signs for $f, \bar{f}$, since $Q_f = -Q_{\bar{f}}$ and $(\bar{d}, -\bar{u})$ transforms in an identical manner under SU(2) as (u, d), i.e. $t_{\bar{d}}^3 = +1/2$. The values of $c_f^{L,R}$ are

[9] In our convention the lepton hypercharges are integers, the quark hypercharges are multiples of 1/3, and $SU(2)_{t_L} \otimes U(1)_y$ gauge transformations on isodoublets are given by $\exp\left(-i\frac{\tau}{2} \circ \Theta(x) - i\frac{y}{2}\mathbf{I}\theta(x)\right)$ with the $SU(2)$ generators satixfying $\tau_i^2 = 1$. We prefer to maintain separate expressions $y_f^L/2 = Q_f - t_f^3$, $y_f^R/2 = Q_f$ to emphasise the chiral asymmetry of the theory.

1.	2.	3.	t_f^3	y_f	Q_f	c_f
$\begin{pmatrix} \nu_e \\ e \end{pmatrix}_L$	$\begin{pmatrix} \nu_\mu \\ \mu \end{pmatrix}_L$	$\begin{pmatrix} \nu_\tau \\ \tau \end{pmatrix}_L$	$+1/2$ $-1/2$	-1	0 -1	$1/2$ $-1/2 + s^2$
e_R	μ_R	τ_R	0	-2	-1	s^2
$\begin{pmatrix} u \\ d' \end{pmatrix}_L$	$\begin{pmatrix} c \\ s' \end{pmatrix}_L$	$\begin{pmatrix} t \\ b' \end{pmatrix}_L$	$+1/2$ $-1/2$	$+1/3$	$+2/3$ $-1/3$	$1/2 - 2/3s^2$ $-1/2 + 1/3s^2$
u_R	c_R	t_R	0	$+4/3$	$+2/3$	$-2s^2/3$
d'_R	s'_R	b'_R	0	$-2/3$	$-1/3$	$s^2/3$

Table 1.1: *G_{EW}-quantum numbers for the elementary fermions of the (first) three families. The weak isospin of each multiplet is $t = |t^3|$.*

listed in table 1.1, together with the electroweak quantum numbers of the fermions. Similarly, eqn. (1.32) gives the *vector and axial couplings*

$$v_f = t_f^3 - 2s^2 Q \quad \text{and} \quad a_f = t_f^3 \tag{1.37}$$

The mixing of the fields W^3, B into Z^0, A indicate the nontrivial way in which the minimal gauge group achieves the fusion of two forces into one gauge force. It is responsible for the cross-sections of neutrinos and antineutrinos on protons to be different from each other. The possibility of intense antiproton beams, that ensued from the discovery of van der Meer of stochastic cooling [19], enabled CERN to build a proton- antiproton synchrotron collider with sufficient energy and luminosity to produce the first (real) $W^\pm$ and Z^0 bosons in 1983 [20]. The Z^0 is now mass--produced after the electron positron colliders, at SLAC, and LEP at CERN, started operation in 1989. Figure 1.1 shows a decay of a Z^0 into hadrons, collected with the DELPHI detector at CERN during the LEP 'pilot' run in August 1989. Displayed are the Inner Detector, the Time Projection Chamber (hits as crosses), the Outer Detector and the High-Pressure electromagnetic Calorimeter (energy depositons as small boxes). The full lines are fitted tracks.

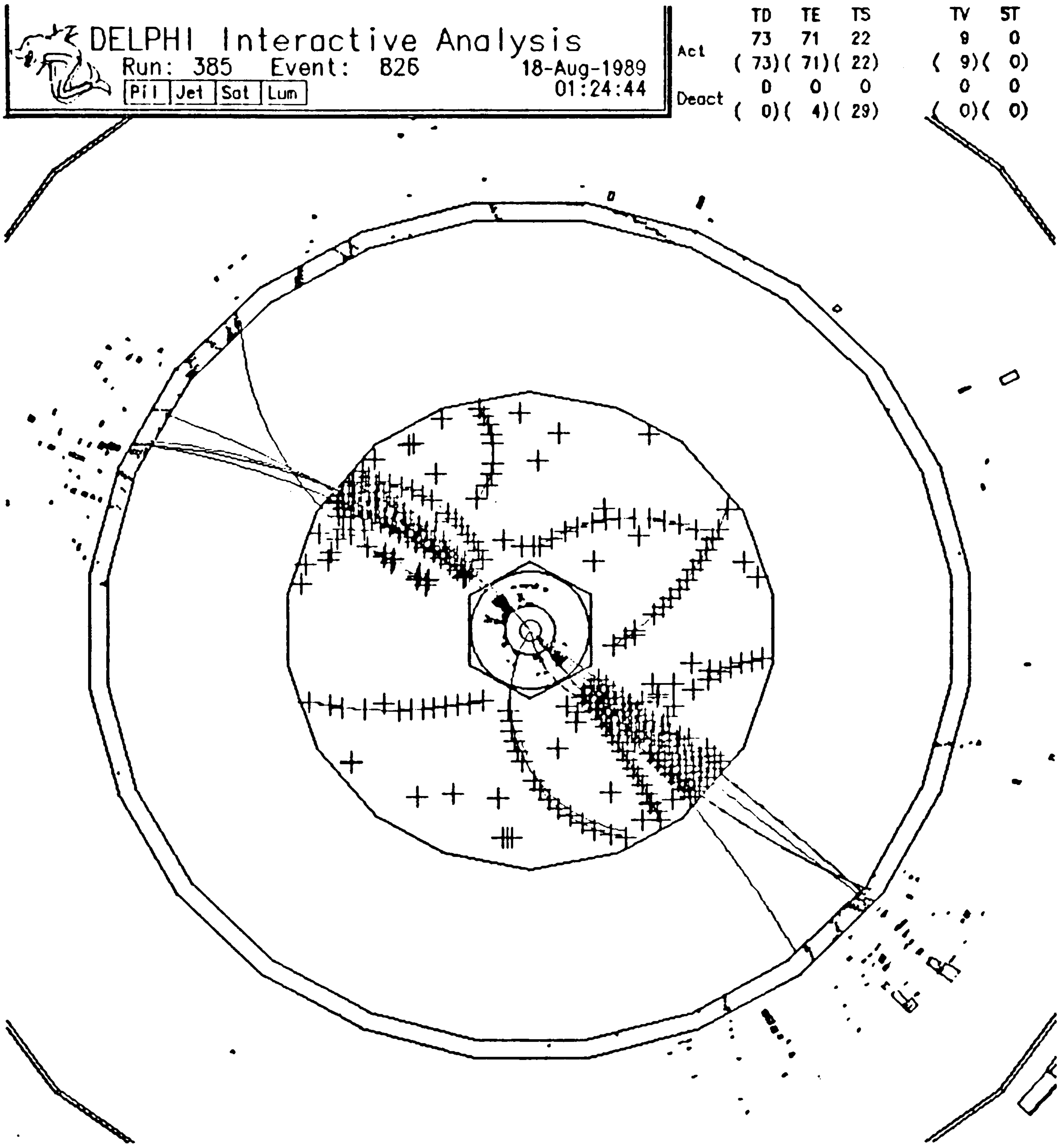

Figure 1.1: Hadronic decay of a Z^0 produced by electron positron collision in LEP detected with DELPHI.

1.4 Deep Inelastic Scattering

The investigation of neutral current processes provides insights into the electroweak mixing and thus stringent tests of the standard model parameters, as well as being a novel probe to the structure of hadrons. Since the Z^0 boson interacts with a hadron in a leptoproduction reaction like $\ell N \to \ell' X$ via a pointlike vertex, we have a possibility at hand to resolve local properties of a bound state system, e.g. of the nucleon. For this purpose neutrino deep inelastic scattering (DIS) is a unique arena as neutrinos only interact via the weak force. We consider the DIS process induced by (anti)neutrinos:

$$\nu(k_\mu) + N(P_\mu) \overset{Z^0(q_\mu)}{\longrightarrow} \nu(k'_\mu) + H(p_\mu) \tag{1.38}$$

where N, H are the proton (Nucleon), and hadronic system, respectively, and the four-momenta assigned are given in brackets.

Because the binding energies in a hadron are comparable to the rest energies of its constituents, it is however impossible to assume an interaction with quasi-free constituents (or even with a fixed number of constituents). DIS makes use of the fact that this is a frame dependent statement, and that the constituents (*'partons'*) can actually be regarded as quasi-free in a frame in which the nucleon is fast. Such a frame can be considered applicable to a physical situation if the energy transfer $E_{\ell'} - E_\ell = \nu^{lab} = (q \cdot P)^{lab}/M_P$ to the nucleon is large, as then the nucleon is fast in the relevant current-nucleon center of momentum frame. It is assumed that DIS can be described by an impulse approximation in which two requirements are fulfilled:

- Bound-state effects on the virtual constituents, which have a lifetime τ_V, decouple from the interaction timescale, $\tau_{IA} \ll \tau_V$.
- After the impact the scattered parton has an energy far greater than the typical

binding energies $\Delta E \sim \frac{1}{r_{Had}}$, where r_{Had} is a hadron effective size, and can be considered quasi-independent of the hadron.

One can show that for $Q^2 \equiv -q^2 \gg (xM)^2$, i.e. $Mx \ll \nu$ (here $P = |P^z|$):

$$\tau_{IA} \sim \frac{P}{2M\nu} = \frac{xP}{Q^2} \quad \text{and} \quad \tau_V \sim \frac{xP}{\mu_T^2} \tag{1.39}$$

where $\mu_T^2 \equiv \; < m^2 + k_T^2 > \; \ll xP$ is an effective transverse mass of the partons contributing, for primordial parton transverse momentum k_T. Both time scales grow with P, but their ratio $\tau_{IA}/\tau_V \sim \mu_T^2/Q^2$ is small provided Q^2 is large enough, and $x \neq 0$. Thus in the kinematical domain $Q^2 \gg \mu_T^2, \nu \gg \Delta E$, and $\nu \gg Mx \gg M^2/\nu$ the current makes an instananeous local measurement of the hadron wavefunction.

The general Lorentz structure of the neutrino deep inelastic cross-section on an unpolarized target can be parametrized [23] with six scalar functions $W_i(\nu, Q^2)$, i = 1,6 , multiplying tensioral combinations of the four-momenta and the metric. Under the conditions specified above one can assume an interaction that is an incoherent superposition of elastic scattering off the partons. Requiring the parton with mass m to be real before and after the interaction, $p^2 = m^2 \cong 0$, one has approximately $0 \cong m^2 = -Q^2 + 2xM\nu$ which introduces a $\delta(Q^2 - 2xM\nu)$ and leads to scaling of the W_i in that they depend on the dimensionless ratio $x = \frac{Q^2}{2M\nu}$ only. The scaling is approximate since Fermi motion within the target as well as the dynamic QCD corrections introduce Q^2 scale dependent modifications. Scaling has been first observed in electron proton scattering at SLAC in 1969 [24] and subsequently in neutrinoproduction [28] at CERN. Time reversal invariance for neutrino reactions forces W_6 to vanish; $W_{4,5}$ can be argued [22] to be negligible for small quark masses. Thus the cross-section turns out to be given in terms of three scalar functions only, that can be related to the absorption of longitudinal and transverse virtual Z^0 bosons by the nucleon

$$\begin{aligned}\frac{d\sigma^{\nu,\overline{\nu}}}{dxdydQ^2} &= \frac{G^2 s}{2\pi}\left(\frac{M_Z^2}{-Q^2-M_Z^2}\right)^2 \cdot \\ &\left[\ \frac{y^2}{2}\, 2x\mathcal{F}_1^{\nu,\overline{\nu}}(x,Q^2) + \left(1-y-\frac{xyM^2}{s}\right)\mathcal{F}_2^{\nu,\overline{\nu}}(x,Q^2)\right. \\ &\left. \pm\left(y-\frac{y^2}{2}\right)x\mathcal{F}_3^{\nu,\overline{\nu}}(x,Q^2)\ \right]\end{aligned} \tag{1.40}$$

Here the Lorentz invariant quantities are defined as $Q^2 = -q^2, \nu = (q \cdot P)/M_P, y = (q \cdot P)/(k \cdot P), x = -q^2/(2q \cdot P)$. The $(Q^2 = xys)$-dependence (there are three independent kinematical quantities) from the Z^0 propagator term is negligible for the small values of $Q^2 \sim \mathcal{O}(10^{-3}M_Z^2)$ in our experiment. The *structure functions* $\mathcal{F}_{1,2,3}$ are the expressions $M_N W_1, \nu W_2, \nu W_3$ in terms of x, Q^2, respectively. In the parton model [21], they are independent of Q^2 and take the form

$$2\mathcal{F}_1 = \sum_f (v_f^2 + a_f^2)\, f(x) \tag{1.41}$$

$$\mathcal{F}_3 = \sum_f (2v_f a_f)\, f(x) \tag{1.42}$$

where we surpressed NC labels and indices for the beam helicity on the $\mathcal{F}$ and on the axial and vector couplings. However, we shall demonstrate in chapter 4 why the structure functions actually do not depend on the beam helicity for the NC case (unlike for CC reactions). $f(x)\,dx$ is interpreted as the probability to find a parton of type f with a longitudinal momentum fraction in the interval $[x, x+dx]$ in the nucleon. If there were only spin 1/2 partons in the nucleon, we would have the exact proportionality given by the Callan-Gross relation [26] $\mathcal{F}_2 = 2x\mathcal{F}_1$. Since partons include the vector bosons of the strong force (gluons), this relation is modified, as described in chapter 4.

We show the predicted dependence of the cross-section on the scaling variables $x_{(Bj)}$ and $y_{(Bj)}$ in figures 1.2 and 1.3, where we used the parton distribution functions of Glück, Hoffmann and Reya [27], evaluated for the two cases $Q^2 = 5GeV^2$

and $Q^2 = 50GeV^2$. A small scaling violation is seen as a shift towards lower $x_{(Bj)}$, as expected.

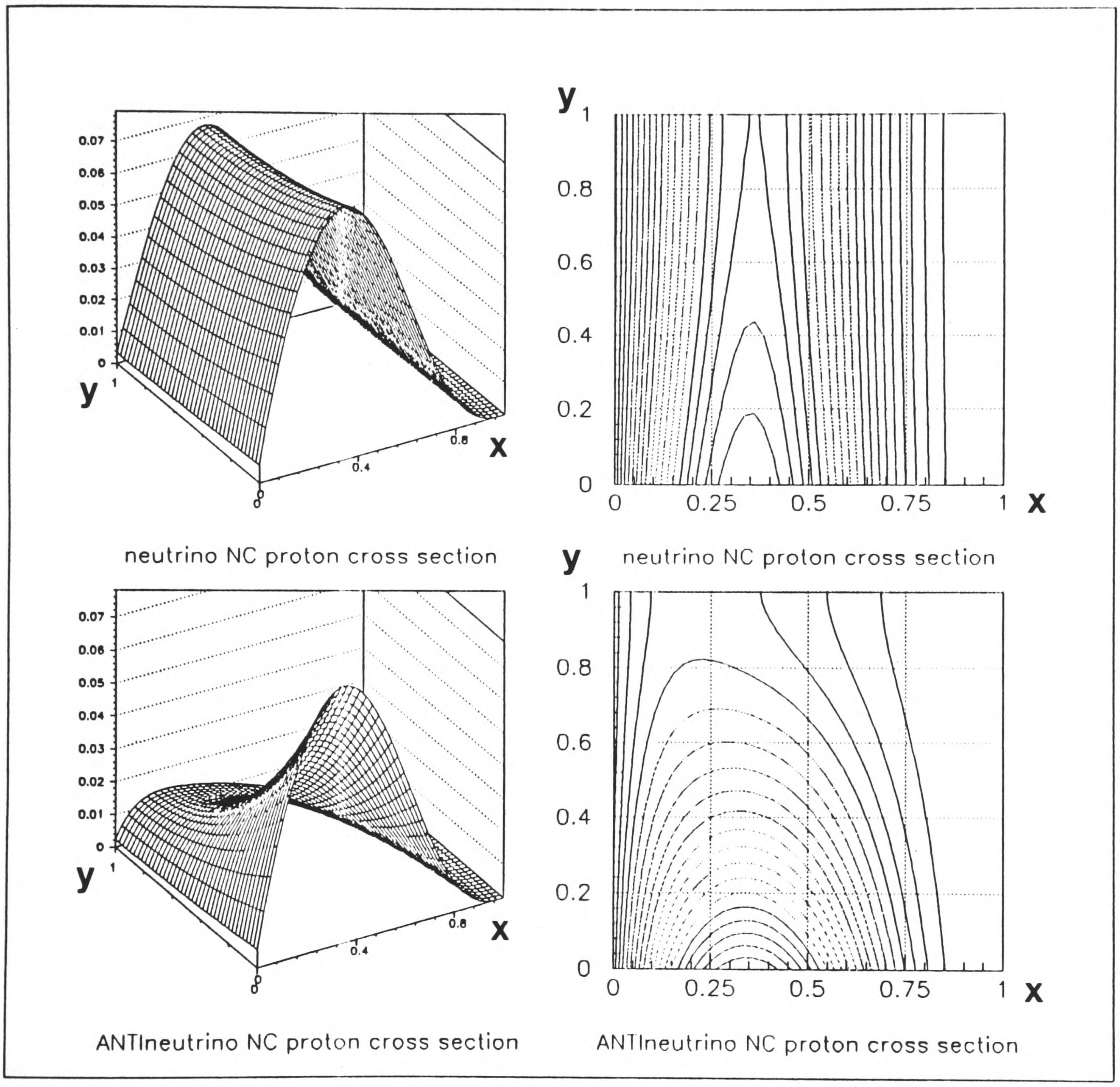

Figure 1.2: *Dependence of the cross-section on $x_{(Bj)}$ and $y_{(Bj)}$ for neutral current (anti)neutrino proton scattering at $Q^2 = 5GeV^2$, top (bottom) line. The units are arbitrary. On the right side we show contour lines of constant cross-section.*

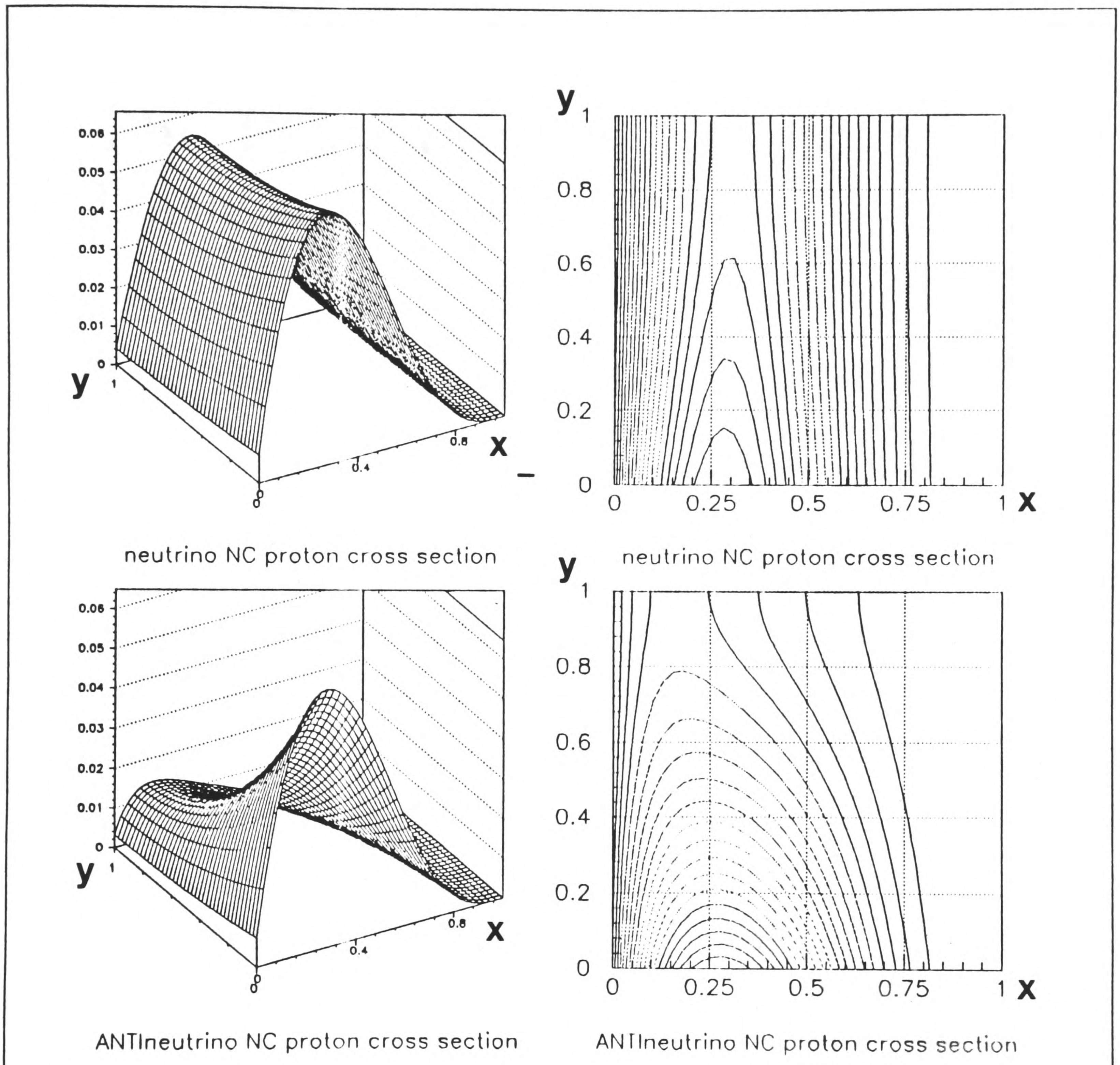

Figure 1.3: *Dependence of the cross-section on $x_{(Bj)}$ and $y_{(Bj)}$ for neutral current (anti)neutrino proton scattering at $Q^2 = 50GeV^2$, top (bottom) line. The units are arbitrary. On the right side we show contour lines of constant cross-section.*

Chapter 2

The Experimental Setup and Data Acquisition

2.1 The Neutrino Beam and the Detector

2.1.1 The SPS accelerator and Neutrino Beamline

Neutrino beams are necessarily secondary or tertiary beams, produced either through the interactions in a ('beam dump') target of fast charged particles that have been accelerated themselves, or through the weak decay of secondaries which have emerged in turn from interactions of accelerated charged primaries, usually protons. The second alternative is realised in this experiment: every 12 seconds a pulse ('beam spill') of 400 GeV protons ($M_P = 0.938$ GeV) is delivered from the Super Proton Synchroton (SPS) at the CERN accelerator center. The arrangement of the beam line components is shown in figure 2.1. This pulse of a duration of about 3ms contains some 10^{13} protons and is directed towards a beryllium target, where the protons undergo nuclear interactions producing a range of secondary particles, mostly pions (90%) and Kaons (9%).

The major part of this mainly hadronic shower is focused and charge-selected, leading to a beam that contains a broad momentum spectrum of secondaries. The focusing is achieved by a magnetic 'horn' which produces an azimuthal magnetic field cylindrically symmetric along the beam axis, that focuses off-axis particles of the selected charge towards the axis, and defocuses the other charge. The required pulsed current, synchronised with the beam spill, is 120kA. Since on the beam axis the magnetic field is vanishing, a stopper is installed at the end of the horn to absorb all those particles that could not be defocused due to their 'perfect' alignment. This reduces the contamination of the ensuing neutrino beam by antineutrinos and vice versa. A second focusing element, the so-called reflector, is positioned 92m downstream the target, it carried a current of 150 kA.

Then the secondaries enter a 290m long vacuum decay tunnel, where they undergo weak decays producing leptons and neutrinos. Due to their broad momentum spectrum the ensuing 'wide-band' beam contains itself a broad range of (anti)neutrino momenta at every radial distance. Positive (negative) secondaries give (anti)neutrinos. For the neutrino case, the most important decay modes are:

$$\pi^+ \rightarrow \mu^+\nu_\mu \quad 100\% \tag{2.1}$$

$$K^+ \rightarrow \mu^+\nu_\mu \quad 63.5\% \tag{2.2}$$

$$\rightarrow \pi^+\pi^0 \quad 21.2\% \tag{2.3}$$

$$\rightarrow \mu^+\nu_\mu$$

$$\rightarrow \pi^0 e^+\nu_\mu \quad 4.8\% \tag{2.4}$$

$$\rightarrow \pi^0\mu^+\nu_\mu \quad 3.2\% \tag{2.5}$$

$$\mu^+ \rightarrow e^+\nu_e\nu_\mu \quad 100\% \tag{2.6}$$

and the charge conjugates of these reactions are relevant for antineutrino production. Due to their large momenta, despite its length only 5% of the pions ($c\tau = 7.8m$) and 20% of the Kaons ($c\tau = 3.7m$) have decayed at the end of the tunnel (time dilatation with respect to the lab frame, or Lorentz contraction of the tunnel in their rest frame). Together with the undecayed secondaries, they enter a 185m long iron shield where all remaining hadrons are stopped within the first meters (the nuclear absorption length in iron is 17cm for neutrons). The shield is dimensioned in order to absorb the undecayed muons ($c\tau = 660m$) that interact with matter only electromagnetically (the ratio of muon energy loss through Bremsstrahlung relative to electrons goes like $(m_e/m_\mu)^2$). It contains six gaps for the muon flux monitoring system [38] that employs solid state detectors to measure the charge deposited by electron hole pairs produced from the high intensity of traversing muons (about $10^8 \mu/cm^2$ per pulse). To further reduce the muon contamination of the beam, 175m of earth shield follow the iron. In all, the detector is located some 820m downstream of the target, which means that the effective beam divergence is about 1mrad. Thus the direction of the neutrino beam is known to high accuracy from the position of the event vertex in the detector.

After the beam energy has been raised to 400 GeV, some muons deviating from the axis have been found leaving the iron shield and being rescattered towards the detectors. To suppress this unwanted effect, a 10m long toroidal magnet is installed at the end of the shield that ensures that those muons traverse as much material as possible, or are deflected away.

In 'narrow band' neutrino beams, where only a small momentum window of charged secondaries is focused (using quadrupoles rather than the horns), the tiny cross section for neutrino nucleon scattering, of the order of $10^{-38} cm^2/GeV$ per proton, necessitates a heavy target to produce reasonable numbers of events . For a hydrogen target this aim can only be achieved if a large momentum range of secondaries remains focused, in a high intensity beam wide band beam. Thus one gains an intense beam over a wide energy range but looses the valuable energy radius correlation and the facilitated determination of the neutrino flux that exists for a narrow band beam.

Figure 2.1: *The CERN SPS and the neutrino beam line. The beryllium target is located at 'T9', and BEBC at the end of the 'West Hall' (3).*

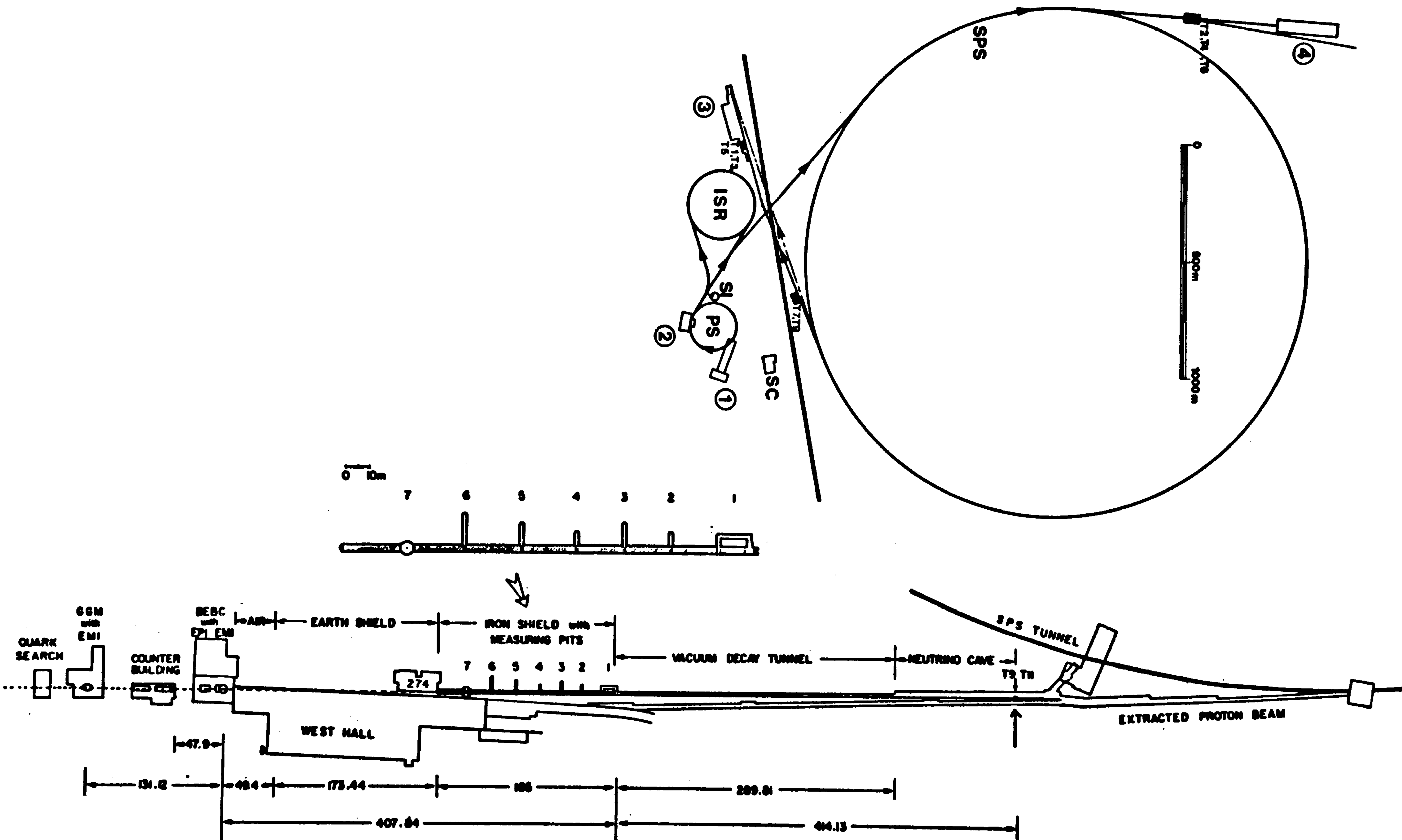
SPS
0
800m
1000m
ISR
PS
SI
SC
T1,T3
T5
T7,T9
T2,T4,T6
1
2
3
4
0 10m
7
6
5
4
3
2
1
QUARK SEARCH
GGM with EMI
COUNTER BUILDING
BEBC with EPI EMI
AIR
EARTH SHIELD
IRON SHIELD with MEASURING PITS
VACUUM DECAY TUNNEL
NEUTRINO CAVE
T9 T11
SPS TUNNEL
EXTRACTED PROTON BEAM
274
WEST HALL
47.9
131.12
49.4
173.44
185
289.81
407.64
444.13

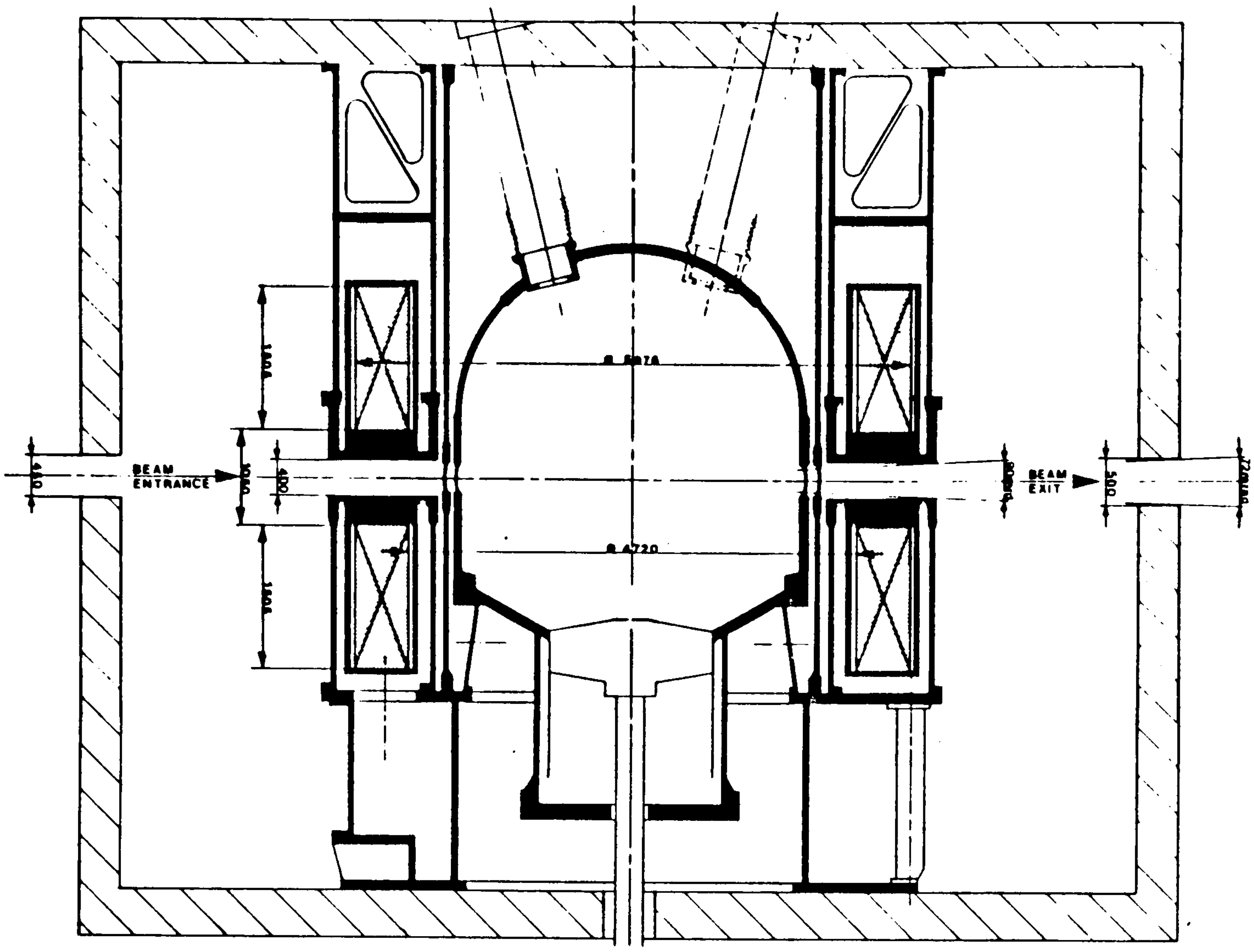

Figure 2.2: *Side elevation of BEBC*

2.1.2 The BEBC-IPF-EMI Detector

The Big European Bubble Chamber (BEBC)

BEBC is a cylindrical bubble chamber operated with liquid pure (99.8% para-) Hydrogen (H_2) at a temperature of 26 K . It has a diameter of 3.7m, volume of $35m^3$ and a hemispherical cap with five windows for the optical system (Fig. 2.2). The liquid has a radiation length of 8.9m and a hadronic absorption length of 7.9m. The stainless steel vessel has a wall thicknesses of at least 5cm and a mass of 45t, ensuring mechanical stability for the optical support structure with respect to the static pressure inside (5.3 bar) and the dynamical stress due to the expansion cycle. The conical bottom plane contains a piston that imposes volume changes of 0.75% in an isentropic expansion/recompression cycle of 115ms duration through a 11cm movement, resulting in a pressure change of more than 3 bar (Fig. 2.3). Since the SPS clock and the BEBC timing are synchronised, the expansion can begin before the decay neutrinos reach the detector. The density of the superheated hydrogen has decreased adiabatically from $0.0625 g/cm^3$, well within the liquid phase, by $0.0005 g/cm^3$ at particle injection time (4ms before the pressure minimum), crossing the boundary to the liquid+vapour phase. Thereby vapour bubbles are allowed to grow along charged particle tracks to a size of about $500 \mu m$, following a time dependence cst$\cdot\sqrt{t}$ [29] (Fig. 2.4). The size is dictated by the need to discern the bubbles by optical means. At this size, some of the bubbles join so that the effective bubble density is difficult to define. During the recompression the recondensation cannot keep pace with the volume change and is completed only after the cycle finishes. This is one limiting factor for the detector repetition rate.

The chamber volume is illuminated by annular xenon flash tubes whose light output is distributed through the liquid by highly reflective scotchlite wallpaper on the inside of the vessel. Since the vapour has a refractive index close to the one of the liquid, there is not enough light reflected from the bubbles for the purpose of recording. Instead, the ('bright field') light scattered away from them leads to a drop in light intensity according to all positions in the chamber where bubbles grow. Five wide angle cameras (Fig. 2.5) behind three-layer hemispherical windows on top of BEBC each cover the useful chamber volume of $22 m^3$. They are inclined by a stereo angle of 13^o to the vertical to give an accuracy of $0.3 mm$ for the reconstruction of tracks.

The chamber is surrounded by a magnetic system consisting of two superconducting coils. These have the advantage over conventional coils of low power consumption (about 1MW including cooling power) and a current (5700A) that is easier to stabilise. The produced magnetic field of 3.5 Tesla (that would require a

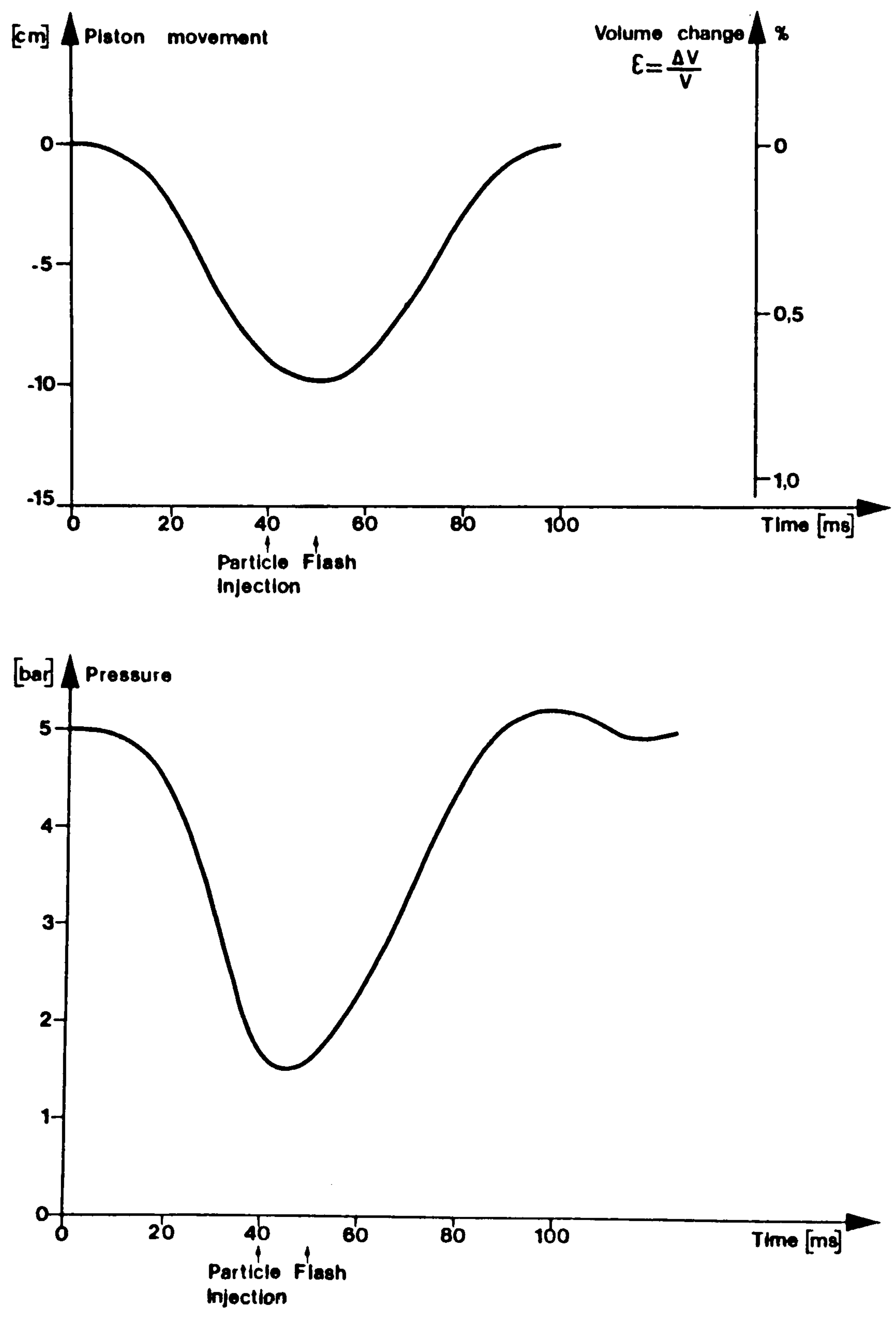

Figure 2.3: *Volume and pressure change during expansion cycle*

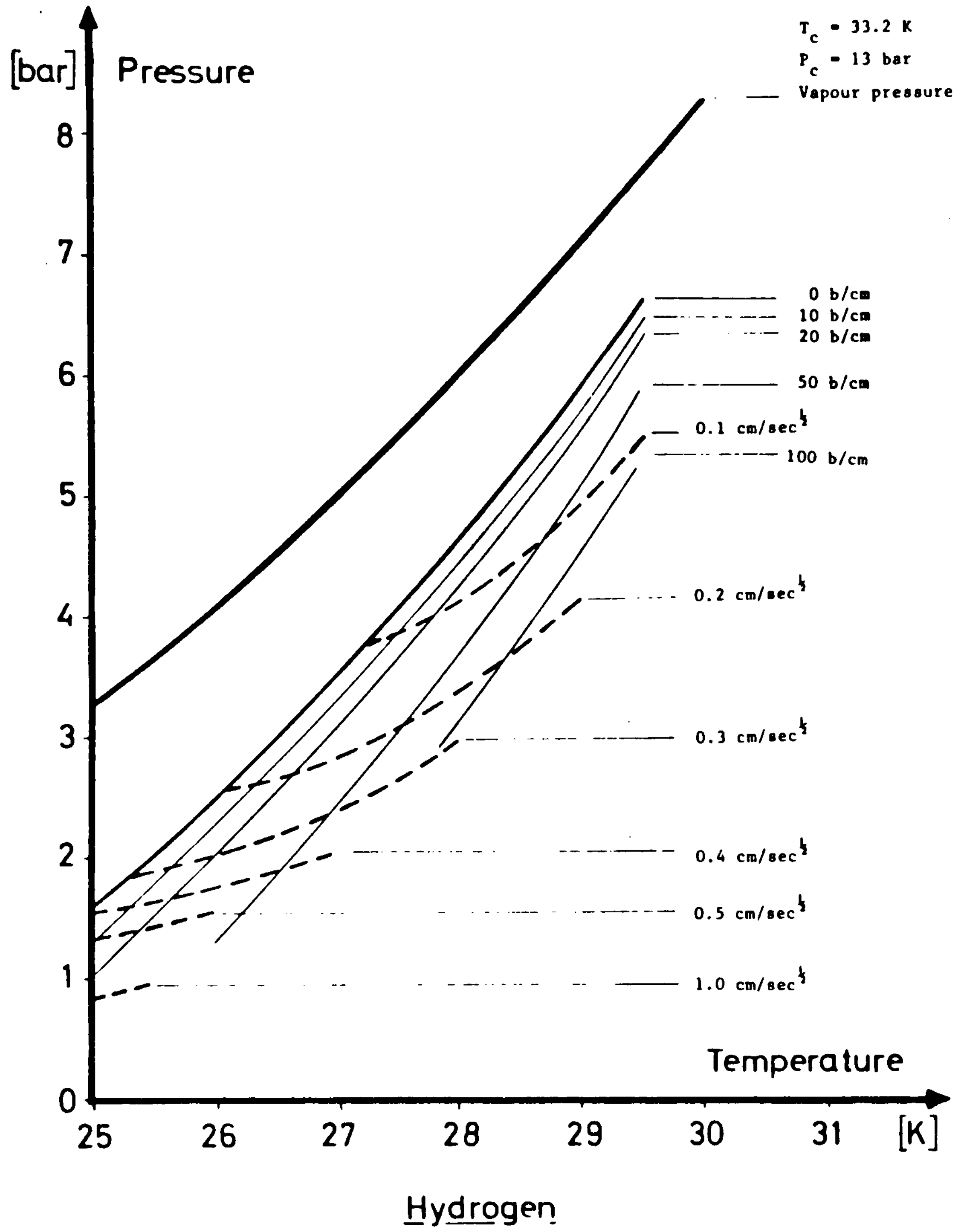

Figure 2.4: *Growth rate coefficient (dashed lines) and bubble density along minimum ionising tracks*

power of 60MW for a normal conducting magnet) is fairly uniform within the chamber (Fig. 2.6). It employs parallel niobium-titanium filaments of 0.2mm thickness, surrounded by copper and steel ribbon. The coils sit in cryostatic vessels where $20m^3$ of liquid Helium maintain the necessary temperature of 4.1K. The sign of the magnetic field is reversed for the antineutrino runs which allowed to leave the asymmetrical outer detectors (EMI, see below) in a fixed location.

The whole system is contained in a 2000 ton 50cm thick iron shield that confines the magnetic field lines and thus keeps the stray magnetic field outside, where control electronics and cryogenics are located, at tolerable levels. Further

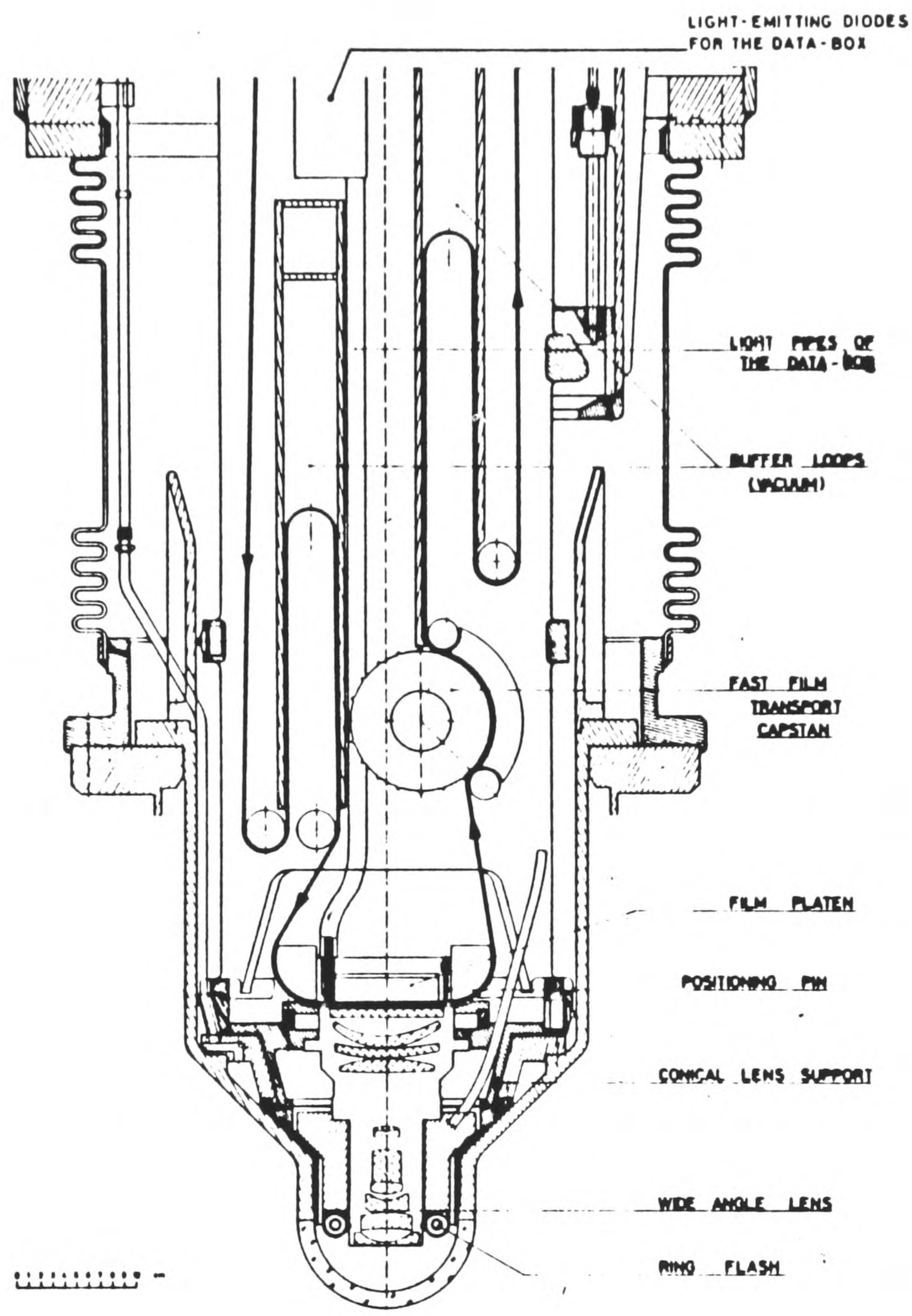

Figure 2.5: *Schematic drawing of the lens and camera system*

aspects of the chamber operation, and the run information are detailed in [37]

The External Muon Identifier (EMI)

The EMI has the task of detecting muons emerging from the bubble chamber with high spatial resolution, allowing a unique association of extrapolated tracks with EMI hit multiplets. To discriminate against hadrons (mostly pions and a few K_L^0), it is separated from the inner detector system by shielding in addition to the magnet yoke. Most hadrons are absorbed by this filter consisting of 50cm of lead (2.7 absorption lengths) and up to 1.7m of iron (3-10 absorption lengths). The detector

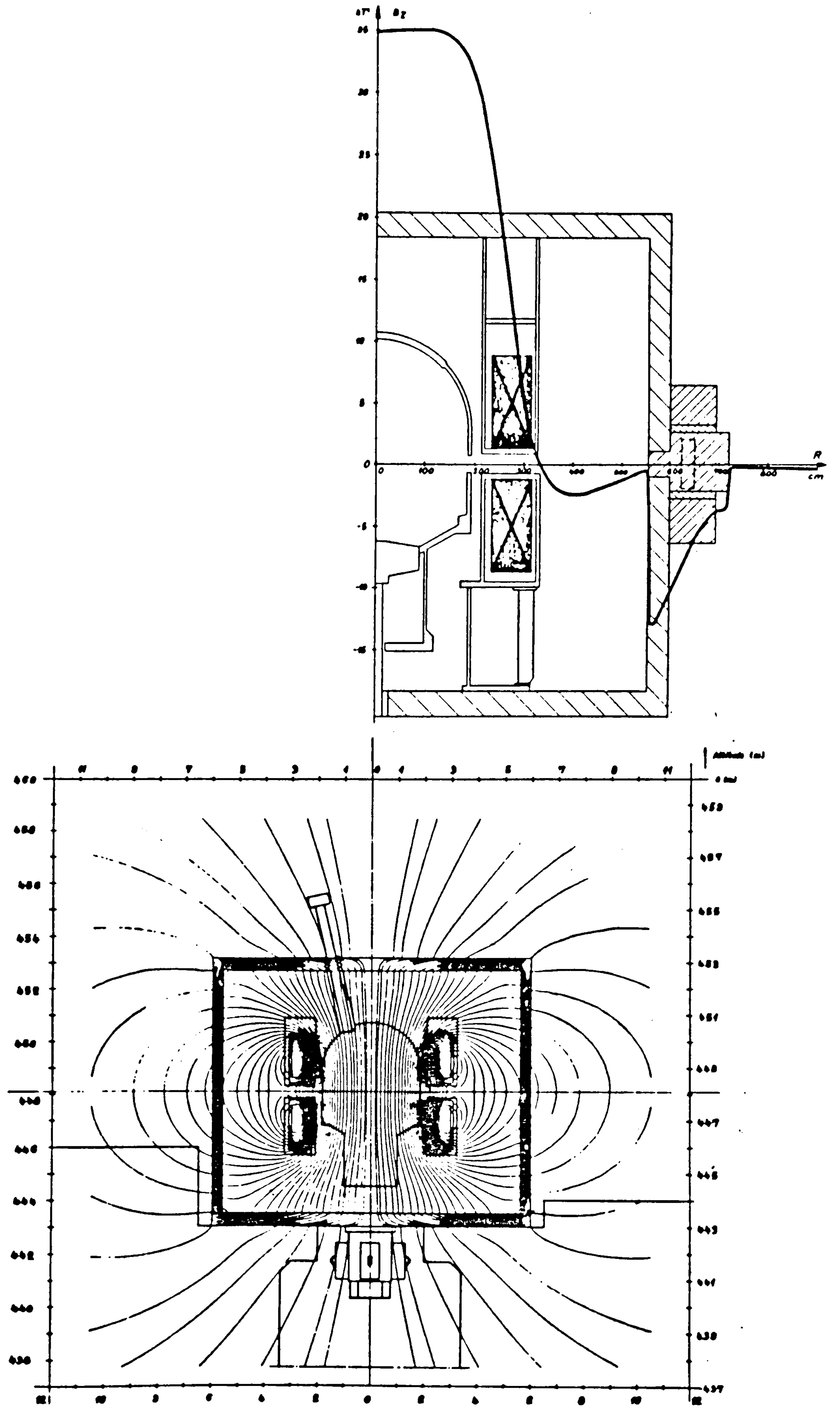

Figure 2.6: *Variation of the magnetic field B_z along the chamber axis (almost parallel to the beam), and lines of constant flux*

is designed to keep pion punchthrough to less than 1% and muon background from pion decay-in-flight to less than 0.1% . Muons, on the other hand, penetrate this amount of material easily since they do not interact strongly and suffer negligibly from electromagnetic Bremsstrahlung due to their large mass (compared to the electron mass).

The EMI is a single plane multiwire proportional chamber system with high modularity. Two anode planes, with $20\mu m$ wires seperated by 4mm and tilted to the vertical by $\pm 60^o$ ensure a spacial resolution of $\pm 0.5cm$. Each module gives three hit coordinates, two from the independent anode planes and one from the cathode strips. The gas used is Ar/CO_2 in a 70/30 volume percent mixture.

The EMI can process the large number of hits arising from muons that almost exclusively come from neutrino interactions upstream of BEBC (background), but must be recorded since the association to genuine neutrino induced tracks from within BEBC is off-line. Only one neutrino event is expected for every 4 frames taken, whereas up to 600 muons per beam spill can impinge on the outer EMI plane. This background is the limiting factor for the maximally acceptable beam energy for a given beam intensity. The data acquisition is self-triggering and defines $0.25\mu s$ 'timeslots' which contain, in addition to the hit data, monitoring information about the chamber performance. The detector system consists of 61 chambers with a sensitive area of 3m x 1m in three parts (see fig. 2.7):

a) A 'veto plane' upstream of BEBC to discriminate against incoming charged particles (6 chambers).

b) The 'inner plane' at a radius of 4m from the center of BEBC, covering azimuthal angles from -67^o to $+34^o$ horizontally and $\pm 18^o$ vertically (8 chambers).

c) The 'outer plane' at a radius of 7.5m covering the range -82^o to $+70^o$

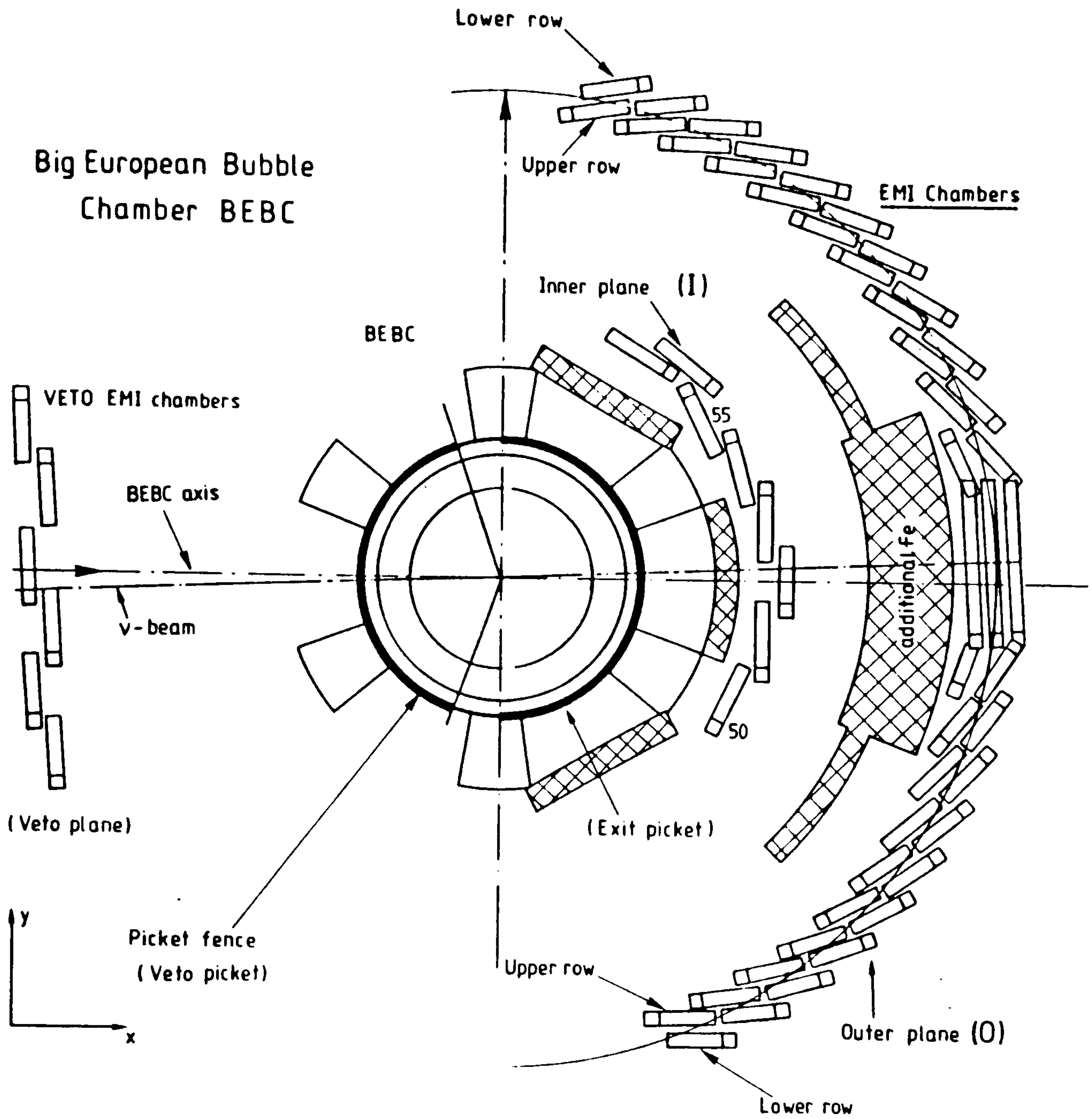

Figure 2.7: *Schematic layout of BEBC, EMI and IPF*

horizontally, and $\pm 20^{o}$ vertically combining an upper and a lower row, giving a total area of $144m^2$ (47 chambers).

The asymmetry is due to the fact that for a given beam type we expect muons of one charge sign only and can thus maximise the geometrical acceptance. The fine spatial and time resolution ($0.25\mu s$) enable the unique assignment of time windows to BEBC events in most cases, in particular the probability of false associations is very low. Details of the EMI performance can be found in [30].

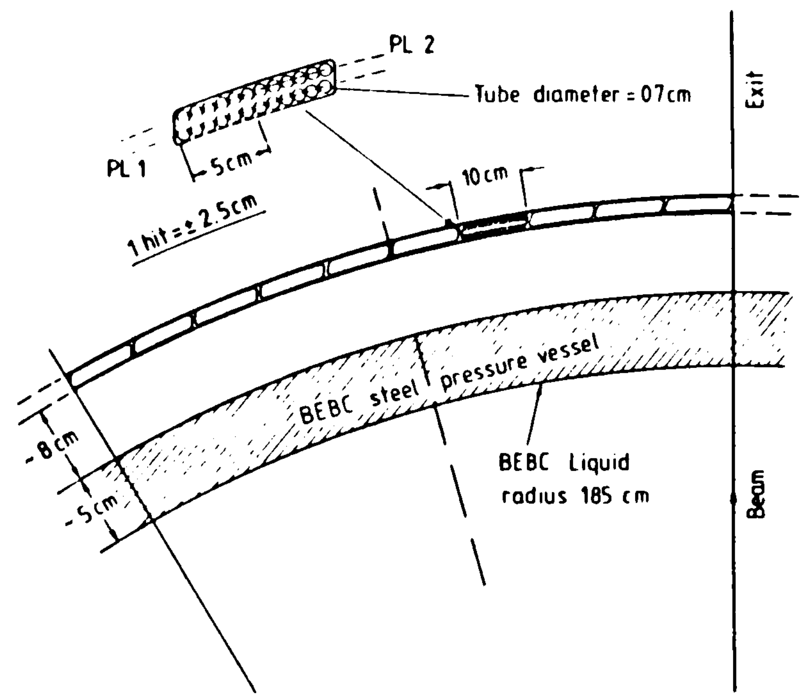

Figure 2.8: *Schematic diagram of IPF and BEBC wall; note the different scale in radius and azimuth*

The Internal Picket Fence (IPF)

From the 1981 runs onwards, BEBC has been equipped with a proportional tube system consisting of 2 vertical planes of 2.2m long tubes with an inner diameter of 7mm. They are positioned inside the BEBC cryogenic vacuum tank, separated from the liquid hydrogen by the vessel steel wall. They operate on a Ar/CO_2 70/30 mixture with $50\mu m$ gold plated tungsten wires at a voltage of 1.9kV and are arranged in a staggered double layer to minimise dead space, grouped as shown in figure 2.8. The coverage is 90% of the azimuth due to gaps for supplies which split the IPF into an upstream 'veto' part and a downstream 'exit' part. The purpose of the IPF system is

- to supply timing information for an off-line trigger. The time resolution of 230ns full width matches the one of the EMI and allows to use the same read-out electronics and simultaneous data storing in 250ns timeslots.
- to provide reliable indication of those timeslots with incoming neutral hadrons or muons, particularly for those cases when they are produced downstream of

the veto EMI (ie. in the shield and coils), in which case they could not be flagged using the EMI alone.

- to improve the overall efficiency for detection of low momenta muons from charged current events that contaminate the neutral current sample.

- to achieve some association of reinteracting neutrals that give rise to a second vertex within BEBC, enabling it to be merged later with the tracks from the primary vertex.

Since many event-related particles reach the IPF but not the EMI, the correlation between IPF hit timing and actual events in BEBC is much more efficient for the association of timeslots to events than the EMI timeslots alone. In addition it allows the off-line triggering to work for the neutral current class of events that are the main interest of this thesis, which by definition do not contain EMI data and thus have no EMI timing information. Hence by basing the decision about the event timeslot on IPF data treats CC and NC events with the same method, essential for any investigation sensitive to the absolute numbers of events of these types.

The inefficiency of the IPF system has been determined [31] to be 6.5% from through-going muons identified by the EMI, a value which is within 10% of the design figure, accounting for the two gaps (4.5%), the wall thickness (0.5mm) of the proportional tubes (1%) and spacer effects (0.3%).

2.2 Off-line Data Processing

2.2.1 Bubble Chamber Film Analysis

The number of photographs ('frames') taken during the 1981 and 1983 runs in the wideband (anti)neutrino beams is indicated in table 2.2.1. These are dis-

Beam/Year	BEBC frames
Neutrino	
Sep-Nov 1981	44,300
Oct-Dec 1983	79,800
Antineutrino	
Sep-Nov 1981	102,150
Oct-Dec 1983	148,500

Table 2.1: Number of photos taken with BEBC in the 1981 and 1983 run

tributed to the laboraties of the collaboration for the scanning and measuring process. The entire film is scanned twice for events that lie in the fiducial volume (see figure 2.2) of $18.9m^3$. Since there is no event-correlated triggering, this is the principal way to determine the frames containing neutrino events . Only later the combined information from the EMI and IPF in any one timeslot is used to predict leaving points of muons for charged current events and the film double scanned subsequently using the predictions.

During each scan the photographs from the different camera views are searched for vertices, and tracks are measured in conjunction with a geometry program [32] that incorporates the influence of the calculated magnetic field: the three-dimensional reconstructed tracks are fitted to a helix-type trajectory and for each mass hypothesis a four-momentum vector is calculated.

Due to the stereoscopic recording, a track of sufficient length L will give information about the polarity of the charged particle, its direction (parametrised by a dip and an azimuthal angle λ, ϕ), and the ratio of the modulus of the momentum to the electric charge, $|\vec{p}|/|e|$. The relative error on the momentum for a track measured over a distance L with dip angle λ is

$$\frac{\delta p}{p} \propto \frac{p}{L^2} \frac{1}{eB\cos\lambda}, \tag{2.7}$$

where the quantity actually measured is 1/p from the sagitta of the track.

The particle identity can usually not be determined, thus mass and energy are not known for the tracks. Slow Protons ($|\vec{p}| < 1.2GeV/c$) are often stopped and then identifiable. A few of the charged pions, Kaons and some muons decay within the liquid and can be classified by their decay kinematics or topological features of the track chain (kinks etc.). Slow electrons sometimes distinguish themselves through their characteristic spiralling due to their small mass. Some of these aspects can be seen on a BEBC photo of a fully reconstructed event in figure 2.9. Of the neutral particles, some of those which carry the additive flavour quantum number 'strangeness' (e.g. K^0 and Λ) decay within BEBC ($K^0_S \rightarrow \pi^+\pi^-$ and $\Lambda \rightarrow p\pi^-$). Their secondaries appear as a vertex with a V-shaped topology that can be linked to the primary vertex when the timing information of the IPF is checked. Unfortunately, only very few of the stable neutrals n, γ are detected in Hydrogen, which leads to a substantial loss in the energy sum of all secondaries produced. The conversion probability for photons in hydrogen is only 7% due to the radiation length exceeding the size of BEBC. Thus the π^0, n component of the hadronic shower will excape almost always undetected. The output of the measuring process are so-called Geometry Summary Tapes (GSTs).

2.2.2 Data Production Software Chain

The offline software now has to merge the information from the films with the electronic data of the IPF and EMI. This is done in several steps which are mapped schematically in fig. 2.2.2.

In the EMI step [33] the measured tracks are extrapolated to the plane to which their momentum allows them to penetrate. Using the magnetic field information, this takes into account the energy loss in the different traversed materials, multiple Coulomb scattering and track measurement errors. An association χ^2 is

Figure 2.9: ***Reconstructed charm production event in BEBC***

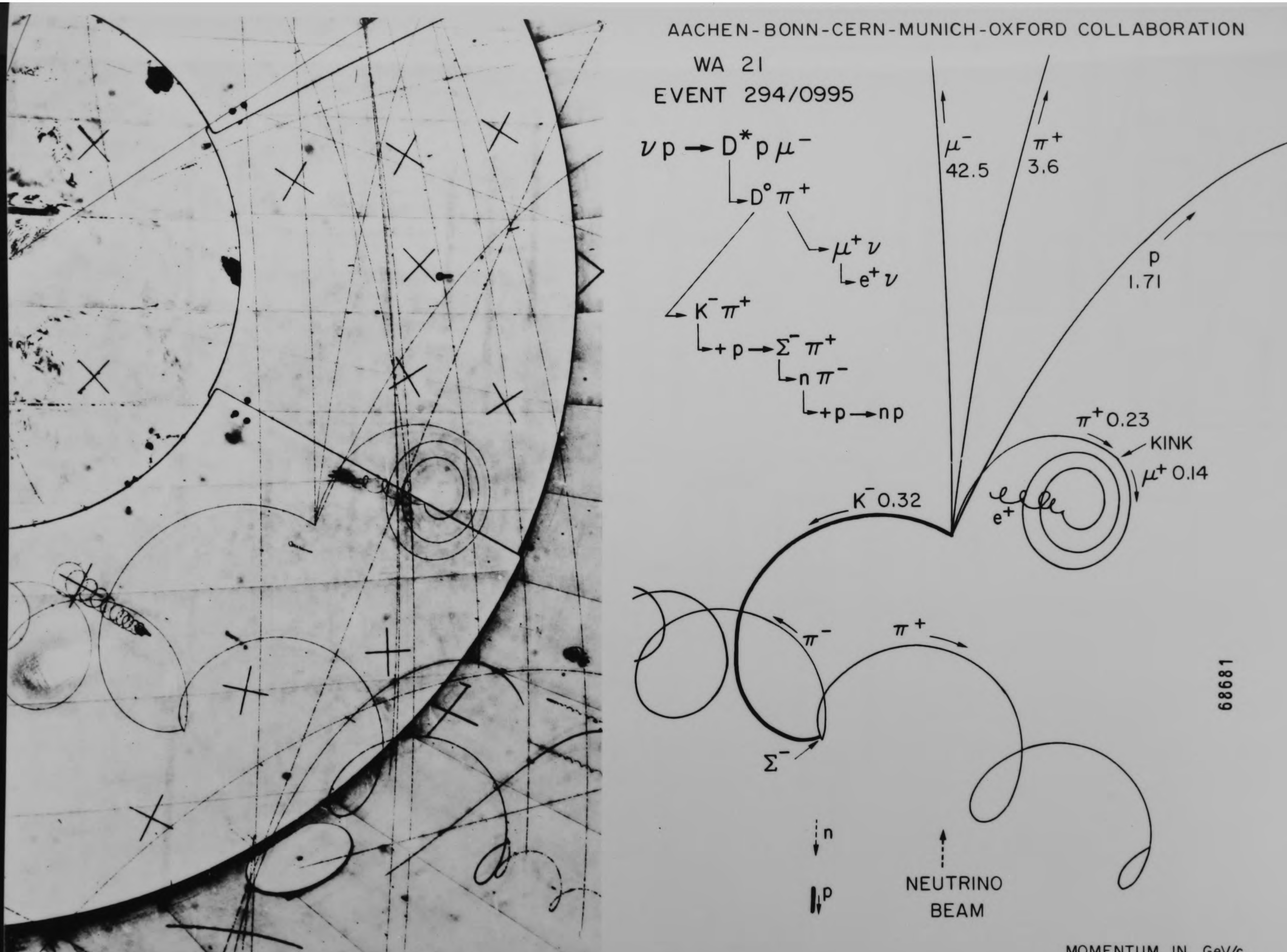
AACHEN-BONN-CERN-MUNICH-OXFORD COLLABORATION
WA 21
EVENT 294/0995
$\nu p \rightarrow D^{*} p \mu^{-}$
$D^{\circ} \pi^{+}$
$\mu^{+} \nu$
$e^{+} \nu$
$K^{-} \pi^{+}$
$+ p \rightarrow \Sigma^{-} \pi^{+}$
$n \pi^{-}$
$+ p \rightarrow n p$
μ^{-} 42.5
π^{+} 3.6
p 1.71
π^{+} 0.23
KINK
μ^{+} 0.14
e^{+}
K^{-} 0.32
π^{-}
π^{+}
Σ^{-}
n
p
NEUTRINO BEAM
68681
MOMENTUM IN GeV/c

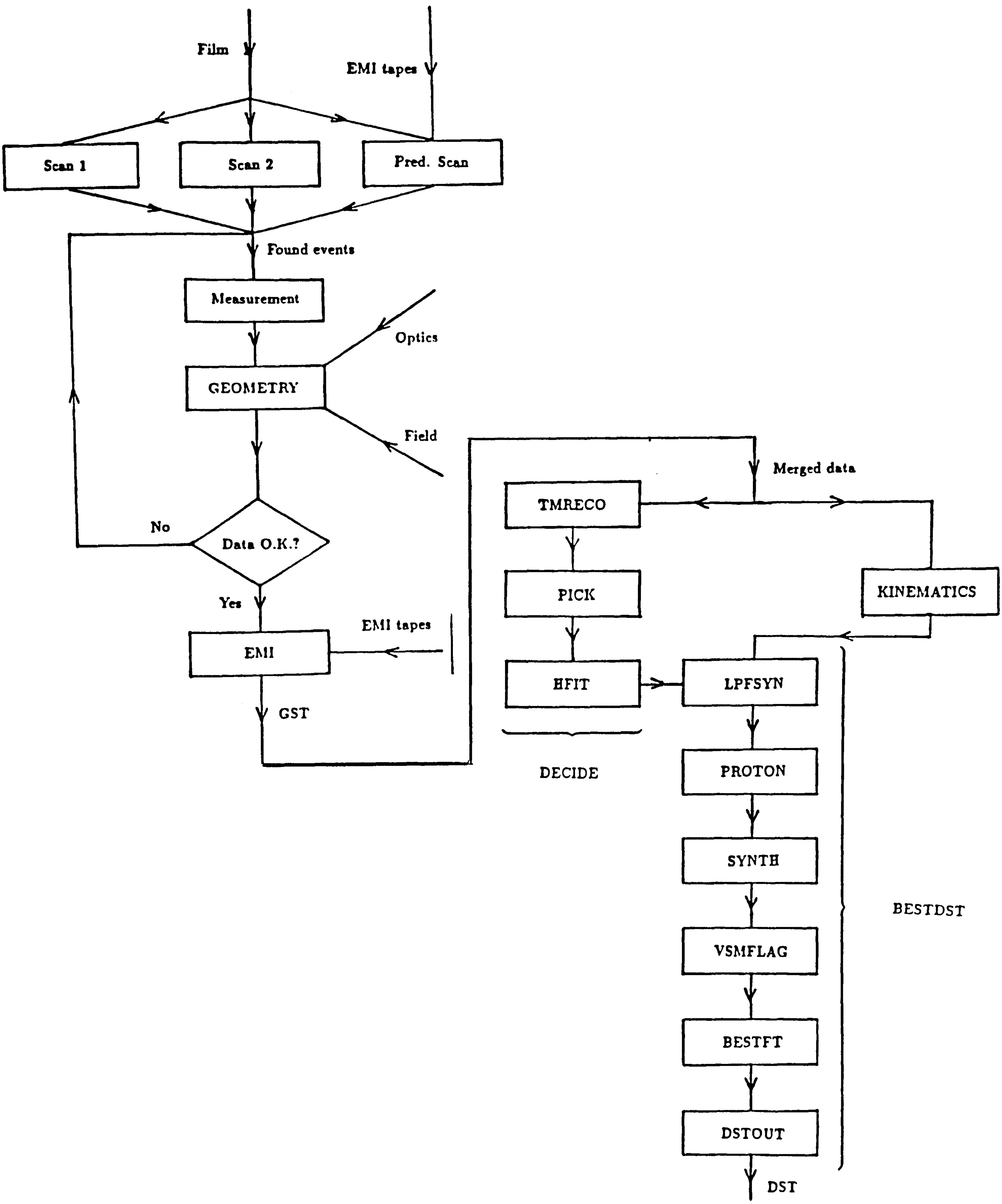

Figure 2.10: a) *The scanning and measuring process* b) *The off-line processing chain*

calculated from the extrapolated hit positions in the downstream detector planes and the actual hits therein, for each timeslot. If the association is of acceptable quality, the actual hit is defined to be an 'associated hit'. This gives the number of associated and unassociated hits per timeslot.

In the DECIDE step [34] the two main tasks are the decision of whether a unique 'event time slot' can be found, and the identification of muons, including those which do not arise from an interaction within BEBC ('through-going muons'). This is done by considering the hit patterns in the EMI IPF system. If a track has hits in both downstream EMI planes with a sufficiently good association χ^2 , it is assumed to be a muon. Then the EMI timing information can be useful in case the timeslot is ambiguous so far. In case it is uniquely defined, in addition all those tracks that hit the exit IPF only and one EMI plane are considered to be muons. To improve the momentum measurement, then a hybrid fit includes the EMI hits as additional constraints which usually results in smaller errors on the fit parameters for the track.

In the KINEMATICS step [35] four-momentum conservation can prove useful, in events where all secondaries are observed, to try various patterns of mass assignments for the tracks. Since for charged current events the outgoing lepton four-vector is determined, only the beam energy is unknown (for neutral current events only one parameter, the vanishing mass of the neutrino is known about the outgoing lepton, and hence four parameters have to be obtained from four constraints) A 3C (0C) fit can then determine whether a particular mass combination is consistent with energy-momentum conservation up to those variations permissible by the obtained measurement errors. Since most events have missing tracks, this proc dure is only sucessful in a small subset of the data, and even for completely reconstructed events the decision about the mass assignments is often not unique.

0C fits are also tried for charged current events under the assumption that a final state neutron is unobserved. Since these 0C fits are often found incorrect, none of them is accepted.

In the BESTDST step [36] the main purpose is the linking of secondary vertices to the primary vertex. This is done on the basis of the IPF timing information (SYNTH). Oviously, in the few cases where a successful kinematics 3C fit has identified the secondary vertex to be a genuine neutrino interaction, we cannot link it (two primary vertices on one frame). Since the linking is done in disregard of the type of neutral connecting the two vertices, it is assigned to be a neutron by default. In cases of a linked two prong decay, the neutral is assigned to a K^0 or Λ unless the kinematics fit has identified it as a photon conversion. Up to one slow proton is allowed to be identified as a stopping track. Then the timeslot decision is improved (VSMFLAG) for cases where it is not yet unique, by using the timing of associated hits in the inner EMI plane. Track pairs extrapolating to the same EMI hits (fake dimuons) are resolved by taking the track with the larger momentum to be the muon.

Finally, DSTOUT writes the obtained information on Data Summary Tapes (DSTs). It determines which mass assignment is defined as the best one, in the order: from the best kinematics fit, from the decision by another program, from the track type that is set by the scanner and checked by a physicist, or from the Geometry fit. All unidentified particles are supposed to be pions.

Chapter 3

A new Approach to NC $x_{(Bj)}$-Distributions

3.1 Introduction

In neutral current (anti)neutrino interactions the knowledge of the kinematic variables - apart from those which characterise the hadronic system or individual final state particles - is rather limited. Without measuring the outgoing neutrino four-momentum, an ideal experiment would still allow to calculate all kinematic variables using energy momentum conservation, given completely determined incoming and outgoing hadronic four-momenta and the direction of the neutrino beam. However, due to experimental resolutions and losses of neutrals, it is impossible, for instance, to associate meaningful values of the scaling variable $x_{(Bj)}$ with individual events. This state of affairs contrasts with the fact that the distributions of neutral current (NC) events with respect to these scaling variables would be very interesting in the framework of the quark parton model description of deep inelastic neutrinoproduction. In addition to revealing the nucleon momentum composition, as it appears to the neutral carrier Z^0 of the electroweak force, neutral current structure functions incorporate the chiral couplings of the quark transition currents to the Z^0 boson [39].

We are primarily concerned with resolving this problem for a fixed target setup including a detector for which the probability to lose an outgoing particle is not directly correlated with its direction with respect to the beam (an indirect correlation will always enter because the loss probability depends on the position of the interaction vertex in the fiducial volume). This is, for instance, the case for a bubble chamber where target and tracking detector coincide and are to a good approximation homogeneous, but also, within a restricted polar range, for massive electronic detectors for fixed target experiments like CDHS.

One faces a related problem with determining $x_{(Bj)}$ in a collider setup like HERA for both charged and neutral current interactions. But here, the longer the track length inside the beam pipe of a produced 'forward' secondary, the larger is the likelihood not to observe it (direct correlation), and indeed a sizeable part of the proton fragments will evade detection. However, firstly, the full incoming (and outgoing, for NC) electron four-momentum is known. Secondly, the event transverse momentum is little affected by the losses in the forward direction and it is this quantity which is more relevant for the determination of Q^2 and hence x than the longitudinal momentum. Thus it has been shown [40] that it is possible to assign reasonably correct values of x to individual events in most cases. The method relies on the separation of the secondary hadrons into a current and a spectator jet, notions that cannot be transcribed naively from a hard scattering framework to the soft fragmentation process. Since the spectator jet will in general have nonzero invariant mass there is a systematic shift between the true and estimated values of the scaling variables that is worst at large $x_{(Bj)}$ and small Q^2, as has been demonstrated in [41].

Evidently, the amount of information represented by a determination of x on an event by event basis exceeds the information contained in the distribution $F(x) = \frac{1}{N}\frac{dN}{dx}$ in x. One way to exploit this simple fact and to circumvent the problem outlined in the first paragraph is to fit an event distribution in accurately measured variables to a convolution of their experimental resolution functions with an assumed parametrisation for $F(x)$. This method could be used, for instance, in a narrow band neutrino beam experiment to obtain $F(x)$ for neutral current interactions from an event distribution in vertex position, hadronic energy and angle with respect to the neutrino beam [42], [43] . Of course, the advantages of using a narrow band beam as well as an efficient detection of neutral secondaries proved crucial in such an investigation. However,this approach leaves open the question whether the extracted $F(x)$ is uniquely determined by the procedure.

We present here a new approach to the problem of measuring $F(x)$ in (anti)neutrino neutral current interactions. Although this is the aim for which the method was developed, it will become clear that it is applicable to charged current (anti)neutrino interactions as well as to other leptoproduction processes where more information about the leptonic current is available than in our case. In those applications it would provide a method to obtain $F(x)$ independent from the usual method which relies on the measured outgoing lepton four-momentum. We shall require the method to work even for an experiment with hydrogen target where few of the outgoing neutrals (γ, n, K_L^0) are detected. It will yield a unique $F(x)$ through a direct, analytic procedure, given as input the distribution in a hadronic scaling variable which we can measure with sufficient accuracy. Apart from this the only other piece of information required is independent of the x distribution we are going to extract and concerns the marginal distribution in Bjorken-y.

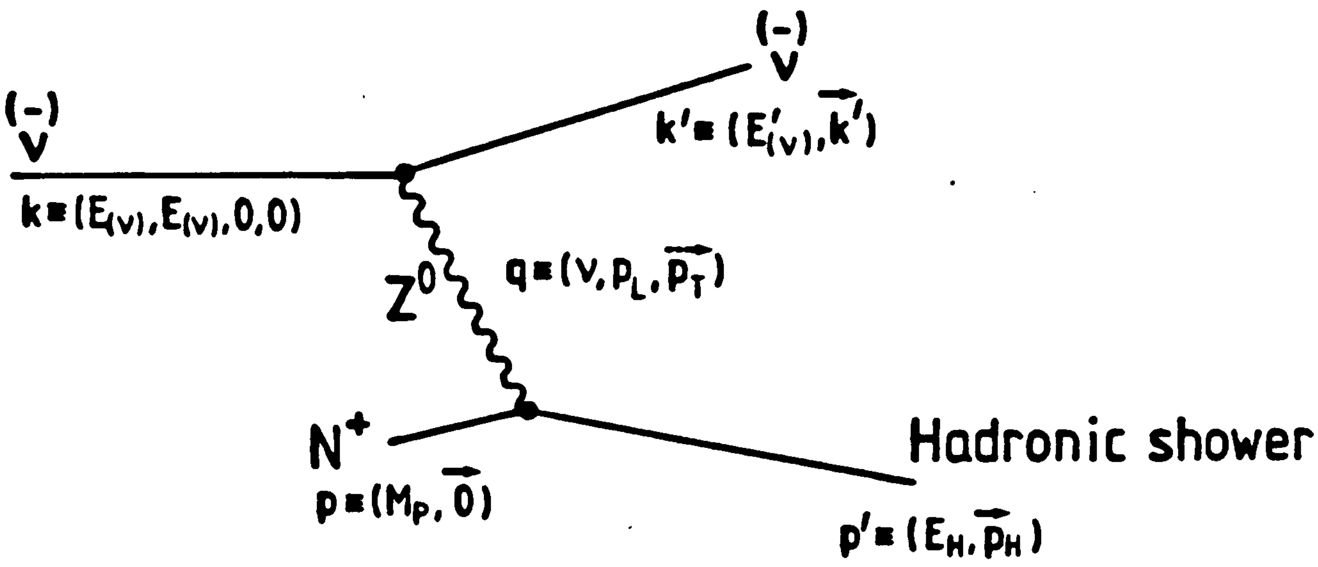

Figure 3.1: *Tree level approximation to (anti)neutrino proton NC scattering*

3.2 The Measurable Part of $x_{(Bj)}$

We define the four-momenta of the (anti)neutrino proton collision $\overset{(-)}{\nu} N^+ \to \overset{(-)}{\nu} X$ in the laboratory frame by (see figure 3.1)

$$\overset{(-)}{\nu}: \quad k = (E, E, \vec{0}), \qquad \overset{(-)}{\nu}{}': \quad k' = (E', k'_L, -\vec{p}_T) \tag{3.1}$$

$$Z^0: \qquad q = k - k' = (\nu, p_L, \vec{p}_T) = p - P \tag{3.2}$$

$$N^+: \quad P = (M, \mathbf{0}), \qquad X: \quad p = (E_H, p_L, \vec{p}_T). \tag{3.3}$$

Here, M is the proton mass, $p_{L,T}$ are taken with respect to the beam axis, $p_T = \sqrt{\vec{p}_T^2}, \mathbf{p}_H = (p_L, \vec{p}_T)$, and three dimensional momenta are boldface.

Initially, we have attempted to estimate the incoming neutrino energy E from measured hadronic variables alone, an aim that was found impossible to reach using the charged part of the hadronic shower only. Realising that the neutrino energy can be written in the form

$$E = \frac{Q^2}{2(p_L - \nu)}, \quad Q^2 = \mathbf{p}_H^2 - \nu^2, \tag{3.4}$$

we are suggested that the unmeasureability of E is not only due to the one of Q^2, but also due to the one of the difference $p_L - \nu$ of two large scales that have to be equal to within M_P (obvious from eqn. 3.9 below).

The idea now is to split $x_{(Bj)}$ into two parts in such a way that only one of them is severely affected by the experimental resolutions and losses. The true value of this latter part need *not* be small compared to x in general. Let us recall how the momentum fraction ξ of the scattering parton inside the nucleon emerges in the quark parton picture. Assuming the scattered parton to be real with mass m, the usual Ansatz $m^2 = (\xi P + q)^2$ gives, with $Q^2 = -q^2$:

$$\xi = \frac{Q^2 + m^2}{M(\nu + \sqrt{\nu^2 + Q^2 + m^2})} \overset{m^2 \ll Q^2, \nu^2}{\approx} \frac{Q^2}{M(\nu + \sqrt{\nu^2 + Q^2})} \tag{3.5}$$

Instead of taking $Q^2 \ll \nu^2$ already here, we carry the exact expression one step further to obtain

$$\xi = \frac{Q^2}{M(\nu + |\mathbf{p}_H|)} = \frac{|\mathbf{p}_H| - \nu}{M} \tag{3.6}$$

The crucial point is the observation that the small positive quantity $p_L - \nu$ is almost exclusively responsible for the experimental inability to measure ξ. Neglecting terms of the order $(\frac{p_T}{p_L})^4$ we find

$$\xi \approx w + \frac{p_L - \nu}{M} \tag{3.7}$$

$$\text{with } \; w \equiv \frac{p_T^2}{2 p_L M} \tag{3.8}$$

This approximation makes an error which is smaller than $(\frac{p_T}{p_L})^3 \frac{p_T}{8M}$. However, to perform the Bjorken limit, ie. to identify ξ with $x_{(Bj)}$, we see from (3.5) or (3.6) that we must have $Q^2 \ll \nu^2$, ie. $p_T^2 \ll \nu^2$ because of the positiveness of $p_L - \nu$ (recall that $Q^2 = p_T^2 + (p_L + \nu)(p_L - \nu)$). Thus $(\frac{p_T}{p_L})^2 \leq (\frac{p_T}{\nu})^2 \ll 1$, i.e. the Bjorken limit is identical with the approximation made for (3), and we can write

$$\xi = x = \frac{p_T^2}{2 p_L M} + \frac{p_L - \nu}{M} \tag{3.9}$$

This holds *exactly*, in the sense that it is an exact statement whenever the interpretation of the Lorentz invariant quantitiy $x = \frac{Q^2}{2q \cdot P}$ in terms of ξ is meaningful. The basis for the forthcoming derivations comes from the identity $p_L - \nu = MQ^2/s$, which gives $p_L - \nu = xyM$ and thus

$$w \equiv \frac{p_T^2}{2p_L M} = x(1-y) \iff \xi = x \tag{3.10}$$

This uses $s = 2ME$ neglecting a term M^2 in s. From the well-known form of (anti)neutrino cross-sections it follows that $\frac{d\sigma}{dw}$ approximately scales in s, as can be seen also directly from definition (3.8), since $p_{T,L}$ scale like $\sqrt{s}$ and s, respectively.

We shall now focus on what can be learnt from a distribution in w. The important property of this quantity is that the associated experimental resolution is sufficiently narrow to be able to correct the measured w values, even for a hydrogen target and the ensuing incompletely reconstructed hadronic system. It has its origin in the fact that the $\frac{p_T}{p_L}$ of the seen hadronic system will on average not differ much from its true value, a fact which is also the basis of the Myatt method [45] (and its extensions [46]) of transverse momentum balance for the estimation of the neutrino beam energy from the collected hadronic energy in a bubble chamber. The main systematic correction to the seen w will be due to a slight underestimation of the event transverse momentum.

We perform a variable change and view it profitably as the two-dimensional transformation

$$\begin{pmatrix} x(1-y) \\ y \end{pmatrix} = \begin{pmatrix} w \\ y \end{pmatrix} \longmapsto \begin{pmatrix} x \\ y \end{pmatrix} \tag{3.11}$$

This is effectively half a Jacobi transformation and maps the unit simplex in the (w, y) plane into the unit square in (x, y), see figure 3.2. We denote the distributions in x, w, and (x, y) by $F(x), G(w)$, and $h(x, y)$, respectively, and they are assumed normalised to unity throughout. Thus, for instance, $G(w) = \frac{1}{N}\frac{dN}{dw}$. We can then obtain an expression for the marginal distribution in w, either locally through a transformation of the density in $x_{(Bj)}$ and $y_{(Bj)}$, or explicitly by integrating a density in $y_{(Bj)}$ and w over a narrow strip in w, and $h(x, y)$ over its image under the

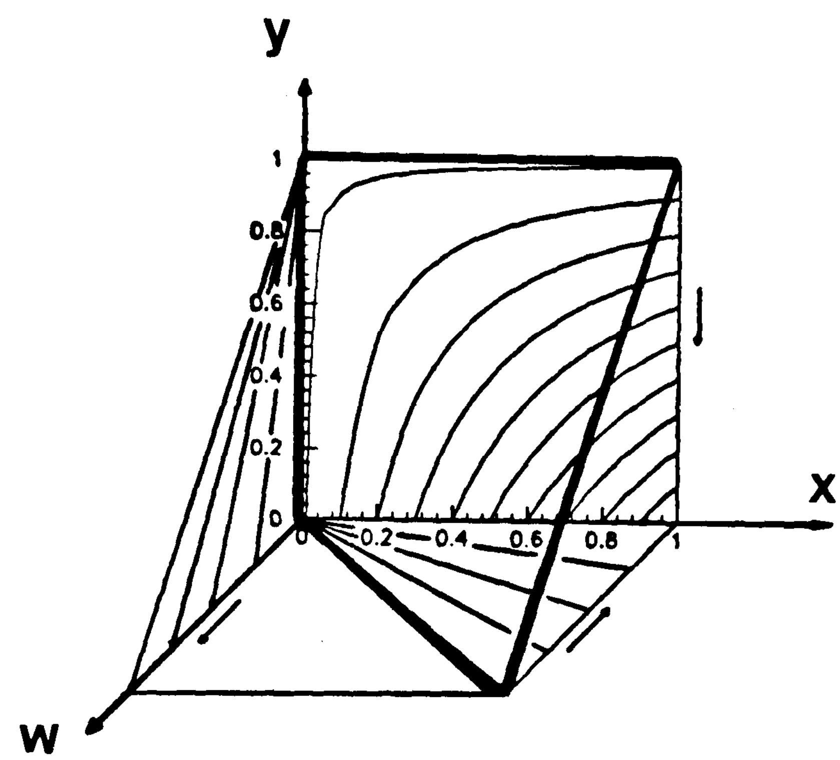

Figure 3.2: *Mapping between planes each spanned by two independent scaling variables out of w, x, y. Lines of constant w in the x, y plane, of constant x in the w, y plane and of constant y in the w, x plane are shown.*

transformation (3.11)

$$G(w) = \int_w^1 dx \, \frac{h(x, 1 - \frac{w}{x})}{x} \tag{3.12}$$

Note that a flat $h(x, y) = cst = 1$ would lead to $G(w) = |\ln w|$. This comes from the behaviour of the lines of constant w in the $x - y$ plane, resulting in a non-trivial functional determinant for (3.11).

It is always possible to decompose h into $h(x, y) = h(y|x)F(x)$ where all the conditional densities $h(y|x)$ for a given x are normalised to unity. This gives the central relation between the x and the w distributions:

$$G(w) = \int_w^1 dx \, \frac{h(1 - \frac{w}{x}|x)}{x} \, F(x) \tag{3.13}$$

This Volterra integral equation of the first kind can be solved analytically if we assume $h(y|x)$ to be independent of x. Otherwise one can resort to numerical techniques. [1]

[1] Formally $F(x)$ can certainly be written simply as $F(x) = \int_{\Omega_x} dw \; k(x|w)G(w)$. However, then, not only the integration region $\Omega_x = [0; x]$ depends on x, but the kernels $k(x|w)$ do not constitute information independent of the desired x-distribution.

Obviously, the true conditional y distributions $h(y|x)$ are not independent of x, although their variation with x is weak. However, we are aiming at reconstructing the x distribution for an observed event sample which represents some subset of the $3m$ dimensionsal phase space (m being the maximum multiplicity) specified by the cuts used. In particular, cuts in the invariant hadronic mass W and the hadronic energy E_H will deplete the low y region. For fixed small $y_{(Bj)}$, a minimum $E_H = \nu + M_P$ translates into a minimum $E_{(\nu)} = \nu/y$, ie. of the flux $\Phi(E)$ which determines the seen number of events at this fixed $y_{(Bj)}$, we integrate only the large E part, where the flux is small. Furthermore, for fixed W, $y \geq \frac{W^2-M^2}{s_{max}}$. These tendencies cause the observed $h(y|x)$ to vanish for $y \to 0$ for a real experiment, an effect which is independent of x and which is the basis of the quasi-independence of the observed $h(y|x)$ on x. In other words, the biased sampling of the 'inclusive' NC phase space by an experiment turns out to be advantageous in this context.

For neutrino interactions, the true marginal y distribution H is almost flat in y, whereas the observed $h(y|x)$ as well as the observed marginal $H(y)$ are found to be best fitted by the one-parameter functions

$$h^{(\nu)}(y|x) \approx H_a^{(\nu)}(y) = \quad N_a \left(1-(1-y)^a\right), \tag{3.14}$$

$$N_a \; = \tfrac{a+1}{a} \tag{3.15}$$

which are normalised to unity by N_a and allow for the fall in H for $y \to 0$. Now one can convert (3.13) into a differential equation whose uniquely determined solution with $F(1) = 0$ is

$$F^{(\nu)}(x) = \frac{1}{N_a a}\left(x^2 G''(x) - (a-1)xG'(x)\right) \tag{3.16}$$

The result is completely general as to the (eventually measured) dependence of G on its argument. [2] The form of (3.16) deserves some remarks: the obtained F(x) is

[2]In course of solving (3.13), using (3.15), the fact that the kernel $\frac{H(1-\frac{x}{x})}{x}$ vanishes for $w = x$ ie.

a linear superposition of two solutions $F^{flat}(x) = -xG'(x)$ and $F^{lin}(x) = \frac{1}{2}x^2G''(x)$ for a fictitious flat $H(y \neq 0) = 1 \quad (a \to \infty)$ and a linear $H(y) = 2y \quad (a = 1)$, respectively, the mixture being determined by the steepness of $H(y)$ represented in a. Below we shall show that the dependence of F on a is actually extremely weak. The structure of F

$$F(x) \propto \sum_{n=0}^{2} c_n(a)x^nG^{(n)}(x), \tag{3.17}$$

where $G^{(n)}$ is the nth derivative of G with respect to its argument, is thus common to a variety of shapes for $H(y)$ and stems rather from the connection (3.13) between F and G. It suggests, for monotonic $G^{(n)}$, G falling, the qualitative unimodular behaviour of $F(x)$.

The antineutrino case requires a more elaborate ansatz for $H(y)$, since the true $H^{\bar{\nu}}(y)$ falls for $y \to 1$, and a sufficiently general parametrisation involves a third term in $1-y$:

$$\begin{aligned} h^{(\nu)}(y|x) \approx H_a^{(\nu)}(y) &= N\left(1-(1+c)(1-y)^a + c(1-y)^b\right),\ c \geq 0 &(3.18)\\ N &= \frac{(a+1)(b+1)}{(ab+C)} &(3.19)\\ C &= a+(a-b)c &(3.20)\end{aligned}$$

For this ansatz a more complicated linear differential equation emerges from the corresponding integral equation, but an analytical solution for an arbitrary $G(w)$ can again be given; it has an identical structure to that in (3.16) except for an additional term which is finite at $x=0$ and depends on the behaviour of G over the range $w = x$ to $w = 1$:

$y = 0$ is steering the calculation. But $H_a^{(\nu)}(y)$ for $a \to \infty$ converges towards the constant function $H = 1$ while retaining $H(0) = 0$. This convergence being non-uniform, it is worth checking that the $F_a(x)$ stemming from $H_a(x)$ converge, with $a \to \infty$, towards the solution F(x) obtained by using $H \equiv 1$ and performing the calculation accordingly differently. We confirmed that one gets $F(x) = -xG'(x)$ in both cases, showing that we are clear of mathematical intricacies.

$$F(x) = \frac{1}{NC}\left(x^2G''(x) - (A-1)xG'(x) + B\,G(x)\right) - \tag{3.21}$$
$$- B\frac{ab}{NC^2}\int_x^1 dw\,\frac{G(w)}{w}\left(\frac{x}{w}\right)^{ab/C}$$

where

$$A = a + b(a-b)c/C \tag{3.22}$$
$$B = (1-\frac{ab}{C})(A-1) + (a-1)(b-1) \tag{3.23}$$

The normalisation to unity of the $x_{(Bj)}$ distributions in (3.16) and (3.22) follows from the fact that the $G(w)$ are normalised to unity. From the formulae for A, B, C, N one reobtains the simpler form of the neutrino case solution (3.16), ie. $A = a, B = 0, (NC) = a+1$, in each of the three limits $a \to b, b \to 0$ and $c \to 0$.

3.3 Extracting the x-distribution

At this point, we want to outline the general strategy of an analysis based on the method presented here. All distributions we have mentioned are supposed to refer to data at the stage when backgrounds have been subtracted and resolution effects have been removed. On the other hand, the data is still affected by experimental 'acceptance' losses due to the effects of the kinematical cuts imposed (cf. discussion after (3.13)). Thus, a complete analysis would proceed in three steps:

- Subtraction of backgrounds, and removal of resolution effects from the observed w-distribution, requiring a simulation of the detector
- Application of the formulae of the preceding section to obtain $F(x)$ corresponding to this corrected data, using the marginal $y_{(Bj)}$ distributions that follow from the known $y_{(Bj)}$-dependence of the cross-section and the effects on it of the kinematical cuts imposed

- In case cuts not related to fundamental quantities have been applied, correction of $F(x)$ taking into account their effects, to yield an x-distribution which is largely independent of the experimental apparatus. The correction can in principle be applied already in the first step, directly to the w distribution.

The purpose of this chapter is to describe a procedure which achieves step two, despite the fragmentary knowledge of the event explained in the beginning. Thus, 'true' Monte Carlo events (ie. without resolution broadening) will be used to demonstrate its performance by comparing $F(x)$ arising from an initial $G(w)$ via our method to the x-distribution which corresponds exactly to that data, inaccessible to direct measurement in a real experiment. The analysis based on this method using bubble chamber data of an (anti)neutrino hydrogen scattering experiment follows in chapter 5.

Any application of the method to real data must of course check that the resolution in w is sufficiently narrow to be able to reconstruct the 'true' $G(w)$ in the above sense from the raw w distribution, without introducing a bias towards $G(w)$ during the correction. [3] More quantitatively, step one corresponds to the extraction of $G(w) = A(w)G_0(w)$ from the observed w distribution that can be written

$$\tilde{G}(\tilde{w}) = (1 + \sigma(\tilde{w})) \cdot \left(\int dw \; R(\tilde{w}, w) A_w(w) G_0(w) \right) + \beta(\tilde{w}) \qquad (3.24)$$

where $A_w(w), R(\tilde{w}, w), \sigma, \beta$ represent the 'acceptance' due to cuts, resolution transform, statistical fluctuations, and background distribution in w, respectively, and $G_0(w)$ is the theoretical w distribution free from all dependence on the experiment. If necessary, the third step takes as input the result $F(x) = A_x(x)F_0(x)$ of our method and transforms it into an $x_{(Bj)}$ distribution $F_1(x) = A_1(x)F_0(x)$ with cuts

[3] In the framework of neutrino scattering in liquid hydrogen in BEBC we found this condition to be satisfied. There the resolution, defined as the standard deviation of the conditional distributions $R(\tilde{w}|fixed\Delta w)$ rises slowly from 0.02 for $\Delta w = [0.00;0.05)$ to 0.08 for $\Delta w = [0.45;0.50)$. $\tilde{w}$ is the observed value of the true w, see chapter 5.

on fundamental quantities only. It should be noted that we are always interested in an $x_{(Bj)}$ distribution that is defined in the deep inelastic region and corresponds to (a set of) cuts, their effects on F_0 represented by $A_x(x)$, which ensure that the resonance region is excluded. Thus $F_0(x)$ is not the object one is primarily trying to obtain, but rather $F(x)$ such that $x_{(Bj)}$ is confined to a physically relevant domain.

The fact that the $y_{(Bj)}$ distributions are assumed known is common to most structure function analyses that aim at extracting the dependence of the cross-section on $x_{(Bj)}$ and Q^2. When the incoming lepton energy flux is integrated over, for fixed value of $x_{(Bj)}$ and Q^2, the dependence on $y = 2ME/Q^2x$ must be included in the integration. Conceptually, the $y_{(Bj)}$-dependence reflects the spacetime structure of the weak interaction vertex, whereas the $x_{(Bj)}$ distribution probes the momentum composition of the target nucleon, so that the two distributions are related to physically completely different meanings.

3.4 Performance of the Method

We now describe the performance of our method in a test using neutrino Monte Carlo data [47] which simulate the BEBC experiment with a hydrogen target at CERN (WA21). Two simulated data samples are considered : the 'full' event sample consists of ~14000 events in the subset of phase space determined by requiring $E_H \geq 7.5\ GeV$ and $W \geq 3\ GeV/c^2$. Since it is far from obvious that the formulae (3.16) and (3.22), involving first and second derivatives of $G(w)$, are useful in the context of limited statistics, we shall comment as well on their applicability to a sample with size of the order of two thousand events (called the 'small' sample). In fact, it is with this level of statistics in mind that the method has been developed initially.

Although cuts in extensive variables like E_H do not *directly* affect the physical region in a (dimensionless) scaling variable, they enter through (again dimensionless) ratios with another extensive variable. In our case, a minimum hadronic energy E_H, for instance, leads to a minimum $y_{(Bj)}$ given by

$$y \geq k_y = (E_H^{min} - M)/E_\nu^{max}. \tag{3.25}$$

This small bound has to be considered, in principle, when we write down an expression for $G(w)$ in terms of an integral over $F(x)$, as in (3.13), in that now the integration interval for $x_{(Bj)}$ is $[w/(1-k_y); 1]$ instead of $[w; 1]$, at fixed w. It can be shown that the structure of the solution does not change due to the implementation of this bound, and in the neutrino case, say, we obtain instead of (3.16)

$$\begin{aligned} F^{(\nu)}(x) &= \frac{1-k_y}{a+1}\Big(v(x)^2 G''(v(x)) - (a-1)v(x)G'(v(x))\Big) && (3.26)\\ v(x) &= x(1-k_y) && (3.27)\end{aligned}$$

Thus, effectively, a cut in E_H stretches the solution by a factor $(1-k_y)^{-1}$, consistent with a maximum w of $w = 1 - k_y$. In practice, the size of k_y is of the order 0.03. Similarly, a cut in the hadronic invariant mass $W \geq W_0$ leads to a bound

$$y \geq k_0 = \frac{W_0^2 - M_P^2}{2ME_{max}(1-x)} \tag{3.28}$$

and to a corresponding solution

$$\begin{aligned} F^{(\nu)}(x) &= \frac{(1-k_0)^{a+1}}{a+1}\,(1 - \frac{k_0}{(1-x)^2}) && (3.29)\\ &\quad \Big(u(x)^{1-a}x^2 G''(x\,u(x)) - (a-1)u(x)^{-a}xG'(x\,u(x))\Big)\,, \\ \text{where} &\quad x\,u(x) = x(1-k_0/(1-x)), \\ \text{for} &\quad x \leq 1 - \sqrt{k_0}. \end{aligned}$$

Again, the effect on the solution is weak, and for the cut values chosen above $k_0 < k_y$, so that the bound in $y_{(Bj)}$ is the relevant one. It should be noted, on the other hand, that a small value of k_0, of the order 0.01, leads to a maximum w value of $w_{max} = (1-\sqrt{k_0})^2 \approx 0.8$ which deviates appreciably from 1. Thus it was usually found that to implement a W_H cut it is sufficient to allow for an upper bound in the form of $G(w)$. To conclude the discussion about the influence of cuts, we have seen that it is possible to implement them in a rigorous way, while their effect on the solutions is small. As long as bounds in E_H, W_H are very small compared to the largest energy scale in the process, ie. $s = 2M_P E$, it is a good approximation to work with the standard formulae (3.16) and (3.22), as has been done in [48]. [4]

Let us now consider first the information about the y distribution. This part of the input to the determination of $F(x)$ can either be supplied from a suitable Monte Carlo simulation or from charged current data, by scaling the known helicity structure with the chiral NC coupling constants and then imposing the cuts above. The important statement is that this information does not impose any a priori assumption concerning the shape of the x distribution. Figures 3.3 and 3.4 show the marginal $H(y)$ as well as the conditional $h(y \mid x)$ for the first three bins [0;0.1),[0.1;0.2),[0.2;0.3) in x for the neutrino and antineutrino case, respectively. These represent the range over which $F(x)$ changes most and which at the same time contains the largest event numbers. The deviations in shape of the fitted $h(y \mid x)$ from the fitted $H(y)$ are small. The mean $y_{(Bj)}$ for fixed x, $< y >_x$, are found to be extremely weakly varying with $x_{(Bj)}$, in particular for the neutrino case, and take the value 0.58 (0.54) for the (anti)neutrino case, as shown in figure 3.5. We obtain parameter values of $a = 4.61 \pm 0.20$ ($a = 2.86 \pm 0.10, b = 2.54 \pm 0.10$; c, which the antineutrino $y_{(Bj)}$ distribution does not constrain, was fixed to 15.0). In

[4] For completeness, we give here the form of the boundaries in the $x - w$ plane for cuts in $\nu = E_H - M, W_H$ and Q^2: as we have seen, $y \geq k_y$ induces $x \geq x_{min} = w/(1-k_y)$. $W \geq W_0$ induces $x_0 = 1 - \sqrt{k_0} \exp r, r \equiv Arcosh(z), z \equiv (1 + k_0 - w)/2\sqrt{k_0}$, and $Q^2 \geq Q_0^2$ induces simply $x \geq w + k_Q$, where $k_Q = Q_0^2/s$. Thus in cases when Q^2 is measureable, the implementation of a Q^2 cut, while being of hyperbolic form $y \geq k_Q/x$ in the $x - y$ plane, is straightforward in the $w - x$ plane.

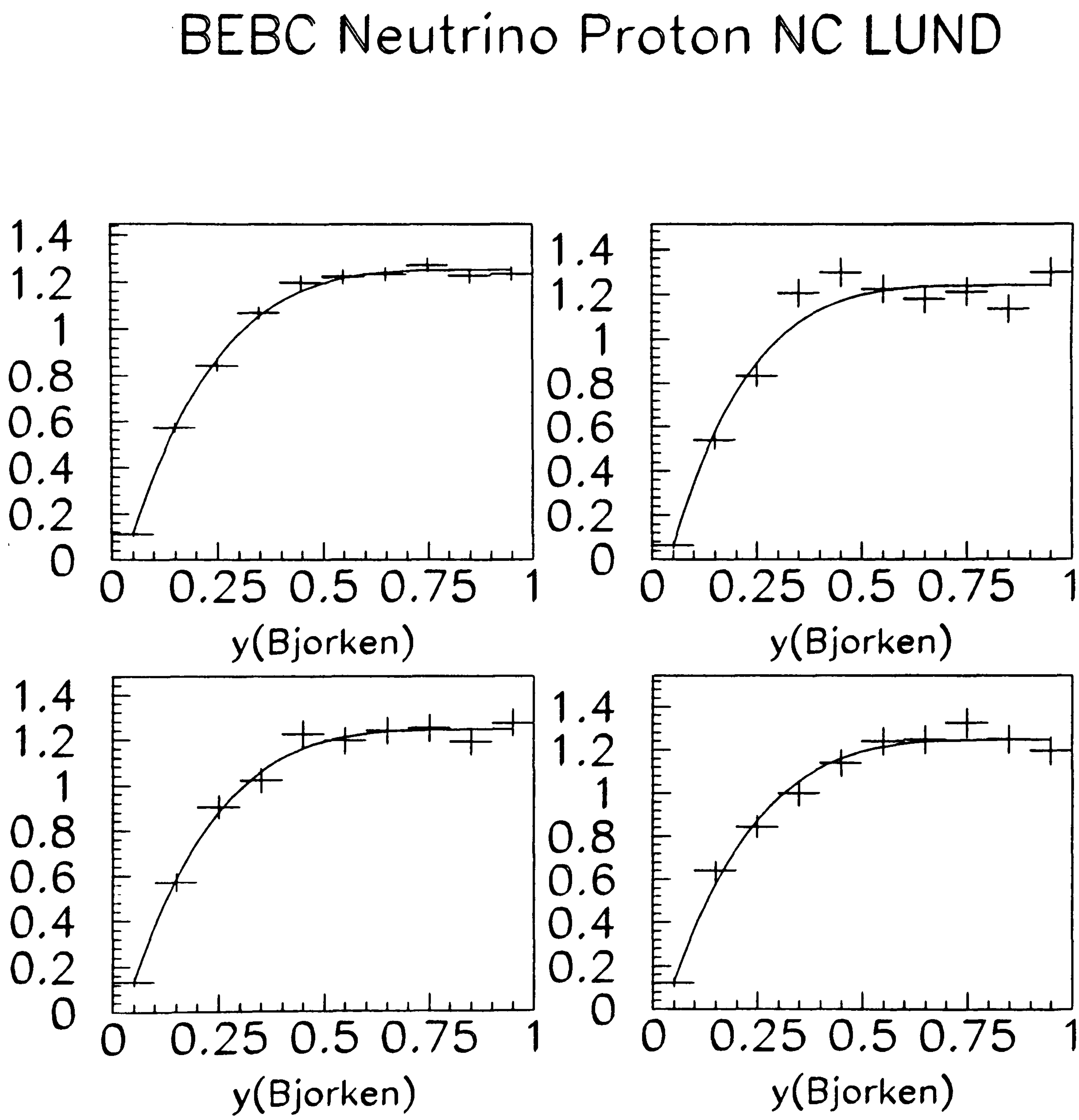

Figure 3.3: *Marginal $y_{(Bj)}$ distribution H(y) (upper left) and conditional $h(y|x)$ (upper right and lower row) for the first three $x_{(Bj)}$ bins of width 0.1, for the neutrino case. Note the slight difference in the vertical scale.*

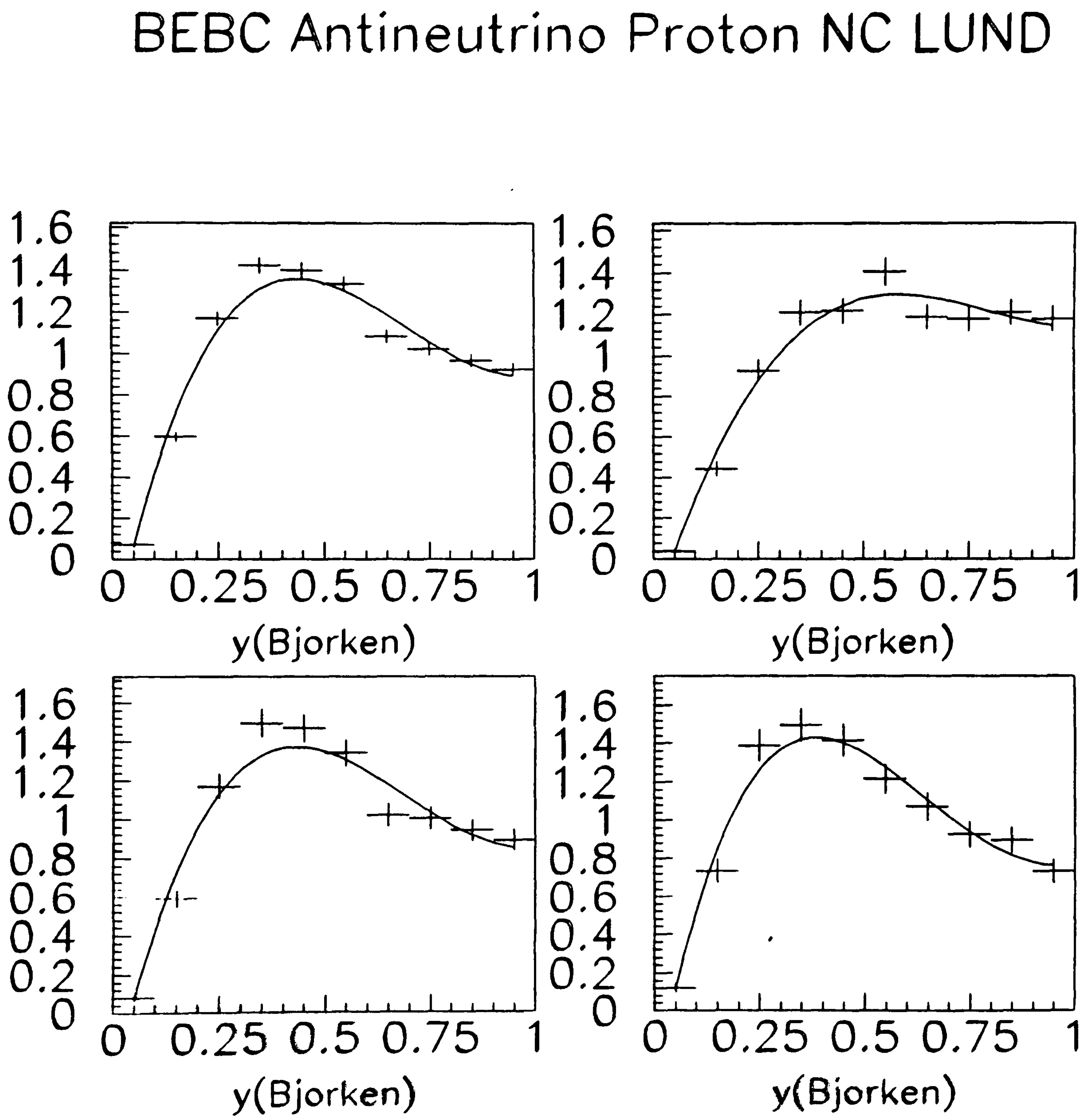

Figure 3.4: *Marginal $y_{(Bj)}$ distribution $H(y)$ (upper left) and conditional $h(y|x)$ (upper right and lower row) for the first three $x_{(Bj)}$ bins of width 0.1, for the antineutrino case. Note the slight difference in the vertical scale.*

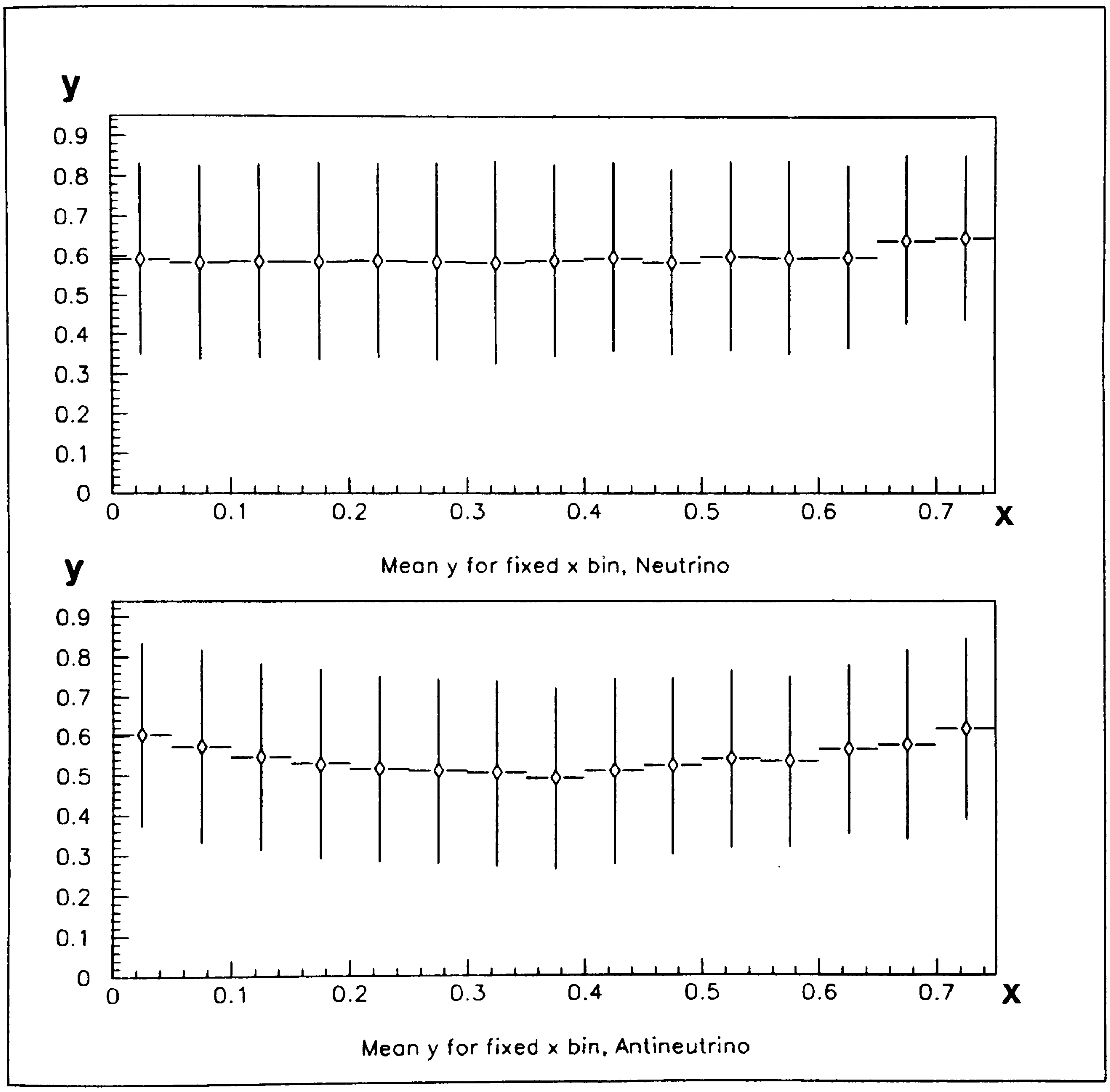

Figure 3.5: *Mean $y_{(Bj)}$ values and spread of the conditional $y_{(Bj)}$ distributions $h(y|x)$ as a function of $x_{(Bj)}$. Note that the error bars are not the the error on the mean, but the standard deviation of the $h(y|x)$.*

view of the fact that the dependence of $F(x)$ on the parameter(s) describing these conditional $y_{(Bj)}$ distributions will turn out to be extremely weak, it can be concluded that the approximation of quasi-independence of the $h(y|x)$ on x is justified within the errors.

Below we shall fit the w distribution to normalised two-parameter functions which subsequently enter the formulae (3.16), (3.22). The motivation for this is that it makes the investigation of stability of $F(x)$ against different input functions that can describe $\frac{1}{N}\frac{dN}{dw}$ lucid. However, we do not intend to advocate any 'model' by choosing one of these functional forms. They are supposed to be mere representations of the fact that the w distributions vary smoothly between the bin centers, the choice of which is quite arbitrary. As a consequence, the individual bin-to-bin statistical errors in w are lost and represented by overall errors in the fit parameters, thus precluding an assignment of point-to-point errors in the result $F(x)$. This limitation is in no way inherent in the principal elements of the method and can be removed since the solution formulae do not make any a priori restriction on $G(w)$. One such possibility is the use of a more sophisticated ansatz for $G(w)$ that employs a partition of unity by *'cubic basis splines'*, choosing the knot distance to be of the order of the experimental resolution in w [44]. However, we convinced ourselves that the description of the observed w distributions using smooth functions of the parametric form below is a convenient *representation* of the data, the detailed functional form of which does not alter the resulting $x_{(Bj)}$ distributions. We shall comment on this further in chapter 6 when discussing systematic errors.

We display the normalised w distribution of the full sample in figure 3.6 in 80 bins of width 0.0075, for $w \leq 0.6$ where sufficient data is available. To test the case of limited statistics, the same was done in parallel for the 'small' sample, using bins of width 0.05. As suggested by figure 3.6, the ensuing 'coarser' w distribution

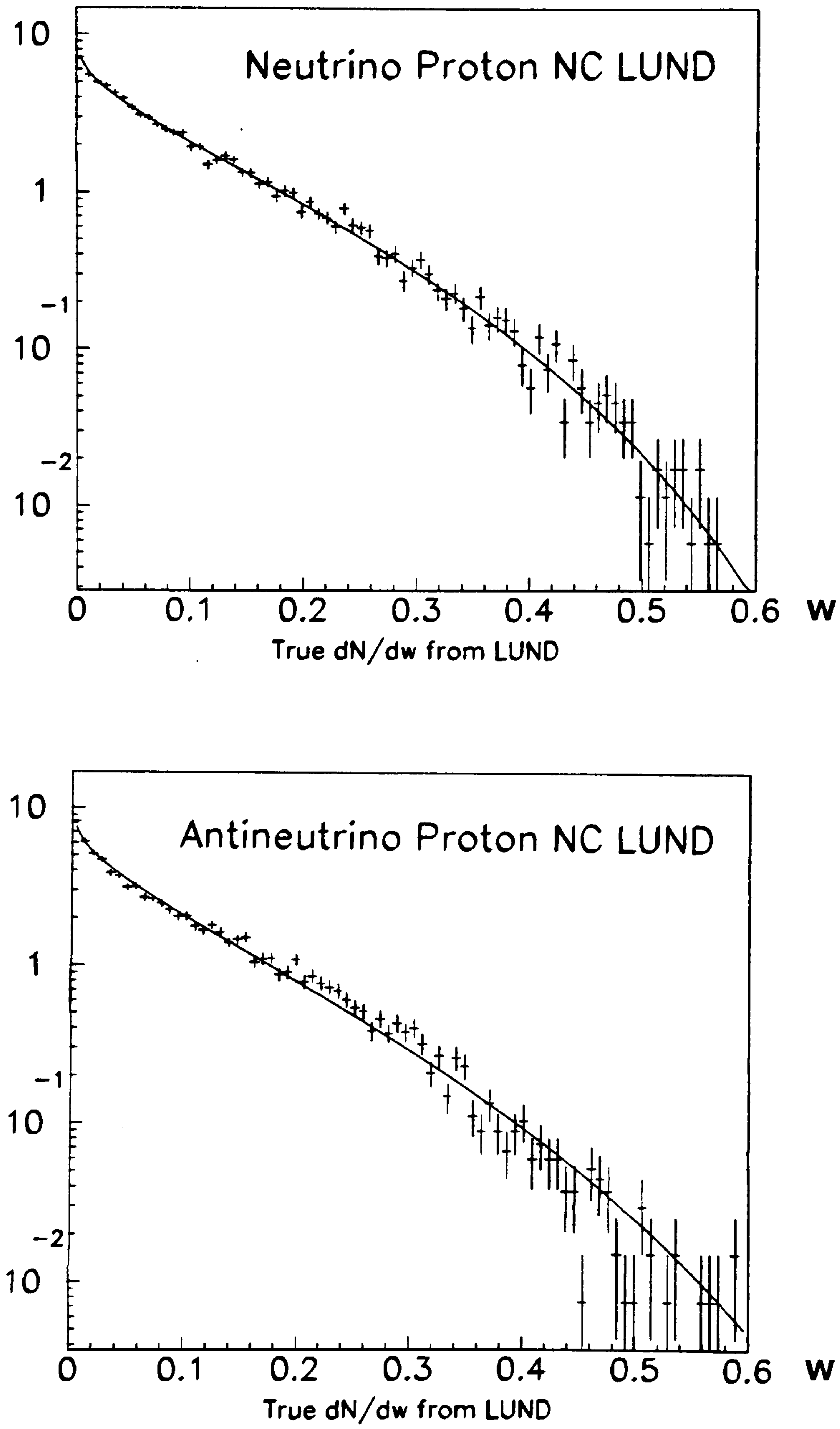

Figure 3.6: *Normalised w distributions $\frac{1}{N}\frac{dN}{dw}$ for the neutrino and antineutrino 'full' sample (see text), respectively.*

is certainly not inconsistent with a pure exponential behaviour, and indeed a fit to a function $G_\alpha \propto \exp(-\alpha w)$ producing a value $\alpha = 10.6 \pm 0.5$ is of reasonable quality. An important point at this preliminary stage is that employing this $G_\alpha(w)$ in the solution for $F(x)$ gives a function which already matches well the true x distribution we are setting out to extract. Except for delivering a slightly soft $F(x)$, which shows as an excess near the maximum of the distribution, the exponential fit to $G(w)$ exhibits all the features of the true x distribution. This shows that it is not due to the use of a more sophisticated function which we shall utilise below, that, for instance, the turnover of F near $x = 0.15$ comes about. It should be emphasised that the main aim in choosing a functional representation of the w distributions is to have a flexible shape that responds well to the trends of the measured dN/dw. Obviously, this can be achieved the better the more parameters are used for the function. It is then a compromise to the limited statistics that we confine ourselves to three quantities describing the w distributions, one each for the behaviour for $w \to 0$ and $w \to w_{max}$, and a normalisation constant.

However, even the small sample w distribution advocates a deviation from a linear shape in a log plot. Thus we found that using either of

$$G_{\lambda,\delta}(w) \propto (w_0 - w)^\lambda / w^\delta \tag{3.30}$$

$$G_{\lambda,\delta}(w) \propto (w_0 - w)^\lambda / (\log 1/w)^\delta \tag{3.31}$$

considerably improves the quality of the fit and allows for faster than exponential fall in G for $w \to 0$ and $w \geq 0.3$. w_0 is the maximum allowed value of w. The value of δ is not determined by the first few w bins only, but follows from the complete shape of $G(w)$ up to about $w = 0.3$. The function (3.31) is the one used in figure 3.6, where we obtained $\lambda \pm \sigma(\lambda) = 3.82 \pm 0.12$, $\delta \pm \sigma(\delta) = 0.78 \pm 0.05$ (neutrino), $\lambda \pm \sigma(\lambda) = 3.63 \pm 0.13$, $\delta \pm \sigma(\delta) = 0.92 \pm 0.05$ (antineutrino), and values of $\chi^2/NDF = 1.26$ for $NDF = 76$ degrees of freedom with the full MC sample. The choice of the function (3.31) displayed here is motivated by the fact that this is the one with which the larger $G(w)$ parameter errors occur, so that the corresponding deviations in the subsequent plots below are the more conservative ones. We shall investigate further the small differences between the solutions $F(x)$ following from (3.31) and (3.30) in chapter 6 when discussing systematic errors.

With this result for $G(w)$, we extract the normalised solution $F(x)$ of the integral equation (3.13), shown as the central lines in figures 3.7 and 3.8, together with those solutions ensuing from using
$G_{\lambda\pm\sigma(\lambda)}$ and $G_{\delta\pm\sigma(\delta)}$ in (3.16) and (3.22),respectively, as dashed and dotted lines. All distributions are normalised to unity in this investigation. The 'true' $x_{(Bj)}$ distribution, taken directly from the Monte Carlo data, is displayed in all figures by the points with error bars. As a consistency test of the method, ideally the solutions should reproduce these shapes, and the figures show that indeed the agreement is remarkable over the entire range of $x_{(Bj)}$. This also indicates that the approximation of independence on $x_{(Bj)}$ of the conditional $h(y|x)$ is a feasible concept, since otherwise the agreement between the solutions $F(x)$ and the true Monte Carlo $x_{(Bj)}$ distributions would have to be attributed to a mere conspiracy. It is noteworthy that the solution is stable in its qualitative features with respect to the exchange of the exponential G_α against $G_{\lambda,\delta}$, although the former is finite at $w = 0$ whereas the latter diverges.

The significance for the small sample is represented by the lowest and highest curve for which $G_{\lambda\pm\Sigma(\lambda)}$ was used where $\Sigma(\lambda) \approx 0.5$ is the error in λ from a fit of 3.31 to the w distribution of the small sample. The harder the w distribution, the harder is $F(x)$ as it must be since x and w are correlated. The extremal curves show that even with limited statistics we can achieve an appreciable precision.

The dependence of F on the parameters λ and δ describing $G(w)$ has to

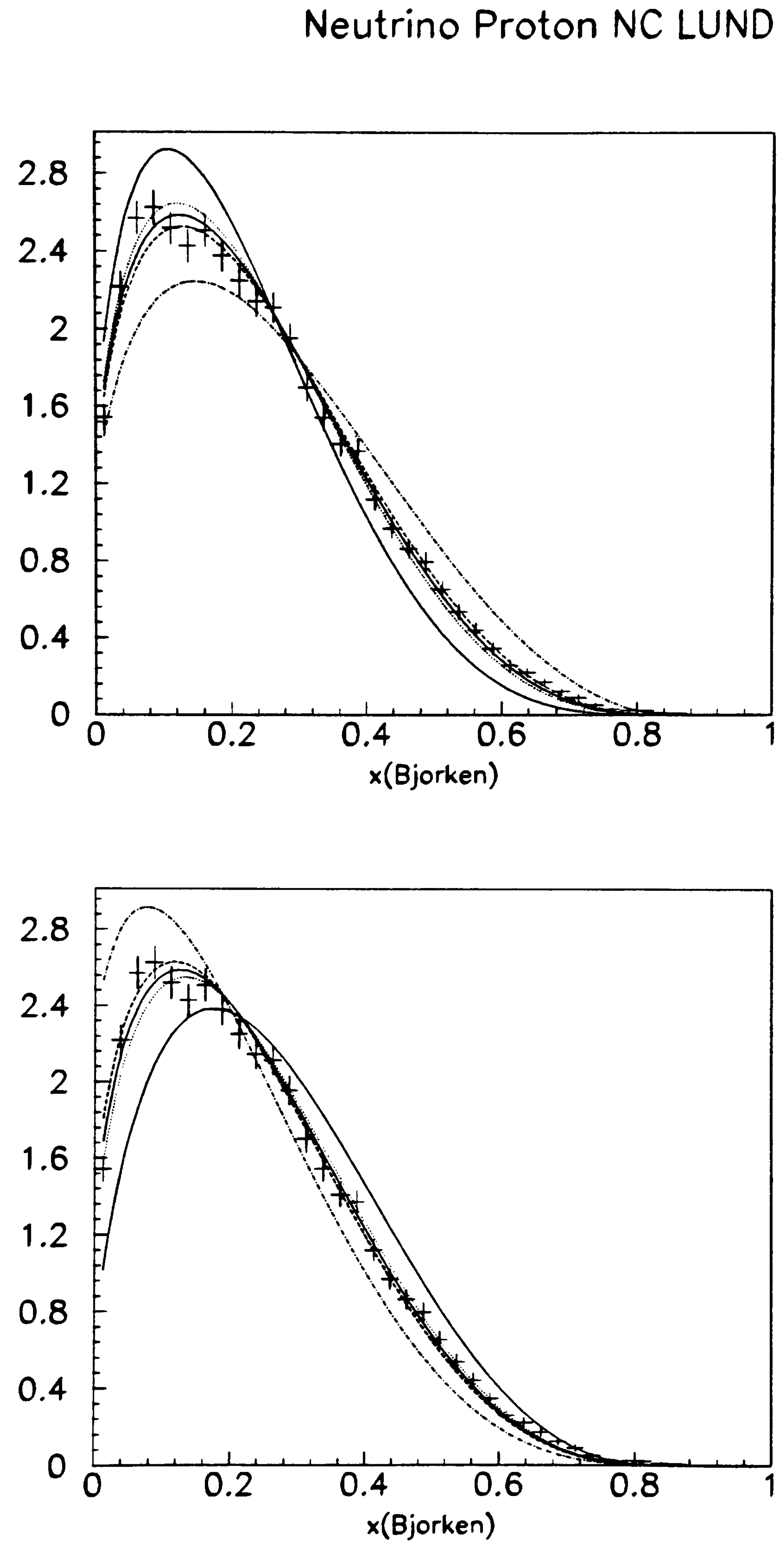

Figure 3.7: *Solution for the $x_{(Bj)}$ distribution $F(x)$ for neutrino proton scattering (central solid line) from the 'full' M.C. sample (see text). Deviations due to parameter errors of the w distributionfrom the 'full' sample (dashed and dotted lines) and from the 'small' sample (outer lines).*

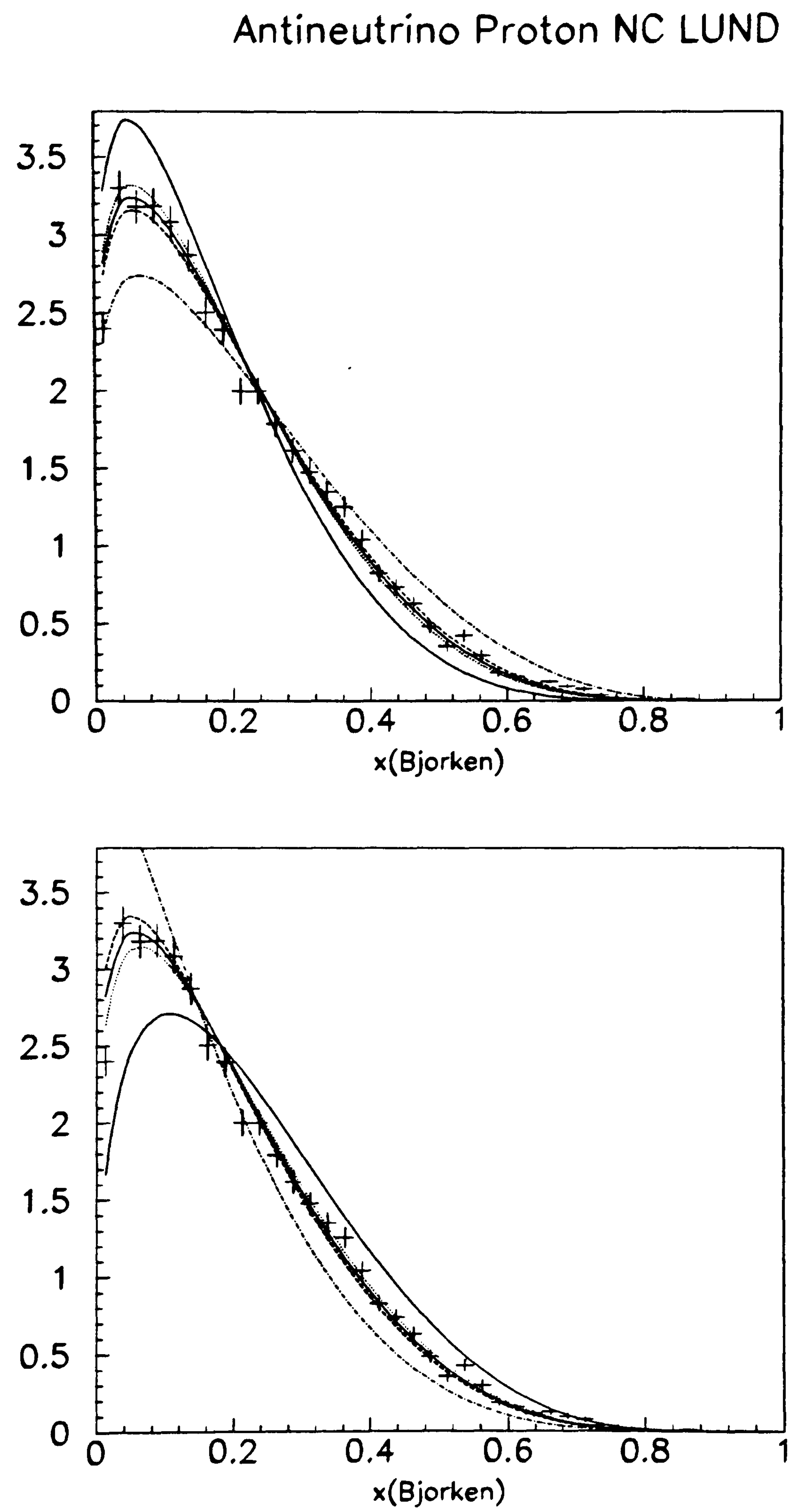

Figure 3.8: *Solution for the $x_{(Bj)}$ distribution F(x) for antineutrino proton scattering (central solid line) from the 'full' M.C. sample (see text). Deviations due to parameter errors of the w distr butionfrom the 'full' sample (dashed and dotted lines) and from the 'small' sample (outer lines).*

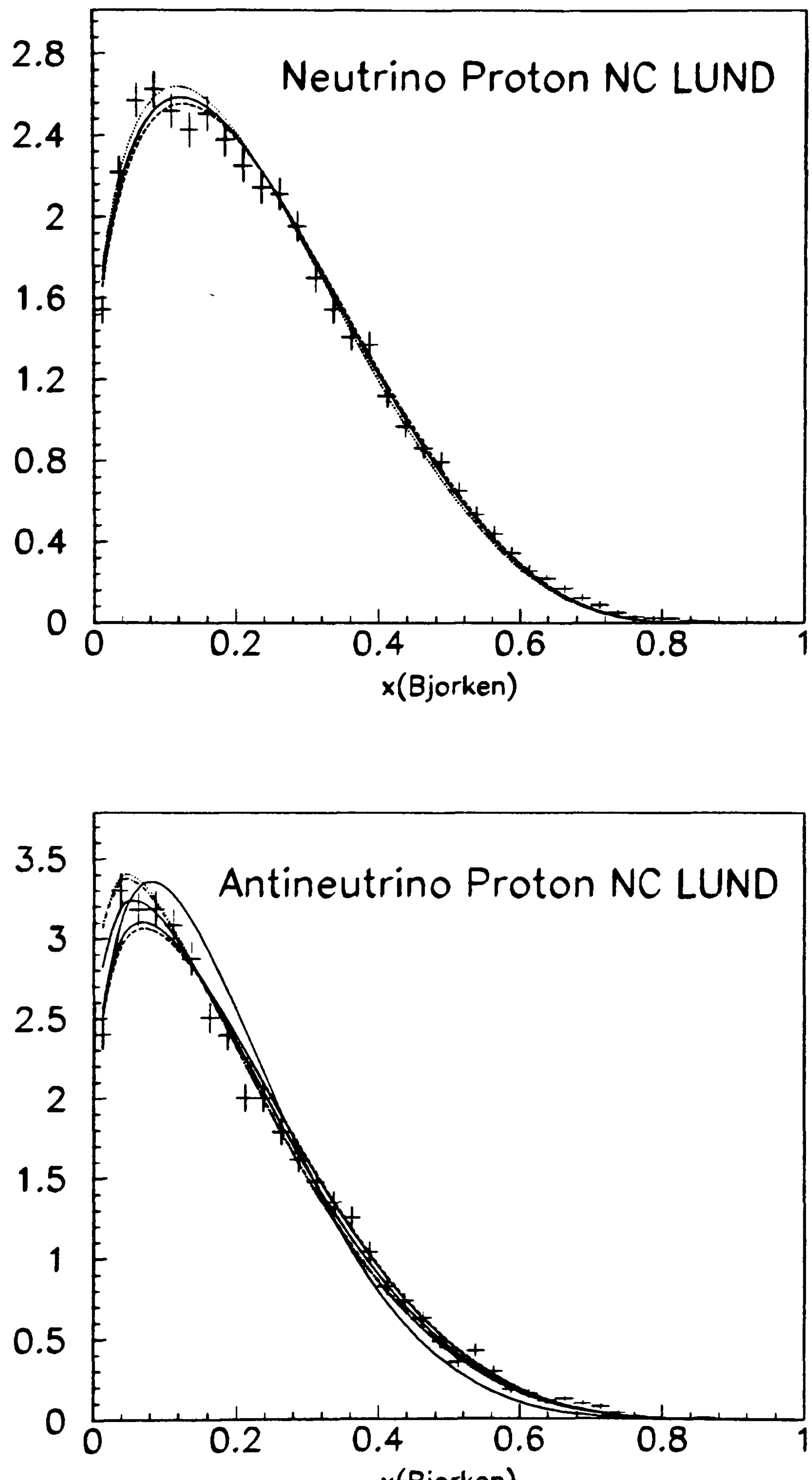

Figure 3.9: *Variation of the (anti)neutrino solution for $F(x)$ with the parameters describing the marginal $y_{(Bj)}$ distribution. In the neutrino case, we show the variation with a, whereas in the antineutrino case with both a and b, and additionally the solution for a hypothetical constant $H(y) \equiv 1$.*

be compared to that on the parameters from the fit of $H(y)$, displayed in figure 3.9 . Next to the previously discussed solution are shown two curves obtained by using $a \pm 2\sigma(a)$, where we added (subtracted) twice the parameter error to make the deviation visible. For the antineutrino case $a \pm \sigma(a)$ and $b \pm \sigma(b)$ as well a hypothetical flat $H(y) \equiv 1$ are shown. We checked the two extremal cases $a = 1$ and $a \to \infty$ of linear and flat $H(y)$, ie. for a situation of rather complete lack of knowledge about a, and obtained solutions deviating from the central one by not more than the deviation encountered with the 'small' sample uncertainty in the parameters of the w distribution, ie. $G_{\lambda \pm \Sigma(\lambda)}$, cf. figure 3. Alternatively, we can say that the dependence of F on a is very small compared to the variation with the input data on w and does not become comparable to the latter unless one is working with event samples of some 10000 events.

3.5 Discussion

Finally, let us review the conditions which have to be met for the method presented to be applicable. The basic assumption is the measurability of the raw distribution in w and a resolution in this variable that is narrow enough to allow a correction for unseen secondaries and for momentum measurement errors. The use of the method in its most powerful and direct way, via an analytic expression like (3.16) which gives $F(x)$ in terms of $G(w)$ and its first two derivatives, further requires the quasi-independence on x of the conditional y distributions for fixed x, a fact associated in part with an independence on x of acceptance losses due to cuts imposed on the data. To conclude, we have shown how to make best use of an appropriately chosen scaling variable w which can be related to x and y. In chapter 5, we are going to show that, in the extreme case of neutrino scattering on liquid hydrogen, it is possible to measure the distribution in w with sufficient accuracy to allow a determination of a uniquely determined x distribution even for quite small data samples. The dependence of the solution on the assumed form of the marginal y distribution was seen to be small, and the extracted x distribution is in agreement with the true one obtained directly from Monte Carlo.

Chapter 4

NC structure functions and w Distributions

4.1 Introduction

In this chapter we study the connection between the neutral current nucleon structure functions and distributions in the hadronic scaling variable $w = p_T^2/(2p_L M_N)$. We are going to show that they are related by simple formulae which do not incorporate any dependence on further kinematical variables, in the scaling approximation. We advocate the use of the w dependence of the neutral current cross section as an important piece of information that can often be extracted more directly from experiment than distributions in Bjorken-x. It also provides access to some quantities that are measured only indirectly in charged current and electromagnetic scattering, and to the behaviour of the structure functions at small values of their argument.

In the investigation of the proton constituents the determination of structure functions has always played a prominent role. These parametrise the composition of the nucleon as it appears to an energetic virtual projectile carrying charge(s) associated with the interaction(s) via which it resolves the substructure. A priori there is nothing to prevent this substructure from emerging differently, depending on which interaction the boson projectile is mediating.

In applying the standard model [15] to these inclusive processes, the structure functions are thought to be convolutions of so-called 'parton distribution functions' (long time scale physics), which describe the probability density to find a scattering source ('parton') inside the hadron, carrying a certain momentum fraction of the latter, and hard partonic cross sections (short time scale physics) determining the scattering of the virtual intermediate boson with the parton ('factorisation') [49].

The hard partonic cross sections are calculable from the gauge theory $SU(3)_c \otimes SU(2)_{t_L} \otimes U(1)_y$ at a given order of the strong coupling, assuming the exchange of a single vector boson. In course of higher order calculations, involving the strong coupling constant of Quantum Chromodynamics (QCD), however, one encounters infrared and mass divergences arising from the Feynman diagrams of physically allowed subprocesses that involve soft and collinear unobserved partons, respectively. These divergences are completely independent of those infinities (arising from self-energy and vertex corrections) taken care of by the usual field renormalisation prescription. It is crucial for the applicability of the parton picture that it could be proven [50] that the concept of factorisation allows an extension leading to a convolution of *finite* factors, which both permit the usual interpretation from above, to all orders in QCD perturbation theory. The main idea is to use the possibility of associating the divergent subprocesses with the propagation of on-shell partons for durations comparable to the long time scale physics which accounts for the binding effects of the hadron. The divergent phenomena are factored out, leaving behind finite calculable partonic cross sections, and are folded with the bare parton distribution functions to yield distributions for observed partons. These are the relevant parton distributions for comparison with experiment and thus argued to be finite. Thus in essence the factorisation idea is a precise (re)definition of what to call an (un)observed parton. It is a remarkable and highly non-trivial result that the 'renormalised' parton distributions are indeed process independent, universal functions, for a *given* given type of interaction (e.g. photoproduction and Drell-Yan process). Without this precondition the more general notion of parton universality, which relates to the structure of the nucleon as revealed via *different* interactions, would be meaningless in the context of a QCD $SU(3)_c$ desciption of the strong interactions.

On the other hand, the parton distribution functions can only be inferred from experiment since they reflect the non-perturbative properties of the nucleon which cannot be calculated analytically from first principles yet. One day lattice QCD might be able to obtain predictions for them. So far, certain average properties like sum rules can be obtained from QCD, and there are expectations about the limiting behaviour at small (large) $x_{(Bj)}$ from various motivations (Regge theory etc). Furthermore, the rate of variation of the structure functions with the square of the four momentum transfer, ie. the logarithmic scaling corrections, are predicted and can be derived from QCD.

The concept of partons induces the hypothesis of a certain universality within the respective parton distributions (and thus within the structure functions) pertaining to the hadronic transition currents of the different interactions. Apart from differing couplings given by the relevant charges, a universal parton composition of the nucleon should emerge. This picture has been demonstrated to be justified for the electromagnetic and weak *charged* current interactions in a wide range of experiments using beams of electrons, muons, hadrons and neutrinos (see, for example, [51]).

For the determination of the weak interaction structure functions the neutrino provides the cleanest probe since it carries weak (isospin) charge only. However, it is intrinsically problematic to obtain *neutral* current (NC) structure functions this way as neither the initial nor the final state lepton is observable. Only with an ideal detector could one achieve the complete reconstruction of the hadronic system leading to a meaningful reconstruction of the relevant scaling variable $x_{(Bj)}$ from the hadronic vertex. Accordingly, the evidence regarding the weak neutral current structure functions is much less stringent and confined to nuclear (heavy) targets, where it has so far proved consistent with charged current data, although with large statistical and systematic uncertainties [57]. In particular, the weak NC structure functions have never been determined for free nucleons, since the methods of their extraction always relied on unfolding methods requiring the use of a narrow band beam, which necessitates a heavy target to ensure a sufficiently large data sample.

We have presented a new method [48] to determine (anti)neutrino neutral current (NC) x_{Bj} distributions by using the variable $w = \frac{p_T^2}{2p_L M_N}$, constructed solely from the hadronic system H of an inclusive NC reaction like $\nu + N \rightarrow \nu + H$, with $p_H = (E_H, p_L, \mathbf{p}_T)$ in the lab frame where the nucleon is at rest. It was shown to be equal to $x_{Bj}(1 - y_{Bj})$ in the Bjorken scaling [53] limit, ie. whenever we can identify $x_{(Bj)}$ with the fraction of the nucleon momentum that is carried by the struck parton. The basic idea then was to concentrate on that part w of $x_{Bj} = w + \frac{p_L - \nu}{M}$ that can be measured sufficiently accurate, and to exploit the fact that we do not have to know $x_{(Bj)}$ for each event individually if we are interested in $\frac{d\sigma}{dx}$ only.

The use of the variable w is advantageous from the point of view of experimental analysis for various other reasons. For instance, discrimination against CC events faking NC events, due to an outgoing lepton having been misidentified as a hadron, is easy since those events cluster at $w = 0$. A small contamination of hadron induced events in a NC sample, almost impossible to supress completely, does not distort the observed w distributions very much. Furthermore, the apparent

Q^2 variation of the distributions in the scaling variables, due to the usual cut in the hadronic energy E_H, is much weaker for $\frac{d\sigma}{dw}|_{Q^2 fix}$ than that of $\frac{d\sigma}{dx}|_{Q^2 fix}$. Finally, the increase of the mean Q^2 with w is far less pronounced than the one with $x_{(Bj)}$, which is known to be highly correlated with Q^2.

The method was completely general insofar as it required no assumption about the form of the NC cross section. Some information about the marginal distribution in $y_{(Bj)}$ was needed, however we found that the influence of the input distribution in $y_{(Bj)}$ on the result $\frac{d\sigma}{dx}$ is weak, pointing to a rather direct dependence of $\frac{d\sigma}{dx}$ on the shape of the w distribution.

The purpose of this chapter is to show that all the information about the weak NC structure functions $F_i^{\nu NC}, i = 1,2,3$ is actually contained in $\frac{d\sigma}{dw}^{\nu NC}$ alone, in the Bjorken scaling limit. Although we have in mind the parton interpretation, augmented by the factorisation idea and the ensuing universality hypothesis, no parton model assumptions are necessary to obtain the results. We only assume the general form of the cross section which follows from Lorentz covariance, the V-A spacetime structure of the leptonic vertex, and time reversal invariance [54]. It will turn out that the special structure of the neutral current, which can be related to its symmetry properties under crossing, is an asset which gives a direct access to quantities that are only indirectly measurable in charged weak and electromagnetic interactions. For instance, we shall find relations between $\int_0^1 dx\ F_3^{\nu NC}$ and the (anti)neutrino NC distributions in w which, in a parton picture, correspond to information about parton distributions that are not weighted by the momentum.

4.2 Crossing symmetry in neutrino nucleon NC interactions

Usually applied to exclusive reactions, crossing symmetry is a concept that relates transition amplitudes $\mathcal{A}$ of different processes, such as $\mathcal{A}_s(a+b \rightarrow c+d)$ and $\mathcal{A}_t(a+\bar{c} \rightarrow \bar{b}+d)$ and $\mathcal{A}_u(\bar{c}+b \rightarrow \bar{a}+d)$ to each other. It is derived from the rather general principles of CPT symmetry and S-matrix analyticity [58]. While second quantisation requires the existence of antiparticles in the framework of Dirac field theory, it is the analyticity postulate which plays that role in S-matrix theory. Conversely, the existence of antiparticles provides some necessity for the postulate, which then entails the possibility to continue the amplitude for a physical channel into a region which corresponds to unphysical kinematical parameters for that channel, but which can be the physical region of a related channel that is the image of the original one under crossing (ie. exchange of an initial and final state particle under reversal of their four-momenta and spin polarisations). Inclusive processes, such as $a+N \rightarrow c+H$, $H =$ hadronic system, can equally well be treated using this concept, as long as the hadronic vertex remains unaffected. This is evident in a parton picture where the inclusive inelastic cross section is composed incoherently of elastic scatterings off the partons, so that the crossing is effectively applied to the elastic exclusive subprocess. The crucial role of the factoristion theorem cannot be overemphasized in this context.

In sharp contrast to charged current neutrinoproduction, weak neutral current inclusive interactions

$$\nu(k_\mu) + N(P_\mu) \ \rightarrow \ \nu(k'_\mu) + H(p_\mu) \tag{4.1}$$

are distinguished by the fact that neutrino and antineutrino scattering are related by crossing symmetry. The definition of all relevant Lorentz invariants can be drawn

νN NC s-channel	$\bar{\nu}$N NC u-channel
$\nu:\ k_\mu$	$k^c_\mu = -k'_\mu$
$\nu':\ k'_\mu$	$k'^c_\mu = -k_\mu$
$Z^0:\ q_\mu$	$q^c_\mu = q_\mu$
$Nucleon:\ P_\mu$	$P^c_\mu = P_\mu$
$Hadrons:\ p_\mu$	$p^c_\mu = p_\mu$
$(k_\mu + P_\mu)^2 \equiv s$	$s^c = u$
$(k_\mu - k'_\mu)^2 \equiv t$	$t^c = t$
$(k_\mu - p_\mu)^2 \equiv u$	$u^c = s$
$\frac{-q^2}{2q\cdot P} \equiv x$	$x^c = x$
$\frac{q\cdot P}{k\cdot P} \equiv y$	$y^c = \frac{-y}{1-y}$
$x(1-y) = w$	$w^c = \frac{x^2}{w}$

Table 4.1: *Transformation of Lorentz vectors and scalars under u-channel crossing.*

from table 4.1, where the 'crossed' parameters are indicated by a superscript 'c'. They correspond to the unphysical region of the antineutrino channel, since $-k^{(\prime)}_\mu$ is a negative energy four-vector (unphysical $E < 0$ particle travelling forwards in time). The u-channel crossed process is

$$\bar{\nu}(k^c_\mu = -k'_\mu) + N(P_\mu) \ \rightarrow\ \bar{\nu}(k'^c_\mu = -k_\mu) + H(p_\mu) \tag{4.2}$$

and is again one which is mediated by the weak interaction only. In the CC case, we would obtain $\mu^+ N \rightarrow \bar{\nu} H$, and not $\bar{\nu} N \rightarrow \mu^+ H$, from the s-channel process $\nu N \rightarrow \mu^- H$. However, this is of marginal value experimentally, since, at the same (low) energy scale, $\mu^+ N$ scattering will rather occur via the electromagnetic interaction, so that $\mu^+ N \rightarrow \bar{\nu} H$ is unmeasurable.

In view of this fact, $w = \frac{p_T^2}{2p_L M}$ turns out to be a natural variable to use, (u-channel) -complementary to $x_{(Bj)}$, as u is complementary to s:

$$w\ s = x\ (-u). \tag{4.3}$$

Nevertheless, x and w do not transform into each other under crossing, as could be hastily assumed from this equation. On the other hand, in terms of an underlying parton elastic scattering, with the corresponding Mandelstam variables in the (anti)neutrino parton center of mass frame denoted by $\hat{s}, \hat{t}, \hat{u}$, one finds

$$x = \hat{s}/s; \quad w = |\hat{u}|/s \tag{4.4}$$

For our investigation, the fundamental quality of the neutral current is the fact that the ν and $\bar{\nu}$ structure functions are necessarily equal:

$$F_i^{\nu NC} = F_i^{\bar{\nu} NC}, \quad i = 1,2,3 \tag{4.5}$$

This follows most directly since the argument of the NC structure functions, $x_{(Bj)}$ and Q^2 (or ν), does not change under u-channel crossing, while, using the form of the dependence of the cross sections on $x_{(Bj)}$ and w given in the next section, one can show explicitly that

$$s \cdot \frac{d^2\sigma^{\nu NC}}{dx\,dw}(s,x,w) \quad = \quad u \cdot \frac{d^2\sigma^{\bar{\nu} NC}}{dx^c dw^c}(u,x,\frac{x^2}{w}) \tag{4.6}$$

are described by one functional expression (as they must be because of the crossing argument), if and only if the scalar functions F_i^{NC} are identical for the neutrino and antineutrino case. [1] Here the right hand side is proportional to the (squared) amplitude for the physical antineutrino ('crossed') NC channel, evaluated at unphysical kinematical values (negative scale u, third argument can be larger than one), where it is found to be equal to the expression for neutrino NC scattering in its physical region (left hand side). The transformation of the kinematical quantities under u-channel crossing can be found in table 4.1 from where one can see that formula (4.6) should have emerged with exactly the given dependence on the crossed parameters $s^c = u, \;\; x^c = x, \;\; w^c = x^2/w$.

[1] We keep with the common practise of writing $d\sigma/dx$ for the name of the cross-section density $x \mapsto \sigma(x)$, although it is nothing like a derivative of a useful x-dependent function. It offers the advantage of distinguishing between the name (e.g. $d\sigma/dx$) of a function and the variables on which it acts (e.g. $\frac{d\sigma}{dx}(\cdot)$), and reminds one of the fact that the function transforms (almost) like a derivative (namely with the *modulus* of the Jacobian), since it is defined via an integral. Like in all crossing applications, the order of the arguments is of course important. In our case, the first argument is the dimensionful scale, whereas the second and third are the dimensionless scaling variables, the fiist of which is the canonical argument of the structure functions .

The reason for the Mandelstam factors s, u in (6) is that we have to consider (squared) amplitudes rather than cross sections when applying crossing symmetry. Since $2 \rightarrow 2$ phase space is dimensionless [59], and the flux factor contributes $1/s$ to the cross section, $s^{(c)} \cdot \sigma$ is the squared amplitude up to numerical factors.

The argument given is sufficient to conclude the equality of the neutrino and antineutrino NC structure functions , but is obviously a stronger condition than the hermiticity of the weak neutral hadronic current, from which the same equality follows (only by assuming an isoscalar target and a vanishing Cabibbo angle is it possible to construct a hermitian *charged* weak current so that a similar equality results for the neutrino and antineutrino CC structure functions). However, using the concept of crossing in our case reflects directly the physical basis of the equality, namely the fact that the outgoing neutrino is actually identical with the incoming lepton and that it has the same helicity. Were this not so, we would not obtain the desired right-handed antineutrino in-field by crossing the left-handed neutrino out-field, and no statement could be made. To see how the hermiticity of the hadronic weak neutral current J_H^μ follows from crossing symmetry, or, equivalently, from the identity of the incoming and outgoing (anti)neutrino, we only have to note that the latter entails the hermiticity of the leptonic current J_ℓ^μ, so that $J_H^\mu = J_H^{\dagger\mu}$ because the interaction must be hermitian, and is assumed to be of the current-current form $g_{\mu\nu} J_\ell^\mu J_H^\nu$ (for this argument we can work with a scalar prodcuct of currents that uses the metric, since one can choose gauge in which the Z^0 propagator is proportional to the metric).

Considering deep inelastic scattering in the crossing context, one is led to a convenient representation of the physical region. Since there are only three independent kinematical variables in unpolarised deep inelastic scattering, we can easily visualise the interdependence of different choices of any pair of variables. The pro-

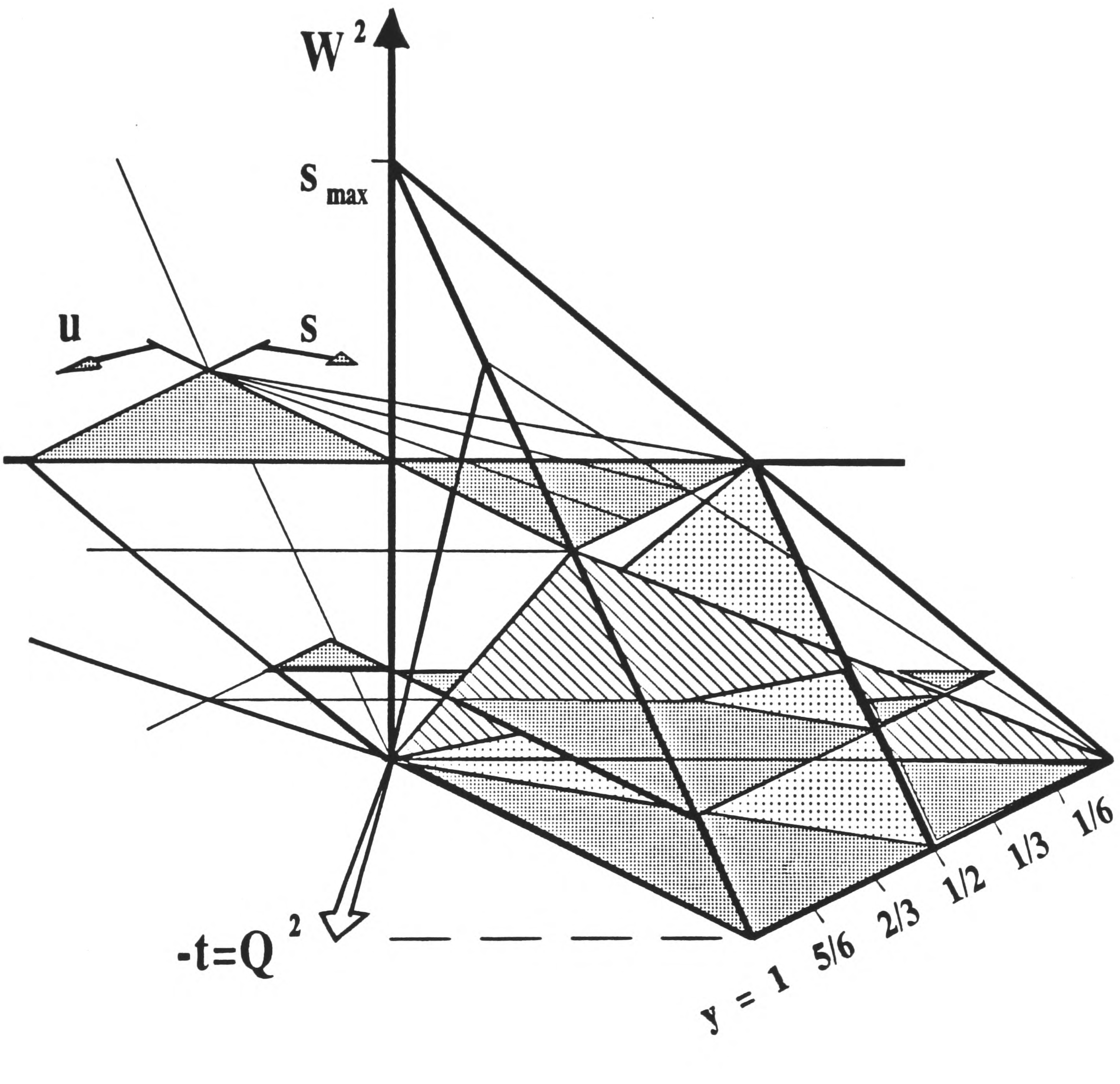

Figure 4.1: *Figure 1: Representation of the physical region in deep inelastic scattering.*

cedure is as follows: for fixed hadronic invariant mass, $W_H = p^\mu p_\mu$, we can take the usual 2-dimensional plot in the Mandelstam variables s, t, u which uses trigonal coordinates. Then the physical region is itself an equilateral triangle, of height $s_{max} - W_H^2$, given by $t = -Q^2 < 0, W_H^2 < s < s_{max}$, and $-u > 0$, (see figure 4.1). Here the lines $y = cst$ are rays from the point $u = s = 0$ into the physical region, with $W_H^2/s < y < 1$, whereas $x = cst$ corresponds to parallels to $t = 0$. We identify the point $(s, u) = (W_H^2, 0)$ as the origin for the chosen W_H^2. If we now arrange all such 'horizontal' planes to be aligned vertically so that their origins define the vertical axis, one arrives at a trigonal pyramid as physical region with the base given by $x = 1$, two vertical faces by $Q^2 = x = 0$, and $y = 1$, respectively, and third face by $s = s_{max}$. With this choice all surfaces $x = cst$ and $y = cst$ are planes, where the former intersect the vertical plane $Q^2 = 0$ at an angle α_x given by $x = (1 + cot\ \alpha_x)^{-1}$. The surfaces $w = w_0$ are then half-cones with top at $Q^2 = W^2 = u = 0$ and confined by the planes $x = w_0$ and $1 - y = w_0$, which they intersect at the base $x = 1$. Three horizontal planes are shown, for the choices $W^2 = s_{max}/2$, $W^2 = s_{max}/6$, and $W^2 = W_{min}^2 = M_N^2 \approx 0$, as well as two planes for constant $x_{(Bj)} = 0.5$ (line-hatched), and $y_{(Bj)} = 0.5$ (dot-hatched). The values of s, u are to be taken as horizontal distances perpendicular to the axes $s = 0, u = 0$, respectively.

With this construction the constraining effect on any pair of quantities of fixing a third independent variable is immediately clear, since we always have $s \leq s_{max}$. For instance, a cut in Q^2 removes a slice parallel to the 'back' face $Q^2 = 0$ and leads to a minimum x value (for $y = 1$), and as well a minimum y value (for $x = 1$), both Q_{cut}^2/s_{max}. In the scaling limit, it is sufficient to visualise the distribution in $x_{(Bj)}$ and $y_{(Bj)}$ on the front $s = s_{max}$, where the equi-$y_{(Bj)}$ lines are parallels to $y = 1$, and the equi-$x_{(Bj)}$ lines are rays emanating from $Q^2 = W^2 = 0$ (three of which, for the values $x = 1/4,\ 1/2,\ 3/4$, are shown). Then a Q^2-cut, for instance, takes the form of a straight line that affects all $y_{(Bj)}$ at low $x_{(Bj)}$ and only low $y_{(Bj)}$ at large $x_{(Bj)}$. Other interdependences are similarly intuitive by inspection of the plot.

4.3 The w-dependence of the NC cross section

We shall aim at applying one principal idea to our problem: since the object of interest is not so much the values of a scaling variable but rather those of the (structure) *functions* F_i, it is not necessary to have them act on $x_{(Bj)}$, the variable which gives them their physical interpretation. If we can establish a relation between *functions*, like $F_i(\cdot) = G_i\{f_j(\cdot)\}$, knowing the G_i from rather general assumptions and measuring the f_j will tell us all about the F_i, no matter whether we use $x_{(Bj)}$ as an argument or not. We start by expressing the ν (and $\overline{\nu}$) NC cross section as a function of x, w:

$$\frac{d^2\sigma^{NC}}{dw dx} = \frac{G^2 s}{2\pi}\,\frac{1}{x}\,\{\frac{1}{2}(1-\frac{w}{x})^2\, 2x\mathcal{F}_1^{NC}(x) \quad + (\frac{w}{x}(1+\epsilon)-\epsilon)\,\mathcal{F}_2^{NC}(x) \quad \pm\frac{1}{2}(1-\frac{w^2}{x^2})\,x\mathcal{F}_3^{NC}(x)\} \tag{4.7}$$

where we did not write out the dependence of the structure functions on $Q^2 = -q^2 = -t$, and we denote $\epsilon = \frac{xM}{2E_\nu}$. The lower sign always applies to the antineutrino case. We are interested in the kinematic region where the Z^0 boson propagator effects, contributing a factor $[M_Z^2/(-Q^2 - M_Z^2)]^2$ to (4.7) in general, are negligible. Note that a factor of x^{-1} appeared as a consequence of the Jacobian, so that we are dealing with expressions proportional to $x\mathcal{F}_{1,3}(x)/x$. Introducing

$$\eta(x, Q^2) = \frac{1 + R(x, Q^2)}{1 + (2Mx/Q)^2} \ ,$$

where $R = \sigma_L/\sigma_T$, so that $\mathcal{F}_2 = 2x \cdot \eta\mathcal{F}_1$, and omitting [2] the target mass term $y\epsilon$, we obtain

$$\frac{4\pi}{G^2 s}\frac{d^2\sigma^{NC}}{dw dx} = \{1 + 2(\eta(x)-1)\frac{w}{x} + (\frac{w}{x})^2\}\, 2\mathcal{F}_1^{NC}(x) \ \pm\ (1-(\frac{w}{x})^2)\,\mathcal{F}_3^{NC}(x) \tag{4.8}$$

[2]The omission of the small target mass term in the equivalent *charged* current case is consistent with neglecting the structure functions W_4, W_5 [54] that are suppressed relative to W_2, W_3 by a factor $m_\mu m_q/Q^2$ proportional to the muon and the quark mass and thus non-vanishing for nonzero quark masses (chiral symmetry breaking). The target mass term $y\epsilon = xyM/2E = (xM)^2y^2/Q^2$ is comparable to this factor bearing in mind that xM can be considered an effective constituent mass. Although the lepton mass is zero for the NC case, one could argue that it should be analysed making the analogous assumptions as in the CC case.

Here we chose to keep $\mathcal{F}_1$ and $\mathcal{F}_3$ since these have the same powers of x in the usual definition where only $\mathcal{F}_2$ is proportional to x times the parton distributions. The factor 2 in front of $\mathcal{F}_1$ is entirely due to this historical convention for defining the structure functions. In the following, we adopt a convenient notation that treats the three structure functions on a more democratical footing . It is motivated, for instance, in [52], and we shall find that our results look more symmetrical using:

$$F_1^{(NC)} \equiv 2\mathcal{F}_1^{NC}$$
$$F_2^{(NC)} \equiv \mathcal{F}_2^{NC}/x$$
$$F_3^{(NC)} \equiv \mathcal{F}_3^{NC}$$

Then $F_1 = F_L + F_R$ is the transverse amplitude, and $F_3 = F_L - F_R$ represents the parity-violating amplitude.

We now make the approximation that the NC structure functions scale, thereby neglecting logarithmic corrections in Q^2/Λ^2_{QCD}. Note that while retaining η, we should have to assume $(2Mx/Q)^2 = (Q^2/\nu^2) = 2Mx/\nu \ll 1$ so that $\eta = 1+R(x)$. This is reasonable in the Bjorken limit $\nu \rightarrow \infty, Q^2 \rightarrow \infty, Q^2/\nu$ finite.

The helicity structure of the weak interaction, giving rise to terms up to order w^2 only, then allows the following procedure: we integrate over all possible $x_{(Bj)}$ values for fixed w to obtain the w distribution:

$$\frac{4\pi}{G^2 s}\frac{d\sigma^{NC}}{dw} = \int_w^1 dx(F_1 \pm F_3) + w^2 \int_w^1 dx \frac{F_1 \mp F_3}{x^2} + 2w \int_w^1 dx(\eta - 1)\frac{F_1}{x} \tag{4.9}$$

where we supressed the dependence of the F_i and η on $x_{(Bj)}$ for brevity. Thus the even powers of w are proportional to $F_{L,R}$, while the linear term in w is proportional to the transverse amplitude. Taking the derivative of this w distribution $\sigma(w) \equiv \frac{d\sigma}{dw}$ then isolates the F_1 part of the integrands:

$$-\frac{2\pi}{G^2 s}\frac{d^2\sigma^{NC}}{dw^2}(w) = F_1(w) - w\int_w^1 dx \frac{F_1 \mp F_3}{x^2} - \frac{d}{dw}\{w\int_w^1 dx(\eta - 1)\frac{F_1}{x}\}. \tag{4.10}$$

Here it is seen how a *functional* connection between the w distributions and $F_{1,3}$ emerges for the first time. This holds separately for neutrino and antineutrino and is valid so far for the charged current case as well. For neutral currents, however, we can profit from the precious property $F_i^{\nu NC} = F_i^{\bar{\nu} NC}$ and take linear combinations to separate the dependence on F_1 and F_3 (omitting the superscript 'NC' on the σ's):

$$-\frac{1}{2}\frac{2\pi}{G^2 s}\left(\frac{d^2\sigma^\nu}{dw^2} - \frac{d^2\sigma^{\bar{\nu}}}{dw^2}\right) = w\int_w^1 dx \frac{F_3(x)}{x^2} \tag{4.11}$$

$$-\frac{1}{2}\frac{2\pi}{G^2 s}\left(\frac{d^2\sigma^\nu}{dw^2} + \frac{d^2\sigma^{\bar{\nu}}}{dw^2}\right) = F_1(w) - w\int_w^1 dx \frac{F_1}{x^2} - \frac{d}{dw}\{w\int_w^1 dx(\eta - 1)\frac{F_1}{x}\} \tag{4.12}$$

where the expression for the difference is independent of $\eta(x)$, as expected. The integrals are definite and hence finite, so all terms are finite for $w > 0$. We find a vanishing (finite) cross section derivative difference for $w \to 0$ only if F_3 is zero (finite) at the origin. [3] This is of course the expected behaviour of F_3, if it behaved as its charged current and electromagnetic relative. It is interesting to recall that for a quark-antiquark symmetric sea which dominates the low $x_{(Bj)}$ region (which, in turn, is contained in the small w region, e.g. $x < 0.05$ implies $w < 0.05$), the ν and $\bar{\nu}$ cross sections are identical, so that (4.11) would reflect a consistent picture in a parton framework. On the other hand, F_1 is expected to diverge and would lead to a cross section sum with singular derivative, at the origin. To keep the notation concise, we define the scaled sum and difference of the w distributions:

$$\Gamma_\pm(w) \equiv \frac{2\pi}{G^2 s}\left(\frac{d\sigma^\nu}{dw} \pm \frac{d\sigma^{\bar{\nu}}}{dw}\right)(w) \tag{4.13}$$

These functions are eventually measured, and normalised to $\sigma^\nu(E_\nu)/E_\nu$ which is constant in the scaling limit. The equation 4.11) for F_3 can be solved by simple differentiation, and one obtains

$$F_3(w) = \frac{1}{2}(w\Gamma''_-(w) - \Gamma'_-(w)) \tag{4.14}$$

[3] Recall that $\lim_{w\to 0}\int_w^1 dx\ (w/x^t)$ exists for all $t \leq 2$

where the primes indicate derivatives w.r.t. the argument, here w. The case of F_1 is slightly more complicated since (4.12) is a nontrivial integral equation. However, it can still be solved analytically. This is obvious for $\eta = 1$ and leads to

$$F_1'(w) = \frac{1}{2}(-\Gamma_+''(w) + \frac{1}{w}\Gamma_+'(w)) \tag{4.15}$$

$$\text{or} \quad F_1(w) = -\frac{1}{2}(\Gamma_+'(w) + \int_w^1 dv \frac{\Gamma_+'(v)}{v}) \tag{4.16}$$

The derivation for F_1 does not work as simply if we do not assume the validity of the Callan-Gross relation. In that case, it is possible to convert the integral equation (4.12) into a linear differential equation for products of η and F_1:

$$(\eta F_1)'' + \frac{1}{w}(\eta F_1)' - \frac{1}{w^2}(\eta - 1)F_1 = -\frac{1}{2}\Gamma_+''' \tag{4.17}$$

where F_1, η, Γ are functions of w. If we make the approximation of neglecting the term $\eta - 1$ relative to the ones in η, we obtain

$$F_2(w) = (\eta F_1)(w) = -\frac{1}{2}(\Gamma_+'(w) + \int_w^1 dv \frac{\Gamma_+'(v)}{v}), \tag{4.18}$$

which gives back (4.16) in the limit $\eta \to 1$, as required. For an inverse power law behaviour of F_1 as its argument approaches zero, $F_1'', F_1'/x$ and F_1/x^2 will be of the same order of magnitude (modulo the exponent). The approximation is thus applicable for any R that is small, and bounded near the origin [4] (in the most general case (4.12) can be integrated numerically).

The solutions obtained for $F_{1,3}$ are uniquely determined after choosing the first two derivatives of $F_{1,3}$ and $\Gamma_\pm$ and these functions themselves to vanish at $x = 1$. The expected shape near $x = 1$ of the structure functions , $(1-x)^\alpha$, with $\alpha > 2$ for the slowest falling part, fulfils this condition. We note that a dominating power law behaviour of $\Gamma_\pm$ near the origin induces a related one for F_3 and ηF_1, as visible from eqs (4.14) and (4.18): $\Gamma_\pm \sim w^{g^\pm}$ translates into $F_{1,3} \sim x^{f_{1,3}}$, *not* into

[4]Often assumed is an interpolating behaviour motivated from QCD arguments: $R = (1 - x)/(4\frac{1}{8} - N_f/4)\ln(Q^2/\Lambda^2)$, where N_f is the relevant number of flavours at Q^2 [55]

several power terms, and $f_{1,3} = g^{\pm} + 1$, where $f_1, g^+ < 0$. Thus the investigation of the behaviour of the w distributions near the origin can give the exponents of the structure functions for $x \rightarrow 0$ directly, if one makes the assumption that they are described by a power law.

Finally, due to the fact that the integral equations (4.11,4.12) are linear in the $F_{1,3}$, the solutions (4.14,4.18) are obviously additive, a property which is of course desireable when thinking of a decomposition of the structure functions into sea and valence contributions in the parton model, or in general into flavour singlet and non-singlet parts.

4.4 Discussion

We have shown that it is advantageous to express NC cross sections in terms of the hadronic scaling variable w and we found a direct connection between the NC structure functions and the w distributions in the scaling limit. Two main ingredients on which the calculation was based were the equality of νNC and $\bar{\nu}$NC structure functions, and the analytical consequences of the weak neutral current helicity structure.

One feature worth noting is that the w distributions are related to the F_i themselves rather than $x \cdot F_i$. This becomes more obvious if we calculate the integral over $F_{1,3}$, for which (4.14) and (4.18) lead to

$$\int_0^1 dx F_3(x) = \Gamma_-(0) \tag{4.19}$$

$$\int_{x_0}^1 dx\ \eta(x) F_1(x) = \Gamma_+(x_0) + \frac{1}{2}\int_{x_0}^1 dx\ \frac{x_0}{x}\Gamma'_+(x) \tag{4.20}$$

In a parton framework the first of these equations gives us the possibility to extract information about the zeroth moment of the valence quark distribution, whereas the second one displays the diverging singlet part of the hadron.

The experimental determination of the derivatives of the w distributions does not pose as difficult a problem as it may appear at first sight. The $\frac{d\sigma^{NC}}{dw}$ fall so rapidly that a point to point calculation of the derivatives, using one of the various discretised numerical approximations [56], can be performed, since the granularity of the binning is limited by the magnitude of the experimental resolution. Furthermore, the shape of w distributions can be parametrised in a simple way by terms of the form

$$c(1-w)^a / w^{1/b} \tag{4.21}$$

so that the use of a fit, from which the derivatives are simple to deduce, represents a second possibility to apply the above formulae.

At the outset of this work, the shape of the (anti)neutrino NC proton w distribution was found [48][37] to be surprisingly reminiscent of that of $F_1 = 2\mathcal{F}_1$, where both are conveniently displayed on a logarithmic scale. It does not differ in its qualitative aspects between neutrino and antineutrino NC events, so that Γ_+ is representative for both cases. Since $\ln|f'| = \ln f + \ln|(\ln f)'|$ for any positive function f with monotonic $\ln f$, the shape of Γ_+ is preserved in taking its derivative, if it is parametised by (4.21). Thus equation (4.18) provides an explanation for the similarity observed between F_1 and the (anti)neutrino NC w distribution (sum).

Certainly it has to be kept in mind that the assumption of scaling played a crucial role in our argument. It leaves us with a cross section that is proportional to the center of mass energy and a function that depends on two *dimensionless* variables only. The fact that they are dimensionless permits us to combine them into any new pair of variables, and we showed that the combination $x, w = x(1-y)$ is useful for our aims.

Extracting the structure functions by looking at distributions in a different variable than their canonical one, $x_{(Bj)}$, entails the possibility [60] to learn about their behaviour in the region of values assumed by w, due to the direct functional (i.e. pointwise) dependence revealed by eqs. (4.14) and (4.18). This region can be different from the region of accessible $x_{(Bj)}$ values. Indeed, the w distributions can be measured down to much smaller values than the $x_{(Bj)}$ distributions, as long as the detector has a good angular resolution for the momentum of the hadronic system as a whole. This statement remains valid even in the presence of kinematical cuts. Usually, the minimum meaningful $x_{(Bj)}$ is determined by the necessity of imposing a Q^2 cut, to ensure that one is investigating the region of approximate scaling, outside which $x_{(Bj)}$ does not have the desired interpretation (we expanded on this in [48]). This confines $x_{(Bj)}$ to $x > Q^2_{cut}/s$. On the other hand, it is easy to convince oneself that neither a Q^2-cut, nor one in $\nu^{lab} = E_{Had} - M$ or $W^2_{Had} = g_{\mu\nu}p^{\mu}_{Had}p^{\nu}_{Had}$ leads to a lower bound in w induced from the one in $x_{(Bj)}$. This is also expected from the definition of w, since the region $w_0 < w < w_0 + \Delta w$ receives contributions from all $x > w_0$. [5]

In the context of analysing the limiting behaviour of the structure functions near the origin, it can be instructive to look at the distributions in $\ell = \log w < 0$, if the resolution in this quantity is sufficiently good. For a shape of Γ_+ represented by only one term of the form (4.21) near the origin, the logarithm of the ℓ distribution (sum) would be expected to behave like

$$cst + (1 - \frac{1}{b}) \cdot \ell$$

at small $w = e^{\ell}$, so that $g^+ = -1/b$ could be extracted. For such an investigation it is advantageous that the mean Q^2 for a fixed value of w, $< Q^2 >_w$, is only decreasing slowly with $\ln w$ and is, in particular, not vanishing in the lowest accessible $\ln w$ bin. This is quite unlike the case of extracting $x_{(Bj)}$, where $x_{(Bj)} \to 0$ is always correlated with $Q^2 \to 0$, so that the statistics for the small $x_{(Bj)}$, finite Q^2 region must become small.

The reason why our argument can lead to a determination of the structure functions , including in an $x_{(Bj)}$ region which is not directly accessible, lies with the fact that we exploited the known spacetime structure (ie. $y_{(Bj)}$ dependence) of the cross-section, which fixes $\sigma(x, w(x,y))$ for $y_{(Bj)}$ -independent structure functions . Of course an obtained w-distribution would have to be corrected for cuts prior to the application of the above considerations. Thus the relevant point is that the cross section remains finite at small w and falls sufficiently slow with $\ln w$.

We conclude that the special structure of the neutrino NC cross sections

[5] Recall that the lines w=cst are hyperbolae in the $x_{(Bj)}$ - $y_{(Bj)}$ plane, as are the lines $y = y_c(Q^2_{cut}, s_{max}, x) \equiv Q^2_{cut}/(s_{max}x)$ and $y = y^c(W^2_{cut}, s_{max}, x) \equiv W^2_{cut}/s_{max}(1-x)$ with $s = 2M_N E_{beam}$.

leads to a direct connection between the $x_{(Bj)}$ and w distributions that justifies the investigation of the w dependence of the cross section in its own right.

Chapter 5

Determination of the w Distributions

5.1 Introduction

Experimentally the detection of neutrino neutral current events is more complicated than the one of charged current events since the outgoing lepton remains unobserved. Since there are other processes which have an identical signature to the genuine NC topology, the discrimination against those is of prime importance when one aims at investigating NC scattering of neutrinos. Thus the Internal Picket Fence has been designed and used in conjunction with the bubble chamber and enables us to reliably estimate the backgrounds to the NC sample. Its operation proved successful and has provoked the construction of similar components for other hybrid detectors using a bubble chamber as tracking device, for instance the 15' bubble chamber at Fermilab.

On the basis of the method presented in chapter 3, we are going to motivate the kinematical region we are using for the reconstruction of the w distributions and we shall find that the measured raw w distributions can be corrected for resolution effects and losses of neutral hadrons. Prior to the considerations of resolution effects, all corrections to the NC sample will have been obtained in dependence on w.

5.2 Event Classification with BEBC-IPF-EMI

5.2.1 Problems in Identifying Neutrino-induced Muonless Events

In this section we shall demonstrate the use of the BEBC-IPF-EMI hybrid detector for the definition of a Neutral Current event sample. Since the classification of an event as being of charged current (CC) type is a requirement on the quality of the muon identification, which will not be satisfied by all genuine CC events, one main contamination of the NC sample will arise from the kinematic region for CC events where muons are likely to be lost, as well as from all (geometrical or electronic) inefficiencies of the detector system itself.

The other main problem is a stringent suppression of hadron induced events. This has been a great challenge for experiment historically since long before the first observation of neutral currents in 1973 [63]. Neutral hadrons (e.g. neutrons, K_L^0, Λ) are produced through interactions of neutrinos in the material upstream of BEBC and are partially discriminated against by the help of the veto EMI plane (see figure 2.2 in chapter 3). However, between this plane and the chamber liquid we find ample material from the shielding and the magnet coils, as well as the steel wall of BEBC itself, in which neutrino induced CC interactions can give rise to neutral secondaries which enter the bubble chamber and can fake a NC event. Together with the neutral secondary, other charged particles from the same vertex in the material will tend to be more or less aligned with the neutral and thus often penetrate into BEBC with entry points not far from that of the neutral. There the veto part of the IPF is of vital importance since it can identify most charged particles related to such an upstream interaction. Two different scenarios are covered:

- in cases where the neutral does itself not lead to hits in the IPF - when, due to an insufficient traversed track length (or hadron energy) in the material, the neutral has not produced a hadronic shower, charged secondaries emanating direcly from the upstream vertex can trigger the IPF. They obviously do not even have to enter BEBC to indicate an event related activity.

- in cases where the upstream vertex is so far away from BEBC that the angle of the secondaries prevents them from crossing the IPF, the likelihood of the neutral hadron producing a hadronic shower of charged particles at small angles gives a second chance of detecting upstream activity.

The remaining background will thus arise from two sources:

a) Low energy neutral hadrons from 'far' away or low multiplicity vertices

b) Neutral hadrons produced in interactions in the BEBC wall.

Both background sources will be supressed by a requirement on the minimum energy seen at the vertex in BEBC, since secondary hadrons are known to be biased towards low energy. The events from this second source are named 'wallons' in common parlance. Many of these wallons are actually identified by the SYNTHESIS procedure and thus labelled as hadron induced.

5.2.2 Timeslot Ranking and the Veto Picket Function

The reliability of any decision made on grounds of the IPF information depends first of all on the correct determination of the event time slot. The problem is the selection of one event timeslot on the basis of a pattern of associating and unassociating hits in the veto or exit picket fence for each timeslot of the frame, where the fact whether an observed charged track in BEBC has *predicted* IPF hits (from the extrapolation) that lie within a multiple scattering circle of the *observed* IPF hits determines whether to call the latter *'associating hits'* or not. This is achieved, for each timeslot and separately for each primary vertex on a frame, by calculation of a generalised 'signal to noise' likelihood ratio [64] for the pattern of all IPF hits of a frame except those that are associating to possible other primary vertices (in which case they are not a background for the vertex in question). The 'signal' is the probability that the given pattern of picket associations was caused by the outgoing particles (based upon appropriate known picket efficiences), while the 'noise' is related to the likelihood that the other timeslots are background (based upon known picket false association rates).

In general, this approach would assume that the number of IPF hits arising from interactions or conversion in the chamber wall of event-related neutrals is negligible compared to the number of those hits caused by through-going muons or charged hadrons from upstream interactions - particularly in the neutrino beam the 'halo' of muon noise is large. [1] In practice, however, although there are usually many through-going particles per beam spill, their number per timeslot (300 ns) is known to be small: the likelihood of a through-going muon occurring in the same timeslot as the event is $\leq 1.5\%$ [66]. Thus, contrary to the above supposition, any unassociating IPF hits, at least those in the exit IPF, recorded in the selected event timeslot rather point towards an event related activity that is connected to produced neutrals.

The procedure clearly presupposes the existence of predicted IPF hits, whence any event that does not meet this minimal criterion will by definition have no event timeslot assigned. After the calculation of the appropriately normalised timeslot weight one often finds events with more than one nonzero timeslot weight. A timeslot is then accepted as the event timeslot if its weight exceeds a chosen threshold. One has to compromise between not accepting too many ambiguous events and

[1] This is due to the fact that more positive than negative secondaries are created by protons in the beryllium target so that the total number of (negative) muons created by neutrinos on the way towards the detector is larger than that of positive muons arising from an antineutrino beam.

not permitting too many events with doubtful timeslot assignment. The optimuum value (0.85) was determined from a study of muon track depleted CC events which simulated NC events but had a known event timeslot from the IPF-EMI identified muon. Further details about the timeslot algorithm and its performance are given in [65].

Once the event timeslot is defined, one can use the veto picket detector to quantify the activity upstream of BEBC in this timeslot and thus to try to classify the event as a neutral current candidate (NC) or as hadron induced (HA). Since secondary hadrons have a limited transverse momentum relative to the total momentum of the hadronic shower, of the order of 350 MeV/c, the entry point of a neutral hadron (mostly neutrons and K_L^0) can be expected to be close to entry points of other charged secondaries from the same vertex which give rise to unassociated veto picket hits.

This angular correlation is the basic motivation for defining a picket function that converts the spatial distribution of unassociatied veto IPF hits, relative to an estimated entry point of a hypothetical neutral hadron having caused an interaction in BEBC, into a single number which indicates how much those hits spread around the hypothetical entry point:
from the observed vertex of the interaction in BEBC, one obtains the total momentum vector of all seen particles produced, and extrapolates it backwards to the veto IPF plane, where it defines the estimated entry point. Then θ_i is, for the ith of n unassociated veto IPF hits, the angle in the horizontal plane it subtends relative to the vertex in BEBC and the estimated entry point. Figure 5.1 shows a rather flat distribution in θ_i for CC events, whereas for a naive NC candidate sample it shows a clear indication of IPF activity concentrated near the estimated entry point of the neutral, suggesting a large contamination of a naively defined NC candidate sample

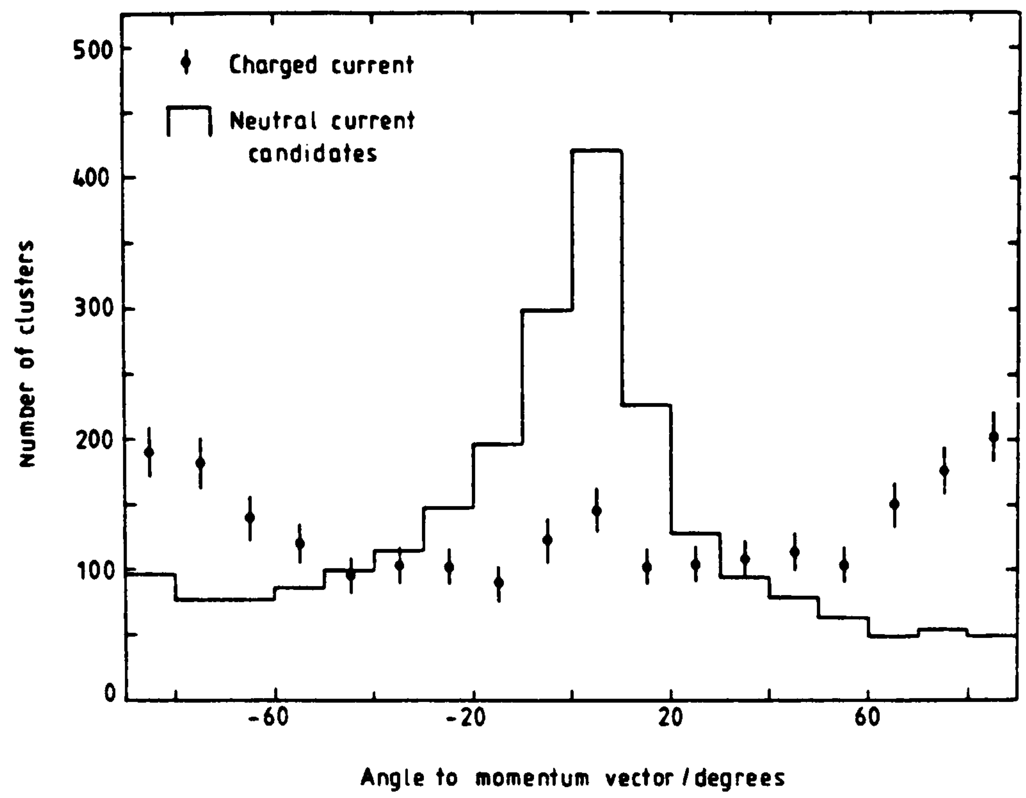

Figure 5.1: *Angle between unassociated veto IPF hit clusters and the hadronic momentum vector. A cluster is defined to be a group of hits in consecutive IPF channels*

by unidentified hadron induced events, as expected. The width of the 'peak' has a contribution from the spread of the IPF hits, as well as from the fact that the direction BEBC vertex - estimated entry point will be uncertain for genuine hadron induced events where many final state particles remained undetected.

The 'Veto Picket Function' F_v is defined by [2]

$$F_v = \prod_{i=1}^{n} (1 - \cos\theta_i) \tag{5.1}$$

and we show the distribution in F_v in figure 5.2, where the data sets are normalised to the same number of 'silent' (ie. $F_v = 1$) events. In the range from 0.1 to 1, the CC and the NC candidate sets show a very similar behaviour, whereas a marked difference occurs in the first bin (of width 0.1; actually, the main discrepancies lie below $F_v = 0.01$), which contains most hadron induced (HA) events. Thus an effective separation of HA from NC events can be achieved by requiring $F_v \geq F_{cut}$

[2]In fact a scaled vertex coordinate $x' = 0.7x$ ($x = 0$ is the center of BEBC) is used in the calculation of F_v, to allow for the transparency of liquid hydrogen to neutrons. Since the change in $\cos\theta_i$ due to this rescaling depends on the distance d of the vertex to the veto IPF like $1/d^3$, events close to the entry wall are assigned a smaller value of $1 - \cos\theta_i$, thus correcting for the fact that their unassociating veto IPF hits *seem* to be less correlated with the event momentum direction.

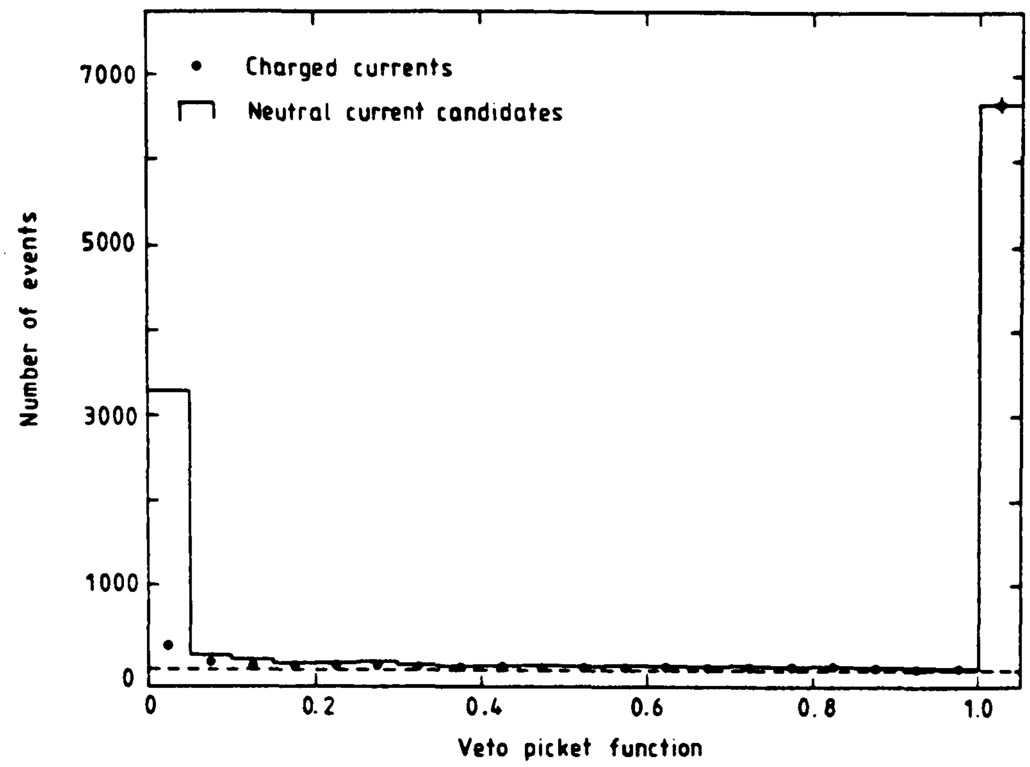

Figure 5.2: *Veto picket function distributions for CC events and NC candidates*

for some chosen low value of the veto picket function cut. On the other hand, it is visible that some CC events have low F_v values as well, so we expect some genuine 'noisy' NC's in the same region of F_v. Most of these 'self-vetoing' events come from the decay of π^0's which send one γ backwards that causes showering in the vessel wall, as a direct investigation of such events on the scanning table showed. Other sources of event related self-vetoing are leaving particles that reenter into the chamber due to the strong magnetic field, or unmeasured tracks from interactions of charged particles of the primary vertex that took place close to the chamber wall. For all the event classes we define in the next section, we also investigated the distributions in $\log_{10} F_V$ for which the different extent of veto picket noise that leads to values $F_v < 0.1$ are more clearly distinguishable.

5.3 Selection of the Event Sample

Here we describe the criteria required to be met by events to be included in the event sample that is considered in the subsequent analysis. In all some 25,400 and 18,900 primary vertices (to the nearest hundred) were found during scanning of

Criterium	Neutrino events	Antineutrino events
BEBC frames	20497	17376
Primary vertices	25394	18902
EMI operative	24492	18309
Inside fiducial volume	17834	14541
$E_{Had} > 5GeV$	11871	7513
≥ 3 charged tracks	11596	7316
$W_{Had} > 1.5GeV/c$	10927	6490
Timeslot well selected	9351	5903

Table 5.1: *Event numbers passing the cuts on the data*

the neutrino and antineutrino films, respectively. The beam monitors and the EMI were required to be operative during the time the frame was taken, which should not introduce any bias in the data.

Since the event classification relies heavily on the IPF information, as described in the preceding section, the normal BEBC fiducial volume, which ensures a sufficient track length in the bubble chamber for the charged particles from the primary vertex, is replaced by a 'reduced' fiducial volume that is defined by the additional restriction on the vertical vertex coordinate $|z| \leq 95cm$, to accept only events with a large fraction of secondaries that traverse the IPF. Through this restriction one loses a small fraction ($\approx 4.6\%$) of classified events but reduces the size of the sample of unclassified events (events without defined timeslot) substantially, by about 20% . The event numbers that pass these requirements can be seen in table 5.1.

As to the cuts in kinematic variables, to ensure a high scanning efficiency it has been customary in analyses of this experiment to introduce a cut in the visible energy, which is the hadronic energy for NC and HA events. To treat all event classes on the same footing, this condition is required to be satisfied by CC events as well. As mentioned before, hadronic events faking NC events are strongly suppressed through this cut. Furthermore, we confine ourselves to event topologies of 3 or more prongs. Unlike in CC events, in the NC case even neutrino induced events have a small proportion of 1 prong events, that is primary vertices with one leaving charged track only. We discard those since the scanning efficiency is very low (about 15%), particular in the neutrino beam the background of through-going muons makes the finding of these events very difficult indeed.

We are interested in the deep inelastic region of phase space. In charged current analyses, a minimum value of the event Q^2 is usually assumed. This is not possible for neutral current reactions in hydrogen since the assignment of an event Q^2 is as meaningless as a naive determination of $x_{(Bj)}$. Nevertheless, we want to exclude the resonance region from the analysis, since the onset of approximate scaling does not occur below a minimum value of Q^2 (around 1 GeV^2/c^2), and moreover since different physical processes dominate the resonance region - namely non-perturbative effects. Thus we are led to introduce a cut on the only Lorentz invariant extensive variable we can measure with sufficient accuracy, the invariant mass of the hadronic system, W. Due to the loss of unseen neutrals in hydrogen, this variable will be underestimated, and care has to be taken in translating a cut on the seen W_{vis} into one on the true W. Now a cut on W induces one on Q^2, which however is not $x_{(Bj)}$ - independent:

$$Q^2 \geq Q^2_{min} = \frac{W'^2_{cut}}{\frac{1}{x} - 1} \tag{5.2}$$

where $W'^2 = W^2 - M_P^2$. In choosing $W_{cut} = 3\ GeV/c$ we maintain that $Q^2_{min} \approx 1\ GeV^2/c^2$ at $x_{(Bj)}$ =0.1. The mean Q^2, on the other hand, is larger even at small $x_{(Bj)}$: from Monte Carlo studies we know that $Q^2_{min} \approx 3.7 GeV^2/c^2$ at $x_{(Bj)}$ =0.05, and $Q^2_{min} \approx 6.6 GeV^2/c^2$ at $x_{(Bj)}$ =0.10. This has to be compared with the overall mean, $< Q^2 > \approx 13.8 GeV^2/c^2$ (all numbers refer to the neutrino case).

Apart from this main motivation for introducing a cut in W, there are several other effects it has on the data sample: since the average number of charged secondaries is known [67] to scale with $\ln W^2$, the resolution on the total hadronic momentum improves as the invisible part of the hadronic shower carries away a fraction of the total hadronic momentum that is determined the better the more tracks are seen.

The W cut will practically eliminate all 1 prong events in the data since for such an event W is the mass assigned to one track only. This is a welcome bias, for the uncertainty in the scanning efficiency for the 1 prong class is large. Finally, due to the anticorrelation of the average W for fixed window in $x_{(Bj)}$ or w, events with large values of w will be supressed. Since the W cut will remain imposed in the final results for obvious reasons, we do not have to correct the $w > 0.5$ region where the resolution in w is poor and not well known, due to the small number of events with such high values in w.

For the choice of the cut on the *visible* W_{vis} we note that W is always underestimated, ie. $W^2_{vis} \leq W^2_{true}$. For a small bin around $W_{true} = 3\ GeV/c$ we find $< W_{vis} >_{W\approx 3} \approx 2.3\ GeV/c$ and $\sigma_{W_{vis}, W\approx 3} \approx 0.5\ GeV/c$. To include most of the events with a true W of 3 GeV/c or more we are suggested to impose $W_{vis} \geq$ 1.5 GeV/c on the data. This leads to smaller correction factors later and prevents the dropping of the about 40% of events with values of the visible W between 1.5 and 3.0 GeV/c.

The event classes are now defined as follows:

Any event which does not have a uniquely defined timeslot with weight larger than the threshold weight enters the unclassified set of so-called 'Don't Know' (DK) events. We further discard all events which have an upstream vertex in the same timeslot. This does not affect the number of classified neutral current and charged current events , whereas the DK and HA classes, which are not unbiased (the timeslot weight is not independent of the kinematics), suffer a small reduction (by 3%). The remaining classified events, 9351 (5903) for the (anti)neutrino case, are divided into the following classes:

- CC: events with an EMI identified muon with momentum of at least 3 GeV/c
- DM: CC dimuon events with the additional requirement of ≥ 2 charged tracks in distinct regions of the EMI outer plane in the same timeslot
- NC: events with no identified muon and $F_v > 0.01$, and without a through-going muon that has recorded hits in the veto and exit Picket fence and both EMI planes (Inner and Outer), but not in the Veto EMI ($\bar{V}P_VP_XIO$) type
- HA: all others, ie. flagged by low F_v values or a through-going muon

The respective event numbers entering these classes can be seen in table 5.2. To obtain an impression of the w distribution of these classes, we display the raw w distributions in figure 5.3. The NC class consists to about 85% of 'silent' events, ie. events with a veto picket function value of 1 (no upstream picket activity). On the other hand, only a few events in the HA class have this F_v value, so that the silent NC candidates are to a good approximation genuine NC events (we discuss silent hadron events in section 1.4.3 below). From figure 5.3 we can observe that the w behaviour of this subclass agrees within statistical errors with the one of the remainder of the NC class, ie. events with $10^{-2} \leq F_v < 1$. It can be further discerned that also the HA and DK w distributions are similar in shape to the NC w distribution. We separated the HA class into two subclasses, where those HA events

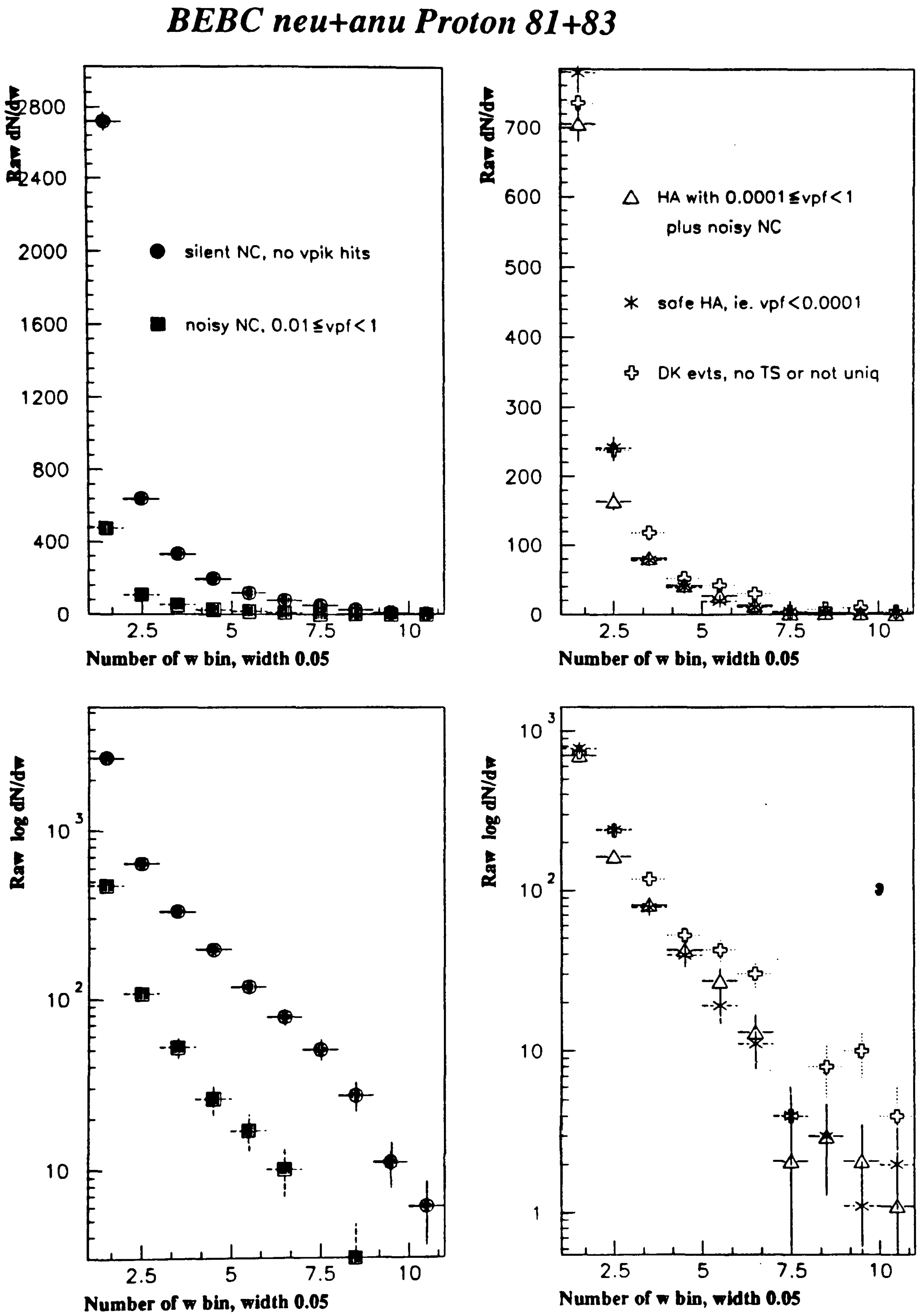

Figure 5.3: *Raw w distributions of different event classes, neutrino and antineutrino added*

Event class	ν sample	$\bar{\nu}$ sample
CC total	5218	3592
CC right helicity	4959	2943
CC wrong helicity	259	649
Dimuon events	50	14
NC total	2943	1882
NC silent	2452	1626
NC noisy	452	229
NC unbalanced charge	41	28
HA	1140	415
DK	1576	587

Table 5.2: *Event classification on the data sample after all cuts*

with $F_v \leq 10^{-4}$ will contain very few genuine NC events, since only 0.9% of the CC events have such low F_v values. This reasoning assumes that the NC and CC F_v distributions are the same, a hypothesis that is not strictly true, but the agreement is sufficient to draw the above conclusion.

5.4 From the Raw to the Corrected w Distributions

During the collection and processing of the data, as well as the analysis itself, some genuine events will fail to be registered, or wrong hypotheses are made about them. Secondly, although an event can be correctly identified, some of its properties, like values for kinematical quantities, can be misjudged due to measurement errors etc. We have to correct for these effects that are inherent in any non-ideal experiment. The corrections fall into several steps:

- 'registration' corrections: we only have to consider those inefficiencies that lead to a bias in the data sample. In the present context, this is the inefficiency of the scanning process. Other requirements made on the data, like the well-functioning of certain detector components, are independent of the event type and kinematics.
- 'classification' corrections: events are not necessarily of the type they are assumed to belong to, for instance hadron-induced or neutrino-induced.
- 'beam' corrections: the beam is not pure but contains contaminations from different neutrino flavours and opposite helicity.
- 'cut' corrections: the cuts on the data are imposed on the measured quantities and have to be corrected, to refer to true values. Cuts in quantities that have no direct kinematic interpretation, like the number of charged tracks, have to be removed.

In the following sections, we shall deal with each of the necessary corrections in detail. Since we aim at extracting a w distribution, each correction has to be applied in dependence on w. The fact that the cross section scales in w approximately will be of help in several situations.

The correction for the contamination due to hadron induced events assumes a central role in the analysis. However, since the variable w is a scaling variable in the Bjorken approximation, the fact that hadronic events are biased with respect to extensive variables, like the energy of the hadronic system E_H, does not necessarily mean that the w distribution of the contaminating events introduce a strong bias in the NC candidates' w distribution. On the contrary, we have seen above that the w distribution of those events with a value of the veto picket function below 10^{-4} shows a similar behaviour to the one of the NC candidates.

5.4.1 Correction for Scanning Efficiency

The likelihood of an event being reckognised in the scanning process depends on the event topology and the beam-associatied background of tracks on the frame. The scanning efficiency is obtained from two different scans of the same data that are assumed to be independent. If for a sample of N events $N_{1(2)}$ and N_{12} are the numbers of events found in scan 1(2) only, and in found both scans, respectively, then the estimate of the efficiency $\epsilon_1 \equiv (N_1 + N_{12})/N$ of scan 1, for instance, is (N is unknown!)

$$\hat{\epsilon}_1 = \frac{N_{12}}{N_2 + N_{12}} \tag{5.3}$$

and depends on the number of events found in the other scan. Using the estimate $\hat{N} = (N_{12} + N_1)(N_{12} + N_2)/N_{12}$ for N, one has for the estimate $\hat{\epsilon}_{scan}$ of the overall scanning efficiency ϵ_{scan}:

$$\hat{\epsilon}_{scan} = \frac{N_{12}(N_1 + N_2 + N_{12})}{(N_{12} + N_1)(N_{12} + N_2)} \tag{5.4}$$

These formulae assume that all events are equally likely to be found, which is not strictly valid, as higher multiplicity events, for instance, are easier to find. Thus

Charged multiplicity	1981		1983	
	NC	CC	NC	CC
3	0.92 ± 0.02	0.92 ± 0.02	0.92 ± 0.02	0.98 ± 0.01
≥ 5	0.99 ± 0.01	0.99 ± 0.01	0.99 ± 0.01	1.00 ± 0.01

Table 5.3: Scanning efficiency for NC and CC events in dependence on the charged multiplicity.

the efficiency has to be calculated as a function of multiplicity. Wtih the IPF information, it was possible to obtain predicted muon leaving points from timeslots with IPF and EMI hit patterns consistent with a muon hypothesis. These predictions were used to find further CC events in a 'prediction scan', which gave a better estimate $\hat{N}'$ of N. For the 1983 data, the events found in addition by this method were added to the CC sample. For events with $E_H > 5\ GeV$, the values displayed in table 5.3 were obtained, using the results of the prediction scan and assuming that for the same year the neutrino and antineutrino film were scanned with equal efficiency. The observed events are then weighted with the inverse of the scanning efficiency. The mean weight for the (anti)neutrino NC sample is found to be 1.026 (1.035).

Figure 5.4 shows a 9-prong event from the antineutrino NC data sample which passes a threshold of $w > 0.05$ and has no leaving track identified as a muon, and a veto picket function value of 1.0 (silent). The frame of figure 5.5 cntains a 3-prong vertex with a close-by V^0 interaction and another one 1.8m downstream.

5.4.2 Treatment of Unclassified Events

After events with a unique timeslot have been classified as described in the previous sections, there remains a fraction of 14.7% and 9.2% (after all cuts) in the neutrino

Figure 5.4: *Example of an event consistent with the NC hypothesis, showing the conversion of two* γ *and a* $\pi - \mu - e$ *decay chain.*

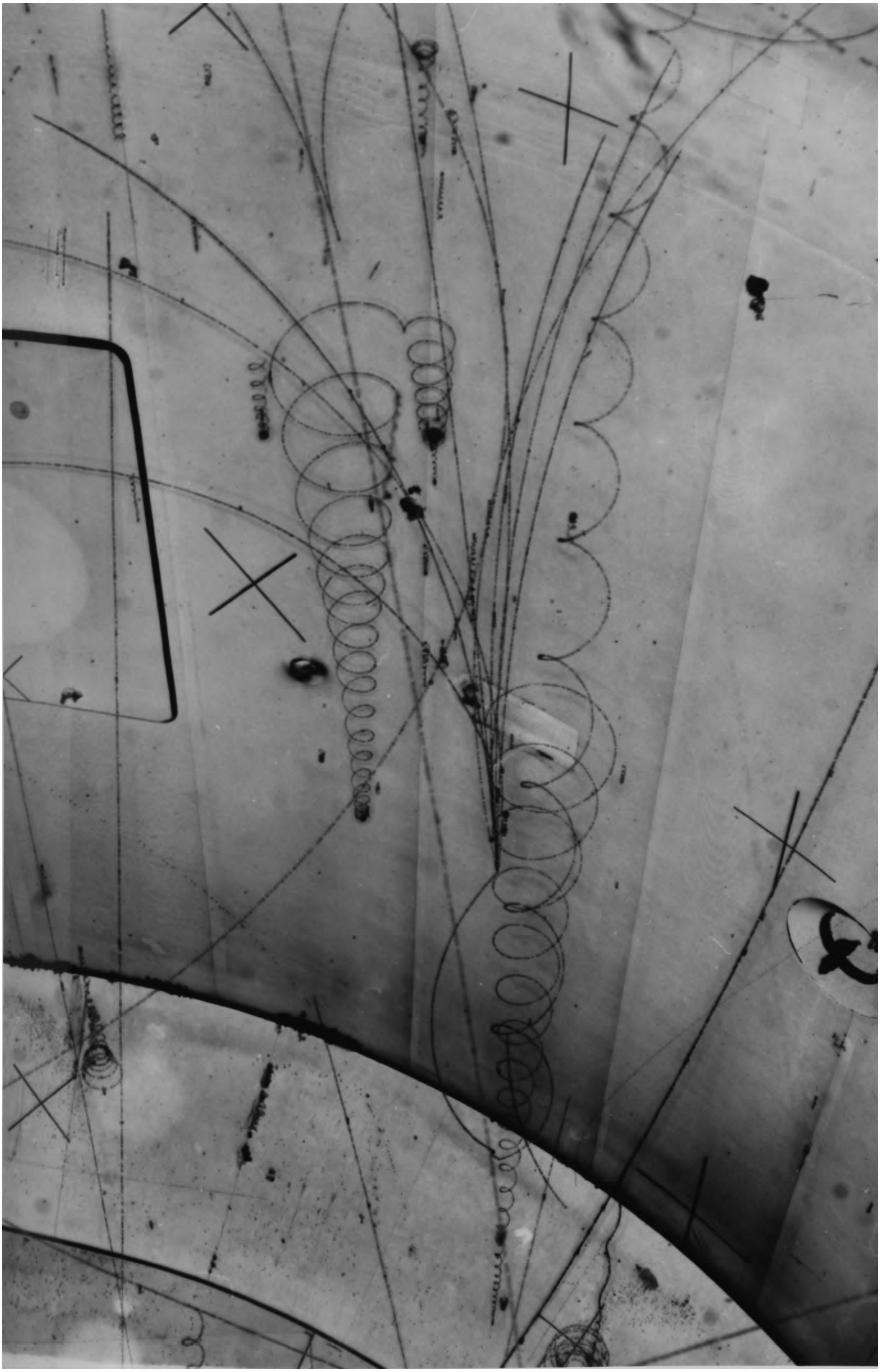

Figure 5.5: *Example of an event consistent with the NC hypothesis, showing the decay of two V^0 particles into hadrons that in turn interact with protons.*

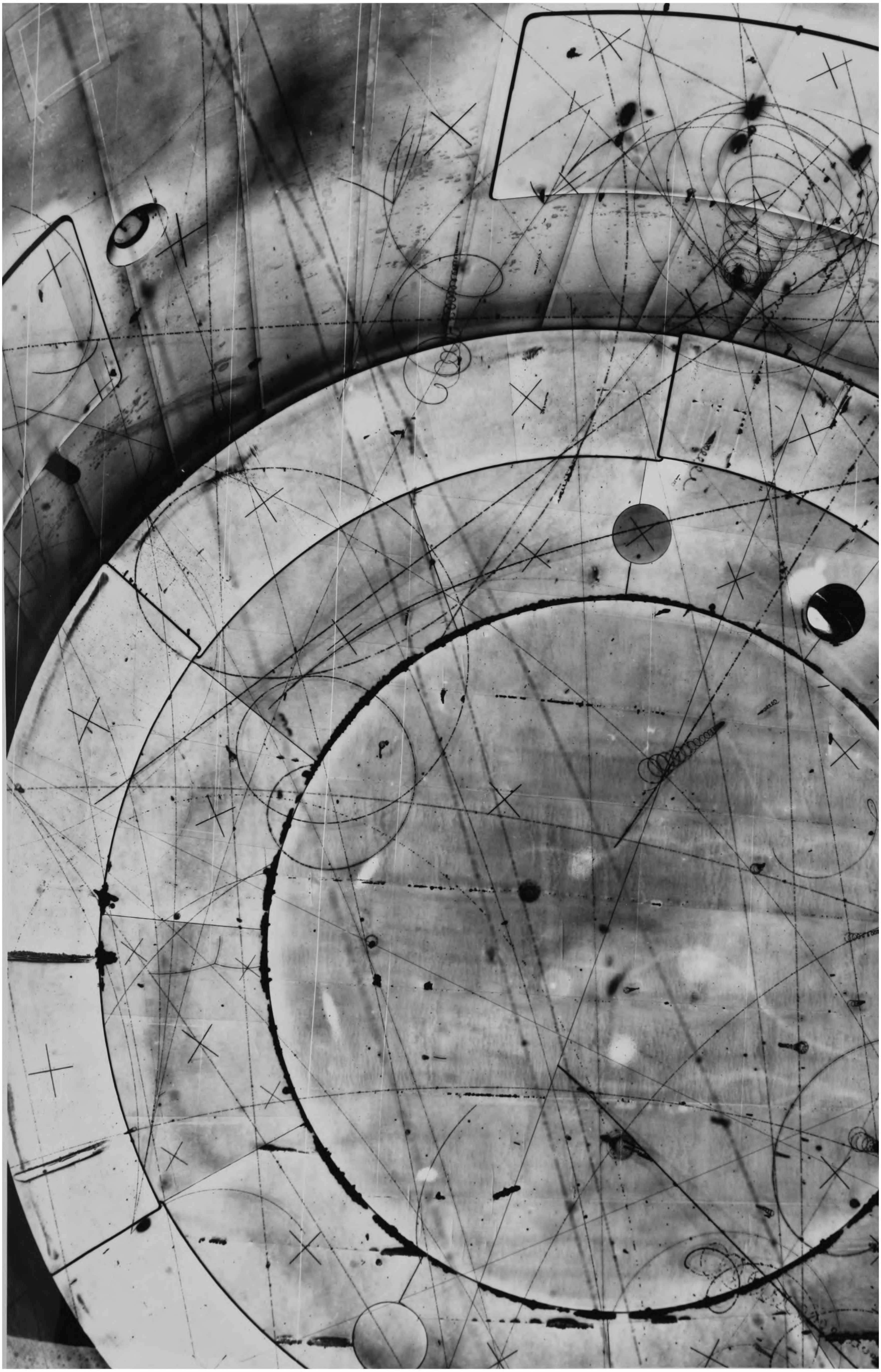

and antineutrino sample, respectively, for which the timeslot weighting algorithm did not identify a unique event timeslot. This can occur because

- No timeslot has a weight greater than the threshold weight. This comprises events with one such timeslot only, and events with several 'ambiguous' timeslots (necessarily below threshold, since $W_t = 0.85 > 0.5$), for instance three timeslots of equal weight 1/3.
- No acceptable timeslot has been recorded at all. A subset of this is the set of events with no predicted track to cross the IPF.

It is now necessary to divide the sample of unclassified events, the so-called 'Don't Know' (DK) set, into either NC or HA candidates. There will also be a small fraction of misidentified CC events in the DK set, which has to be considered by applying the correction for the overall contamination of the NC set due to misidentified CC events *after* the DK correction. The partition will be carried out on a statistical basis. We will not use the crude approximation that the ratio of NC to HA events in the DK set is the same as in the classified set. The probability that a certain event is classified is clearly not uncorrelated with its kinematics. Unclassified events will be biased towards lower hadronic energies and lower multiplicities, we expect the fraction of HA events to be larger than in the classified set. Therefore, we shall use a variable that is correlated with the event kinematics and directly related to the timeslot ranking algorithm: the number of tracks predicted to cross the IPF. This idea has been introduced in [68]. We calculate the probability $P_{DK}(N_{PT})$ for an event with N_{PT} predicted tracks (PT) not to be classified, for fixed N_{PT}, as

$$P_{DK}(N_{PT}) = 1 - P_{CL}(N_{PT}) \tag{5.5}$$

$$P_{CL}(N_{PT}) = \frac{CL(N_{PT})}{CL(N_{PT})+DK(N_{PT})}, \tag{5.6}$$

N_{PT}	Neutrino	Antineutrino
1	0.444 ± 0.023	0.644 ± 0.023
2	0.764 ± 0.014	0.877 ± 0.018
3	0.884 ± 0.015	0.955 ± 0.020
4	0.951 ± 0.017	0.976 ± 0.022
≥ 5	0.984 ± 0.013	0.990 ± 0.018

Table 5.4: ***Probability for an event to be assigned a unique timeslot as a function of the number of tracks predicted to cross the IPF***

where CL is the number of classified events (ie. CC or DM or NC or HA), and DK the number of unclassified events, in a symbolic notation. Since the likelihood of an event having its timeslot determined also depends on the level of background hits in th IPF, these probabilities are beam dependent. Table 5.4 shows the probabilities P_{CL} for the two beams. The estimated number $\Delta^{(DK)}_{(NC)}$ of NC events in the DK sample for fixed N_{PT} is then obtained by weighting the observed number of NC events with the same N_{PT} with the probability not to have a unique timeslot:

$$\Delta_1(N_{PT}) = NC(N_{PT})\, P_{DK}(N_{PT}) \tag{5.7}$$

This procedure can be applied to all events in the DK set except those with no predicted tracks, $N_{PT} = 0$. In the (anti)neutrino sample 171 (108) out of 1613 (601) DK events thus remain to be considered. We split those according to the proportion of NC (HA) events with $N_{PT} = 1$ *relative* to the total number of NC (HA) events, in the sum of NC and HA events :

$$\Delta_0 = NC(N_{PT} = 0)\, \frac{nc}{nc + ha}, \tag{5.8}$$

where $nc = NC(N_{PT} = 1)/NC_{tot}$, and similarly for ha. An overall error of 50% is then assigned for this contribution. The total number of estimated NC events in the DK sample is then

$$\Delta^{(DK)}_{(NC)} = \Delta_0 + \sum_{N_{PT}} \Delta_1(N_{PT}) \tag{5.9}$$

and we obtain 450 ± 62 (250 ± 51) events for the (anti)neutrino case. The con-

N_{PT}	$\Delta^{(DK),\nu}_{(NC)}$	$\Delta^{(DK),\bar{\nu}}_{(NC)}$
0	110.0 ± 55.0	92.0 ± 46.0
1	95.6 ± 11.2	67.6 ± 9.3
2	123.4 ± 12.8	57.6 ± 11.1
3	75.5 ± 12.8	20.5 ± 10.1
4	29.6 ± 11.5	7.8 ± 7.5
≥ 5	15.9 ± 13.4	4.5 ± 8.2

Table 5.5: *DK correction to the (anti)neutrino sample*

tributions for the different values of N_{PT} can be seen in table 5.5. To implement the obtained NC numbers, we scale the w distribution (after weighting for scanning eficiency) of the DK set by the overall ratio Δ/DK. There is a bias in this treatment if the w distributions of the DK set, for fixed N_{PT}, vary with N_{PT}. To a small extent, that is the case, and we have recalculated the correction by weighting those individual w distributions according to the ratios $\Delta(N_{PT})/DK(N_{PT})$ before summing over N_{PT}. The difference to the result obtained with the 'overall' ansatz is much smaller than the statistical errors for most of the w bins, except for $w \geq 0.3$ where they are of comparable magnitude.

5.4.3 Noisy NC and Calm HA Misclassifications

The combination of the Veto picket fence detector with the BEBC-EMI system and the construction of the picket function criterion permits an effective separation of NC events from hadron-induced events. Here we are concerned with the misclassification due to two sources: genuine NC events with low values of the picket function ($F_v < 10^{-2}$), hereafter named 'noisy' NC, and hadron-induced events which fail to be recognised as such, because of a large value of the picket function ($F_v > 10^{-2}$) *and* the absence of a through-going muon, called 'calm' HA, a subset of which are those with no veto picket hits at all , ie. $F_v = 1$, called 'silent' HA. We already commented on the physical processes giving rise to the misclassifications in section 1.2.2.

Of the HA candidates, about 42% have a through-going muon of $\bar{V}P_V P_X IO$ type in the same timeslot, however only $(6.5 \pm 1.3)\%$ are flagged by this occurrence alone, having a picket function value larger than the cut. We have to estimate the fraction of genuine HA events with $F_v > 10^{-2}$ that enter the NC class because of the absence of a through-going muon. The distribution of the HA events which do have a through-going muon is approximately flat in $\log F_v$. Those events will be largely unbiased, since the primary neutrino vertex will be close to the chamber and thus should produce a through-going muon in case the parent event is a CC interaction (the random association due to spurious IPF hits is known to be less than 1%). If we neglect a possible, but certainly negligible admixture to the HA class of noisy NC and misidentified CC events, in the region $F_v \leq 10^{-4}$, we can obtain an estimate of the number of calm HA events in the NC class by scaling the observed number of HA candidates with $F_v > 0.01$ *and* a through-going muon by $(1 - r_{TM})/r_{TM}$, where r_{TM} is the fraction of HA candidates below the picket function value $F_v = 10^{-4}$ that have a through-going muon. This gives 90.1 ± 29.2 (30.0 ± 15.3) events in the (anti)neutrino case.

For the 'noisy' NC events, ie. those with $F_v < 0.01$, we have to calculate the ratio

$$\frac{NC\ events\ with F_v < 0.01}{NC\ events\ with\ 0.01 < F_v < 1} \tag{5.10}$$

and assume it to be the same for the CC and NC classes, which is a weaker statement than requiring the respective F_v distributions to be identical. The agreement between the NC and CC picket function distributions is sufficient to warrant the use of this weaker assumption. We obtain a ratio of 0.276 ± 0.32 and (0.0236 ± 0.42). Once the calm HA and noisy NC correction are known in size, we subtract and add the appropriately normalised known w distributions of the HA set with $F_v < 10^{-4}$ and of the NC set with $0.01 < F_v < 1$, respectively. As we saw earlier, these two w

distributions are very similar in shape and are certainly applicable for these small corrections.

5.4.4 Misidentified Charged Current Events

The second main correction stems from those genuine charged current events that fail to be identified as such, due to the muon either

- not leaving the bubble chamber since its momentum is too low,
- or not crossing the active region of the IPF and EMI detectors for geometrical reasons,
- or not firing the IPF of EMI for electronic inefficiency reasons.

Contrary to the DK correction, this contamination of the NC set introduces a marked bias in the w distribution, since the genuine muon is regarded as a hadron and included in the calculation of the event hadronic p_T and p_L. Thus we expect extremely small values of w for the events of this contamination. Indeed, more than 95% of the CC events have a w value smaller than 0.05, compared to about 65% for the NC case. The imposed cut on the hadronic energy reduces the event sample appreciably, but will not have any rejecting power with respect to the misidentified CC events, whose relative contribution increases. Thus we are left with two possible courses of action: either we restrict our attention to a region in w above a suitable cut, like $w > 0.05$, thereby removing almost the entire CC contamination, or we evaluate the size of the contamination and subtract a corresponding fraction of the CC w distribution from the NC candidate w distribution, with an estimated systematic error. Since we prefer not to restrict the w region investigated, and have knowledge about the inefficiencies of the detector system, we choose the latter alternative. There are then three sources for contributions to the correction:

The EMI geometrical inefficiency

Muons can emanate from CC interactions with directions that prevent them from crossing the region covered by the EMI. The relevant variables determining this geometrical inefficiency are the muon momentum, to which the deflection in the magnetic field is inversely proportional, its polar and azimuthal angles about the beam direction, and the event vertex position. Since we are not interested in the spatial distribution of events in the chamber, the vertex position is always averaged over, and the geometrical inefficiency is parametrised in terms of the muon momentum and the polar angle about the beam direction only (the azimuthal angle is again not entering any investigation of structure functions, however in the CC case the scaling variables are usually calculated using the muon polar angle).

This acceptance α_{geom} has been obtained in [64] using a Monte Carlo simulation incorporating the (anti)neutrino flux shape in the generation of the vertex position and energy. Muon momenta were generated from flat distributions and then extrapolated using the same EMI routines as in the data production chain. For the wrong helicity component of the beam the spatial and energy distributions were taken from the data, as we have insufficient knowledge about the flux of the defocused part of the beam. The resulting acceptance α_{geom} is shown in table 5.6 and has been found to be independent of the beam type and energy within statistical errors. Since the asymmetrical arrangement of the EMI is optimised for the right helicity beam component, the acceptance is lower for the wrong helicity part. The acceptance becomes small and uncertain below a value of 3 GeV/c for the muon momentum and we therefore accept as CC events only those with muon momenta above this value. The contribution from CC events with muon momenta below 3 GeV/c is calculated by Monte Carlo separately, described below. The implementation of the EMI acceptance thus found has to be done on an event by event basis

p^{μ} GeV/c	p_T^{μ}/p^{μ} 0.0–0.1	0.1–0.2	0.2–0.3	0.3–0.4	0.4–0.5
3–4	0.950	0.920	0.812	0.635	0.480
4–5	1.000	0.973	0.882	0.716	0.536
5–6	1.000	0.976	0.900	0.736	0.575
6–8	1.000	0.977	0.903	0.760	0.623
8–10	1.000	0.979	0.906	0.784	0.650
10–15	1.000	0.983	0.910	0.828	0.700
15–20	1.000	0.986	0.916	0.860	0.750
20–25	1.000	0.990	0.920	0.890	0.800

p^{μ} GeV/c	p_T^{μ}/p^{μ} 0.0–0.1	0.1–0.2	0.2–0.3	0.3–0.4	0.4–0.5
3–4	0.430	0.420	0.392	0.351	0.302
4–5	0.592	0.583	0.533	0.463	0.357
5–6	0.728	0.703	0.639	0.519	0.398
6–8	0.873	0.822	0.711	0.568	0.449
8–10	0.949	0.897	0.766	0.625	0.500
10–15	0.986	0.942	0.831	0.709	0.550
15–20	0.997	0.966	0.880	0.750	0.600
20–25	0.999	0.975	0.910	0.800	0.650

Table 5.6: *The EMI geometrical acceptance α_{geom} as a function of the muon momentum and polar angle $sin(\theta) = (p_T/p)_{\mu}$ for the right- and wrong-helicity beam component*

as it cannot be assumed that the genuine CC events misidentified as NC due to the geometrical inefficiency have the same w behaviour as the identified CC events. We weight each identified CC event by

$$\omega_{geom} = \frac{1}{\alpha(\theta_\mu, |\vec{p_\mu}|)} - 1. \tag{5.11}$$

Indeed, it is found that the w distribution arising from these weights is significantly harder than the one of the identified CC events. The weights have to be applied to all identified CC events with $E_H > 5\ GeV$ and in addition to those with $E_H + E_\mu > 5\ GeV$ since the latter will not be rejected by the energy cut and thus enter the NC candidate set. This enlarged CC sample contains 50% (100%) more events than the standard CC sample for the (anti)neutrino case, showing that the correct implementation of the weights is crucial to the correction. The substantial increase can be understood by recalling that the hadronic energy cut removes a large part of the events found in the fiducial volume (see table 5.1), most of which are CC events from (anti)neutrinos with energy near the mode of the flux spectrum. The same procedure applies to the cut in the hadronic invariant mass, however very few CC events with $E_H + E_\mu > 5\ GeV$ are rejected by the W_H cut.

The EMI electronic inefficiency

All remaining inefficiencies of the EMI detection system, which is here understood to include the EMI data processing chain, that are not connected to the purely geometrical acceptance, are collectively referred to as 'EMI electronic inefficiency'. The various contributions to this source of misclassification of CC as NC events are:

- purely electronic inefficiencies of the chambers in the charge collection and signal registration system
- gaps between individual chambers and dead regions (walls etc.)

- software inefficiencies
- multiple scattering fluctuations and track measurement errors.

The combined probability of the EMI recognising the traversal of a charged particle is independent of the particle momentum at the muon energies involved. Hence a purely statistical fraction of the genuine CC events enters the NC candidate sample and can be assumed to have the same w distribution as the identified CC events. We correct the w distribution by weighting the observed charged current w distribution, calculated under inclusion of the muon, by the inverse of the EMI electronic efficiency. The fact that a genuine CC event which does not pass the cut in the hadronic momentum can still be accepted if the muon is mistakenly included into the hadronic system has to be accounted for and is contained in a factor $f(E_H^{cut}, W_H^{cut})$. We checked that the w distribution of the CC sample with a total visible energy of more than 5 GeV is not different from the one of the CC class defined above. We thus add to the w distribution

$$\Delta^{CC,elec} = (\frac{1}{\epsilon_{elec}} - 1)\ f(E_H^{cut}, W_H^{cut})\ \frac{dN_{CC}}{dw}. \tag{5.12}$$

The electronic efficiency ϵ_{elec} has been calculated in two different ways that give consistent results. One has to use some property of the CC muons that identifies them without the help of the EMI muon identification whose performance is to be assessed.

One alternative is to exploit the fact that the muons from deep inelastic interactions will on average have a larger p_T (with respect to the beam direction than any individual hadron in the current or target jet, due to the limited momentum spread of individual hadrons around the jet axis, and the fact that the collection of hadrons has to balance the muon p_T (For the center of momentum energies achieved in this experiment the different behaviour of hadrons from the current and target jet is not yet significant). Then one can obtain an estimate of the electronic efficiency by fitting the transverse momentum distribution of π^- hadrons in NC candidate events to a linear combination of the transverse momentum distributions of π^- hadrons in CC events and of identified muons from CC events. From this investigation a value of $\epsilon_{elec} = 0.957 \pm 0.007$ has been found. It must be assumed that the p_T distributions of genuine hadrons in NC and CC events are identical, and that the difference in the p_T distributions of the particles assumed to be hadrons in the NC sample to the one of CC hadrons arises exclusively from a contamination of genuine CC muons. This is not strictly the case, but the procedure can be justified by stating that a similar analysis using the distribution in p_{T_H}, ie the transverse momentum with respect to the direction of the hadronic system, yields consistent results; secondly, the p_T spectrum of hadrons in CC events is found to be insensitive to the beam helicity and thus to the detailed form of the differential cross-section.

A similar method [69] uses a different quantity, the so-called F variable, that has been introduced in [70] to identify muons, instead of the muon p_T. A value consistent within errors to the above was found, while here it is not necessary to assume the equality in shape of the F distributions, but only that of event number ratios above and below a cut in F. Another data set that can be used in principle is a sample of identified through-going muons.

Low momentum muons

For muons with momenta below 3 GeV/c the EMI geometrical efficiency is low and badly known. It contains the effect on the efficiency of those muons that do not leave BEBC, due to the position of the vertex and/or the low momentum. This contamination can only be corrected for by simulating the muon spectrum of CC events. We use the Monte Carlo described in the next section to obtain the ratio $N_{CC}^{p_\mu<3}/N_{CC}^{p_\mu>3}$ within the cuts imposed on the sample. Since the muon of any identified CC event in the data must have passed the same momentum cut of $p_\mu > 3$ GeV/c, we scale the CC w distribution by the above ratio. Again the fact has to be considered that the hadronic energy of the CC events can be lower than the cut value as long as the total visible energy exceeds it.

5.4.5 Wrong Helicity and Electron Neutrino Background

So far, the incident neutrino has been considered naively to be of the desired type. From the generation of the beam described in chapter 3, we expect, however, two beam contaminations to mix into our data sample:

- Due to the focusing system not being ideal, some parent hadrons of the defocused charge will enter the decay tunnel and lead to a wrong helicity background. This is known to be larger in the antineutrino than in the neutrino beam since positive particles, leading to decay neutrinos, are produced more abundantly in proton interactions.
- The electron decay modes of the parent hadrons and a few muons that decay in flight give rise to a ν_e ($\bar{\nu}_e$) contamination.

The wrong (sign) helicity background (WS, RS = right sign helicity) is about 5% in the neutrino beam and about 22% in the antineutrino beam. We calculate the correction to the w distribution due to this source using the observed number of wrong helicity CC events and scaling it by the measured NC/CC ratio [72]. This assumes that the observed w distributions, that is the beam flux shape folded with the w dependence of the cross section, to be the same e.g. for neutrino events from the neutrino beam and from the background to the antineutrino beam. Although the flux shape of the right helicity neutrinos in one beam and of the wrong helicity background in the other is not identical, the fact that the cross section displays approximate scaling in w justifies the assumption in the context of a correction calculation. Then the appropriate amounts of the w distributions, corrected for all backgrounds so far, are subtracted from each other. For instance, we first subtract

$$\Delta^{WS}{}_{\bar{\nu}}(w) = (N_{CC}^{WS})_{\bar{\nu}}\,(\frac{NC}{CC})_{\nu}(\frac{1}{NC}\,\frac{dN_{NC}}{dw})_{\nu} \tag{5.13}$$

to correct the antineutrino w distribution, and then use this corrected distribution for the subtraction of the antineutrino contamination in the neutrino sample. The procedure can in principle be iterated until the differences found are insignificant compared to the statistical errors. The number of wrong helicity CC events found were 259 (649) in the (anti)neutrino sample, which has to be compared to the 4959 (2943) CC events with correct helicity.

The correction for electron neutrino beam contamination is again done on a statistical basis, using the corrected observed CC and the NC w distributions. There are two separate corrections:

- charged current events producing electrons and positrons will always be misclassified as NC since the electron does not reach the EMI planes. Taking r ($\bar{r}$) to be the fraction of electron to muon (anti)neutrinos in the beam, we have to subtract, for instance in the neutrino case,

$$r\,\left(\frac{dN'}{dw}\right)_{CC-RS} + \bar{r}\,\left(\frac{dN'}{dw}\right)_{CC-WS} \tag{5.14}$$

  where the CC w distribution counts the muon into the hadronic system, and N'_{CC} are all CC events with visible energy (muon and hadrons) of at least 5 GeV. From the appropriate branching ratios and momentum spectra of the various components of the secondary hadron beam the values $r = 0.015 \pm 0.004$, $\bar{r} = 0.009 \pm 0.002$ have been calculated [69]. With those we obtain 114.3 ± 29.3 and 73.1 ± 13.0 events.

- There is also an electron neutrino NC contribution that should be subtracted as we are aiming at a flavour pure NC sample. In this case,

$$r\,R\left(\frac{dN}{dw}\right)_{CC-RS} + \bar{r}\,\bar{R}\left(\frac{dN}{dw}\right)_{CC-WS} \tag{5.15}$$

has to be used with an input of the NC/CC ratio. The size of the correction is small and not sensitive to the exact value of this ratio: 31.3 ± 8.3 and 12.7 ± 2.1 for the (anti)neutrino beam.

5.4.6 The w Distribution of the Background-subtracted Sample

Apart from the corrections that we discussed in some detail above, the other possible contaminations that arise are:

- Pion decay-in-flight producing a muon energetic enough to reach the outer EMI plane and faking a CC event, or a charged hadron accidentally traversing the shielding and firing the EMI (punch-through).
- The random association of extrapolated hadron tracks with EMI noise hits leading to fake successfully associating muon tracks.
- Incorrect timeslot selection.

Each of these effects is known to be well below the 1% level from previous studies in the collaboration [66][64], and in particular they do not induce a bias with respect to w due to their random nature. Thus we cannot expect any distortion of the extracted w distribution from these sources and therefore neglect them in the further analysis. In any case the statistical errors alone turn out to be much larger than the linear sum of these effects.

In tables 5.7 and 5.8 we display the w-dependent corrections to the raw neutrino and antineutrino sample, respectively. The background subtractions due to event misclassifications (NC/HA separation, DK class treatment, and CC events seen as NC due to an unobserved muon) are summed before the wrong helicity and ν_e contaminations are accounted for, to better illustrate the relative size of these beam contaminations. All numbers refer to samples corrected for scanning losses, thereby non-integer values appear throughout. The errors are combinations of statistical and systematical contributions, added in quadrature. In cases when they were calculated using correction factors, the error on the factor determined the systematic part of the total error. The systematic errors dominate the corrections at low w in most cases. In particular, the CC correction for the electronic efficiency of the EMI acquires a substantial relative error from the uncertainty in ϵ_{elec} that is propagated to $\frac{1}{\epsilon_{elec}} - 1$.

w_0 :	0.05	0.10	0.15	0.20	0.25	0.30	0.35	0.40	0.45	0.50
silent NC	1670.8	391.4	186.0	124.6	72.4	46.0	31.2	11.8	5.4	3.1
$\pm$	41.1	19.9	13.8	11.3	8.6	6.9	5.6	3.5	2.4	1.8
noisy NC	399.5	95.7	50.9	18.2	13.1	8.2	0.0	1.4	1.3	1.3
$\pm$	30.2	12.2	8.6	4.9	4.3	3.4	0.0	1.4	1.3	1.3
calm HA	-61.2	-16.8	-6.1	-2.8	-1.6	-0.6	-0.2	-0.1	-0.0	-0.1
$\pm$	20.0	5.5	2.0	0.9	0.5	0.2	0.1	0.1	0.0	0.1
unclassified	265.5	83.2	41.9	23.4	11.7	6.3	6.3	4.1	1.8	0.9
$\pm$	49.7	11.5	7.5	4.5	2.2	1.5	1.8	0.8	1.3	0.8
EMI-ϵ_{elec} : CC	-234.7	-9.2	-1.7	-0.5	-0.3	-0.1	-0.1	-0.0	-0.1	-0.0
$\pm$	42.2	1.6	0.3	0.2	0.1	0.1	0.1	0.0	0.1	0.0
EMI-ϵ_{geo} : CC	-142.4	-14.5	-4.4	-2.4	-1.5	-0.4	-0.8	-0.0	-0.3	-0.7
$\pm$	20.2	1.5	0.5	0.4	0.5	0.2	0.6	0.0	0.2	0.5
$\lvert\vec{p}\rvert_\mu < 3$: CC	-617.5	-31.7	-3.6	-0.7	-0.7	-0.0	-0.0	-0.0	-0.0	-0.0
$\pm$	67.9	3.5	0.4	0.3	0.3	0.0	0.0	0.0	0.0	0.0
b/g-subtr. NC	1280.0	498.2	263.0	159.8	93.1	59.4	36.4	17.2	8.2	4.5
$\pm$	110.8	26.9	18.0	13.2	9.9	7.8	5.9	3.9	3.0	2.4
wrong helicity	-56.1	-21.7	-13.5	-6.9	-4.8	-3.3	-1.6	-1.4	-0.6	-0.3
$\pm$	11.2	5.7	3.9	2.8	2.3	1.9	1.3	1.2	0.5	0.3
ν_e background	-124.2	-10.9	-4.3	-2.5	-1.3	-0.8	-0.5	-0.2	-0.1	-0.1
$\pm$	27.5	2.1	0.9	0.6	0.3	0.2	0.2	0.1	0.1	0.1
pure ν_μ NC	1099.7	465.6	245.2	150.4	86.9	55.3	34.3	15.6	7.5	4.1
$\pm$	114.7	27.5	18.4	13.5	10.2	8.0	6.0	4.1	3.0	2.4

Table 5.7: *Corrections to the raw neutrino NC sample for the w bins $[w_0 - 0.05; w_0]$: background (b/g) subtraction and helicity unfolding.*

w_0 :	0.05	0.10	0.15	0.20	0.25	0.30	0.35	0.40	0.45	0.50
silent NC	1087.9	257.8	152.4	74.5	47.9	33.7	19.1	14.9	6.4	3.1
$\pm$	33.3	16.2	12.5	8.7	7.0	5.9	4.4	3.9	2.6	1.8
noisy NC	199.4	41.2	15.3	15.3	9.1	5.4	1.4	2.6	0.0	0.0
$\pm$	18.9	7.6	4.5	4.5	3.5	2.6	1.4	1.9	0.0	0.0
calm HA	-25.6	-11.1	-2.6	-1.7	-0.5	-0.8	-0.3	-0.3	-0.2	-0.1
$\pm$	9.2	4.0	0.9	0.6	0.2	0.3	0.1	0.1	0.1	0.1
unclassified	146.3	47.0	23.5	10.0	8.3	6.0	0.8	1.8	2.5	0.8
$\pm$	30.8	10.6	5.7	2.8	2.5	1.9	0.5	0.9	1.1	0.5
EMI-ϵ_{elec} : CC	-227.1	-8.9	-0.6	-1.0	-0.1	-0.0	-0.0	-0.0	-0.0	-0.0
$\pm$	40.5	1.5	0.2	0.4	0.1	0.0	0.0	0.0	0.0	0.0
EMI-ϵ_{geo} : CC	-116.1	-12.0	-2.8	-2.3	-0.2	-0.0	-0.1	-0.1	-0.0	-0.0
$\pm$	26.8	2.4	0.6	0.5	0.1	0.0	0.1	0.1	0.0	0.0
$\lvert\vec{p}\rvert_\mu < 3$: CC	-304.2	-20.1	-2.7	-1.2	-0.0	-0.0	-0.0	-0.0	-0.0	-0.0
$\pm$	36.1	2.2	0.3	0.2	0.0	0.0	0.0	0.0	0.0	0.0
b/g-subtr. NC	760.6	293.9	182.5	93.6	64.5	44.3	21.3	18.9	8.7	3.7
$\pm$	78.5	21.5	14.5	10.2	8.2	6.7	4.6	4.5	2.9	1.9
wrong helicity	-190.4	-74.1	-39.1	-23.8	-13.8	-8.8	-5.4	-2.6	-1.2	-0.7
$\pm$	23.0	11.3	7.4	5.5	4.0	3.1	2.4	1.6	1.1	0.7
$\overline{\nu}_e$ background	-75.5	-5.3	-1.9	-1.1	-0.6	-0.4	-0.2	-0.2	-0.1	-0.0
$\pm$	12.4	0.9	0.3	0.2	0.1	0.1	0.1	0.1	0.1	0.0
pure $\overline{\nu}_\mu$ NC	494.7	214.5	141.5	68.7	50.1	35.1	15.7	16.1	7.4	3.0
$\pm$	82.7	24.3	16.3	11.6	9.1	7.4	5.2	4.8	3.1	2.0

Table 5.8: *Corrections to the raw antineutrino NC sample for the w bins $[w_0 - 0.05; w_0]$: background (b/g) subtraction and helicity unfolding.*

The observed NC events were split into the 'silent' part, for which $F_v = 1$, and a 'calm' part, for NC events with $10^{-}2 \leq F_v < 1$. In this way it is visible that the major part of the NC class are in fact silent events, for which the misidentification from HA is very small. In the analysis, we excluded events which did not balance charge (hadronic system with overall charge +1 for NC), since they must contain badly measured tracks and their inclusion would unphysically distort a distribution in any kinematical variable. This subtracted UB=41(28) events in the (anti)neutrino case. The silent NC sample w distribution was then scaled by the ratio $NC_{sil}/(NC_{sil} - UB)$, and the corrected event numbers are displayed in the first row. The second row in the tables consists to about 80% of observed (raw) events, since we added a correction for the noisy NC, that was 27.6% (23.6%) in magnitude relative to the calm NC events.

The main correction arises from the misidentified CC events, as expected. More than 95% of those enter the first w bin, except for the geometrical EMI acceptance correction, which is harder in w than the other two. This is due to the fact that events with large angle muons are more likely to be lost and thus acquire a large weight, while on the other hand they are obviously biased towards larger $w = p_L(p_T/p_L)^2/2M_N$ values. The largest single correction considers the low momentum muon CC events, where the relative size of the correction is larger in the neutrino than in the antineutrino case. This is expected because of the helicity structure of the neutral current which leads to fewer slow muons for the antineutrino sample - there most events have small $y_{(Bj)}$ values, i.e. the fractional energy transfer to the nucleon tends to be small, leaving mainly fast muons. This effect of course has to be folded with the energy spectrum of the beam, and is hence not as marked as one might conclude from the $y_{(Bj)}$ distributions alone.

In the antineutrino case, the wrong helicity contamination is another sizeable correction, since the abundance of positive hadrons cannot be surpressed sufficiently by the magnetic horns. The electron neutrino contamination is dominated by ν_e CC events, hence the w distribution of the correction follows closely the shape of the misidentified CC corrections.

5.4.7 Correction for the Experimental Resolution in w

The ability to measure w depends on the correct determination of the ratio of transverse to longitudinal hadronic momentum, p_T/p_L, as well as on a reasonable resolution for the absolute p_T. Here we are going to show the quality of resolution in w as determined from Monte Carlo studies in which the true w value is compared with the one obtained from a full simulation of the detector performance. We are mainly affected by losses of neutral hadrons, n, π^0, K_L^0, that tend to lead to an underestimation of the hadronic three-momentum. This is due to the meagre spread around the total shower direction of the individual hadrons.

The Monte Carlo Method chosen to determine the corrections to the data was the LUND Monte Carlo Program (LMC) [47]. The LMC uses the Quark Parton Model (QPM) for the initial scattering process and the Lund fragmentation scheme [61] for the subsequent quark hadronization. This model has been employed previously by this experiment [62] and in general agrees with our data, for the appropriate kinematical region where the hadronic invariant mass is sufficiently large, $W^2 \geq 2.5GeV^2/c^2$. When comparisons between the LMC and real data are made, the LMC sample was obtained by the application of cuts identical to those used to define the real data sample. Special care has to be taken about the fact that not only the relative shape of the w distributions changes, but also the total size of the sample, due to the adjustment of a cut in visible variables to a cut in true variables.

This is a change in addition to the variation of the sample size with different chosen cut values. We thus analysed an identical Monte Carlo sample twice, once for the cuts on visible variables and once for the cuts on their true values.

Experimental biases resulting from non-identification of (neutral) particles and measurement errors were included. With the exeption of the parameters E_{min} and s/u (see below) all parameters of the LUND model were set to their default values. In particular, the value for the probability that a meson has spin 1 was 0.5, and the value for the width of the Gaussian p_x and p_y distributions for primary hadrons was 0.44 GeV/c (p_x and p_y are the components of the transverse momentum perpendicular to the original quark direction). The parameters E_{min}, the minimum energy at which the creation of quark-antiquark pairs is terminated, and s/u, the ratio of $s\bar{s}$ and $u\bar{u}$ pairs created in the fragmentation of chain, were changed from the default values of 1 GeV and 0.3 to 0.2 GeV and 0.21 respectively, in order to reproduce the observed x_F spectra of the charged hadrons and the measured K^0/(charged π ratio in the current fragmentation region. With these parameters the measured average charged multiplicity $< n_{ch} >$ as a function of the hadronic mass W, and the p_{Lab} distribution of the identified protons were also approximately reproduced by the Monte Carlo events, both for νp and $\overline{\nu}p$ scattering. These comparisons were made using 'modified' Monte Carlo events: in order to allow for the experimental biases the initial Monte Carlo events were modified according to the experimental situation. The momenta of the generated charged particles were smeared within the measuring errors, unidentifiable charged particles were assigned the pion mass and undetectable neutral particles were removed.

The LMC has been extensively tested [71] for the description of the NC channel and was found to represent the data well. We emphasise that it has not been 'tuned' to reproduce the observed w distributions, so that the agreement be-

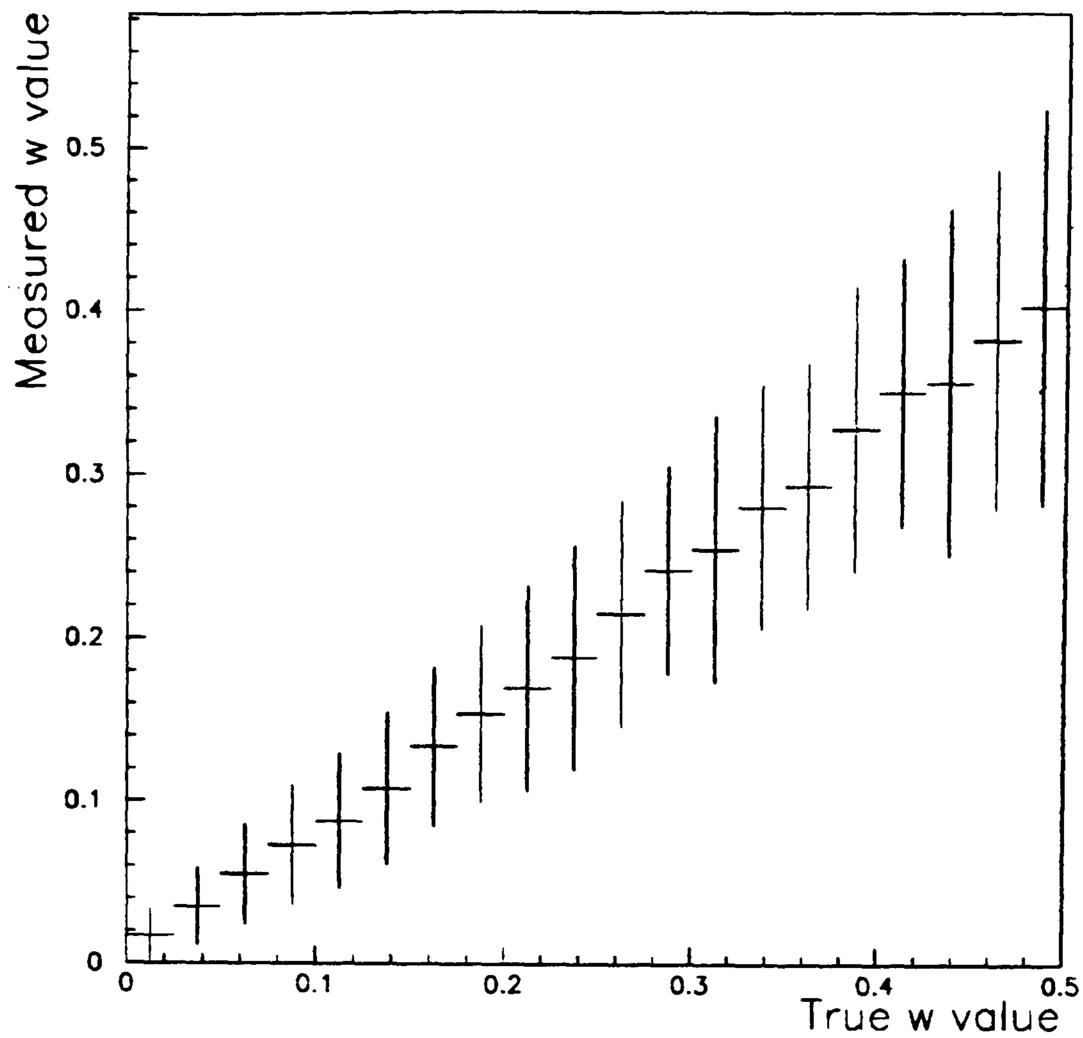

Figure 5.6: Mean of the distributions in the measured w for a fixed bin of the true w. The errors shown are *NOT* the errors on this mean, which are much smaller, but represent the spread of the conditional distributions. LUND neutrino sample.

tween the measured and the simulated data shown below is a non-trivial indication that the main biases have been understood and correctly treated. The reason of the Monte Carlo correction factors differing from unity is mainly an experimental underestimation of the event p_T, so that the correction will not be dependent on the detailed fragmentation model, because any reasonable simulation has to reproduce the basic distributions in the event p_T and p_L of the hadronic system. This is of course only a necessary and not a sufficient condition for an agreement between measured and simulated w distributions.

In figure 5.6 we show the means and standard deviations of the conditional distributions in the reconstructed w values, in dependence on the true value of w. To obtain errors on the means, the errors shown would have to be scaled by the inverse of the square root of the bin content. However, they have no physical meaning since they can be made arbitrarily small by increasing the size of the simulated sample.

The relevant information is rather contained in the standard deviations we have shown. For the first few bins the actual resolution is better as the size of the errors shown, since there the w bin size is not small relative to the absolute value of w. The last bins of the true w contain only a few events (the distribution in the true w decreases by more than three orders of magnitude over the range displayed here), thus the errors indicated underestimate the quality of the resolution.

The comparison of the w distributions obtained after subtracting the various backgrounds from the raw NC sample are displayed in figures 5.7, 5.8, 5.9 and 5.10, for the neutrino case (logarithmic and linear scale) and the antineutrino case (logarithmic and linear scale), respectively. We observe fair agreement which shows best on the logarithmic plots for the second half of the distributions, and on the linear plots for the small w bins. The w distributions which have been Monte Carlo-corrected for the effects of resolution and for the cuts $W > 3.0\ GeV/c$, $E_H >$ $7.5\ GeV$ are shown in the next chapter, where they are used as input to the method of chapter 3.

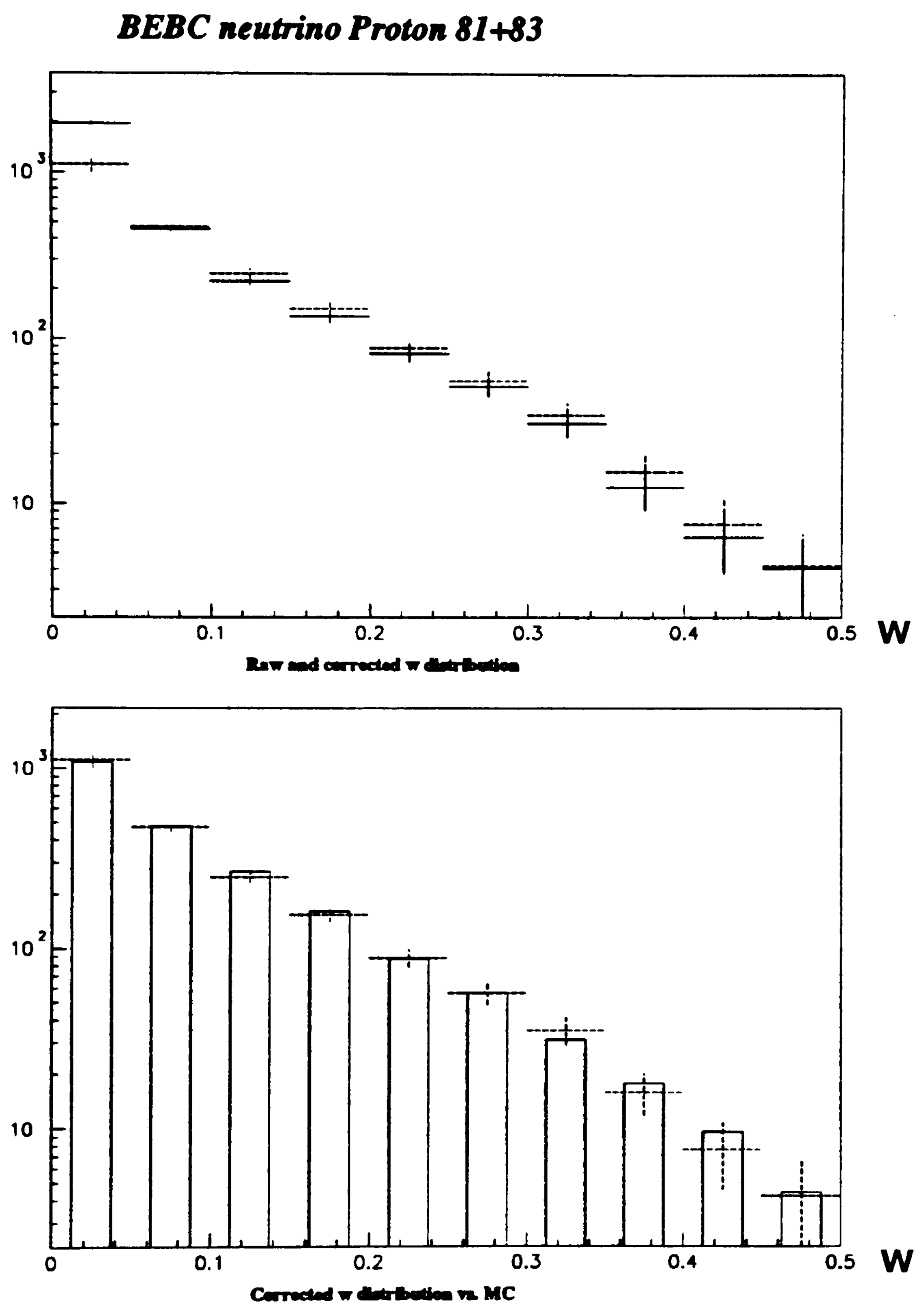

Figure 5.7: Top: Comparison of raw and background-subtracted w distribution for the neutrino NC sample. Bottom: Comparison of this corrected w distribution to the simulated data which is normalised to the measured number of events. Logarithmic scale.

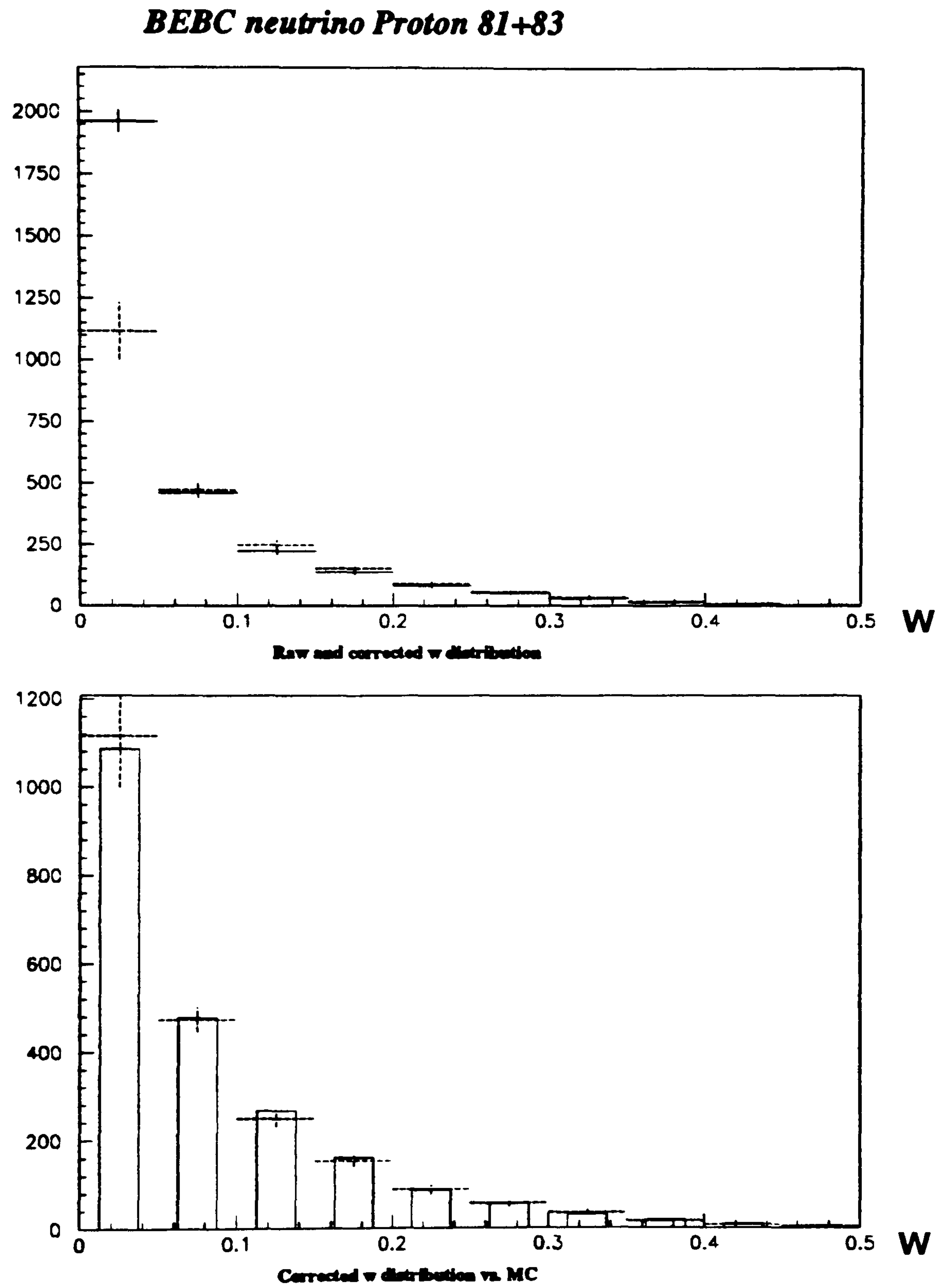

Figure 5.8: Same, linear scale.

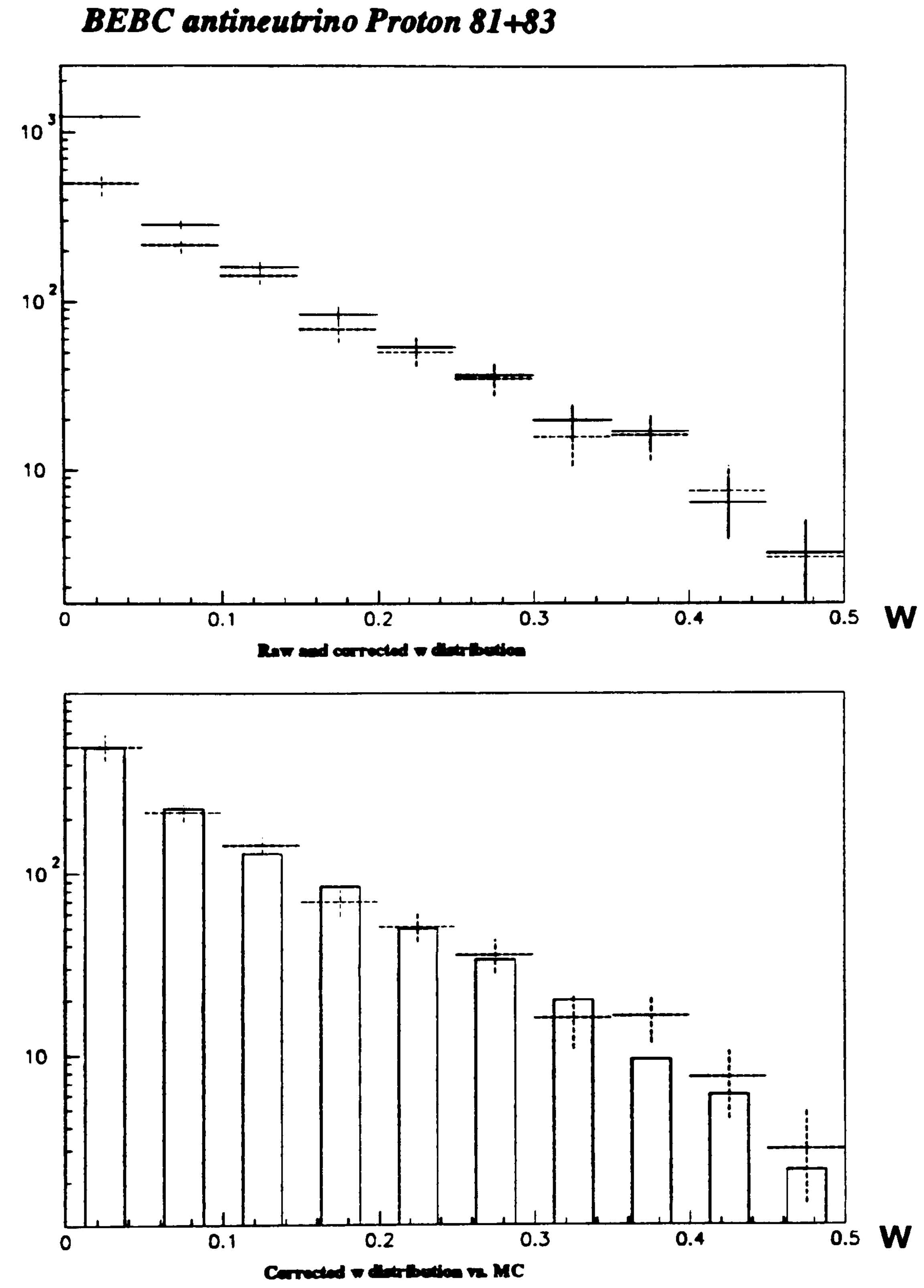

Figure 5.9: Top: Comparison of raw and background-subtracted w distribution for the antineutrino NC sample. Bottom: Comparison of this corrected w distribution to the simulated data which is normalised to the measured number of events. Logarithmic scale.

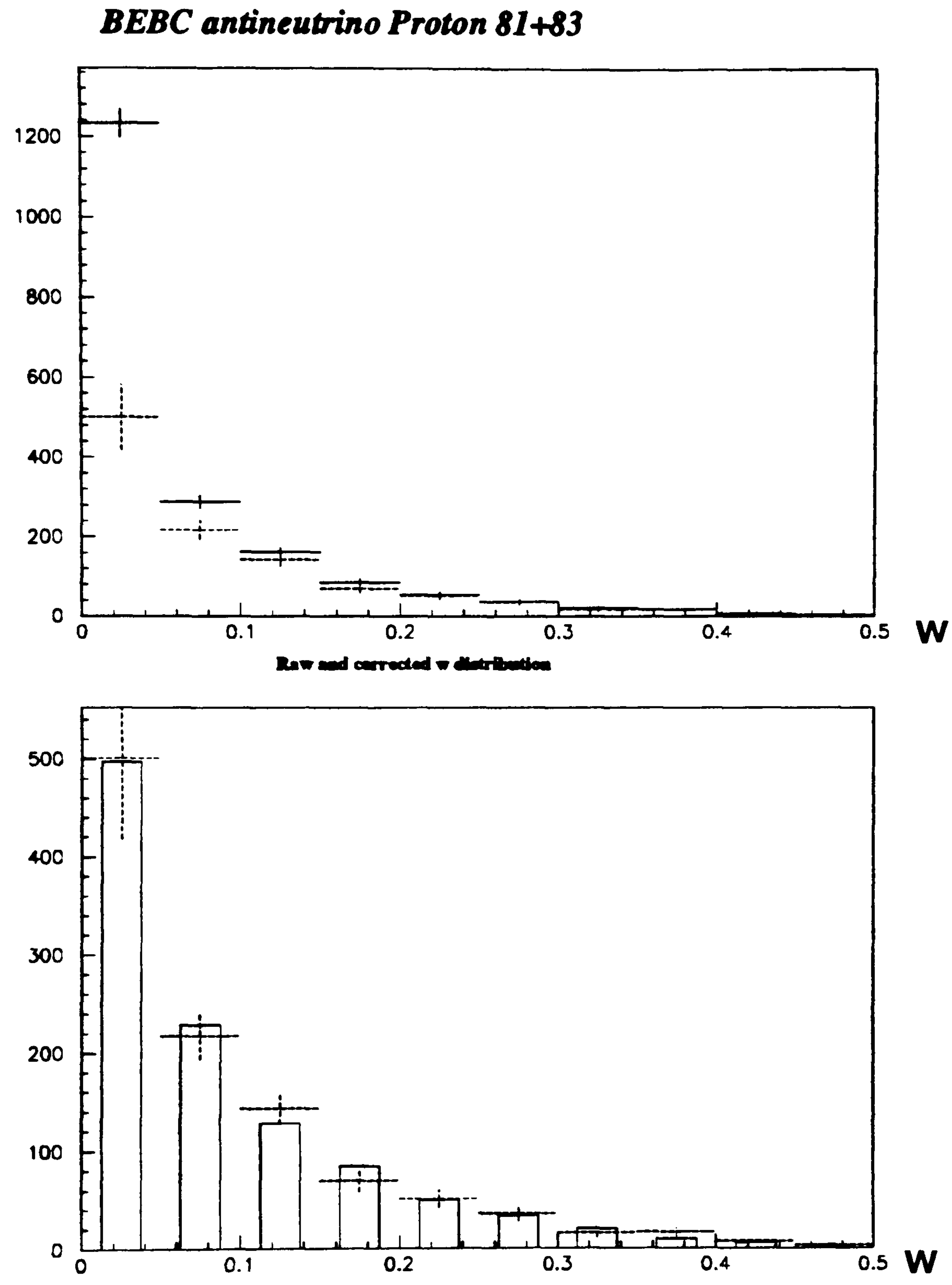

Figure 5.10: Same, linear scale.

Chapter 6

The Proton Structure in NC Interactions

6.1 Introduction

Many of the recent precision experiments performed to test the standard model parameters probe the nucleon via weak and electromagnetic deep inelastic scattering. The extraction of values for $\sin^2\theta_W$, for instance, in those different physical processes relies on the assumption of universal parton distributions in the nucleon. Whereas the charged current structure of the nucleons has been extensively compared to its electromagnetic (EM) structure, surprisingly little is known about how it compares to the neutral current structure, and we have expanded on the experimental reasons for this in chapter 3. Even in the comparison of charged weak and electromagnetic interactions discrepancies of the order of 10% persist for the $x_{(Bj)}$-dependence of the parton distributions and their integrals. Although the precision that can be achieved in neutral current DIS will obviously be a long way behind the one in charged current DIS, it is important to address this more difficult channel that provides us with a new and independent probe of the hadrons. The remarks at the end of chapter 4 already indicated that there can be also advantages in investigating the NC channel, particularly when one is interested in the low $x_{(Bj)}$ region.

So far the existing analyses of the neutral current cross-section dependence on $x_{(Bj)}$ always relied on heavy targets, employing mainly calorimetric techniques to reconstruct the hadronic system (jet). This offers the advantage that also the neutral part of the hadronic shower is included in the event kinematical variables. However, although fine-grained calorimeters have been successfully applied to the problem, the intrinsic difficulty to measure accurately the angle of the shower, related to the complex mechanisms of lateral shower development, remains the major obstacle to an exact assignment of a $x_{(Bj)}$ value for the event. The best shower angle resolution achieved so far is comparable to the angle itself and dominates the resolution in $x_{(Bj)}$, particularly at large shower angles (high p_T) or low shower energies. This arises from the reconstruction of $x_{(Bj)}$ by the measurement of the shower angle and energy, in addition to the incident neutrino energy, via

$$\begin{aligned} x &= w/(1-y) \qquad \text{(in our notation)} \\ &\equiv p_L(p_T/p_L)^2/2M(1-y) \;\approx\; E_H \tan^2\theta_H/2M(1-y), \qquad (6.1) \\ y &= E_H/E_{(\nu)} \end{aligned}$$

To limit the uncertainties due to this source, a cut in the scaling variable $y_{(Bj)}$ is imposed. Nevertheless, small changes in the shower angle resolution translate into fairly large fluctuations in the final $x_{(Bj)}$ distributions.

Since the necessity of determining the neutrino energy on an event by event basis can only be met with a narrow band beam, the targets used are heavy nuclei throughout. One has to be aware then that what is actually measured is the nucleon structure in a nuclear environment, and since the discovery of the EMC effect [74] we know that it is a premature assumption to extrapolate naively from heavy target to free nucleon target physics. This is a distinction of principle and has to be kept in mind when a pragmatic attitude is taken in assuming that the errors of an analysis are larger than any nuclear effect. In the context of neutrino interactions this attitude is usually taken because so far the statistics have not been sufficient to clear the issue of the existence of a nuclear effect in neutrino DIS [73].

6.2 Extraction of the $x_{(Bj)}$ Distributions

In the previous chapter we isolated the neutral current w distributions, after subtracting the neutron background with the help of the IPF detector information and after correcting for the other contaminations, of which the most sizeable has been due to charged current events where the muon escaped detection. After resolution effects have been removed with the help of a Monte Carlo simulation, we arrived at fully corrected w distributions for the neutrino and antineutrino case.

Here we intend to apply the method developed in chapter 3 to use these w distributions for the extraction of the $x_{(Bj)}$ dependence of the cross-section. This application of the method will yield information about the NC cross-section dependence on $x_{(Bj)}$ for free protons, for the first time. It also is the first such investigation that is carried out with a target that is not (approximately) isoscalar, unlike in all heavy target experiments.

We display in figures 6.1, 6.2 the corrected w distributions $G(w)$ for the neutrino and antineutrino sample, respectively, before and after the the Monte Carlo correction for the effects of the kinematical cuts, $E_H > 7.5GeV$ and $W^2 > 3.0GeV^2/c^2$ (true values), and for the resolution in w are made. The solid line is the result of a fit to the parametrisation

$$G(w) = cst\ (w_{max} - w)^{\lambda}\ (\ln \frac{1}{w})^{\delta} \tag{6.2}$$

which was explained in chapter 3. We shall comment on the use of other parametrisations in due course. Again, this logarithmic form for $G(w)$ is the one for which the fit parameters have the larger errors, so that we chose the function that is least

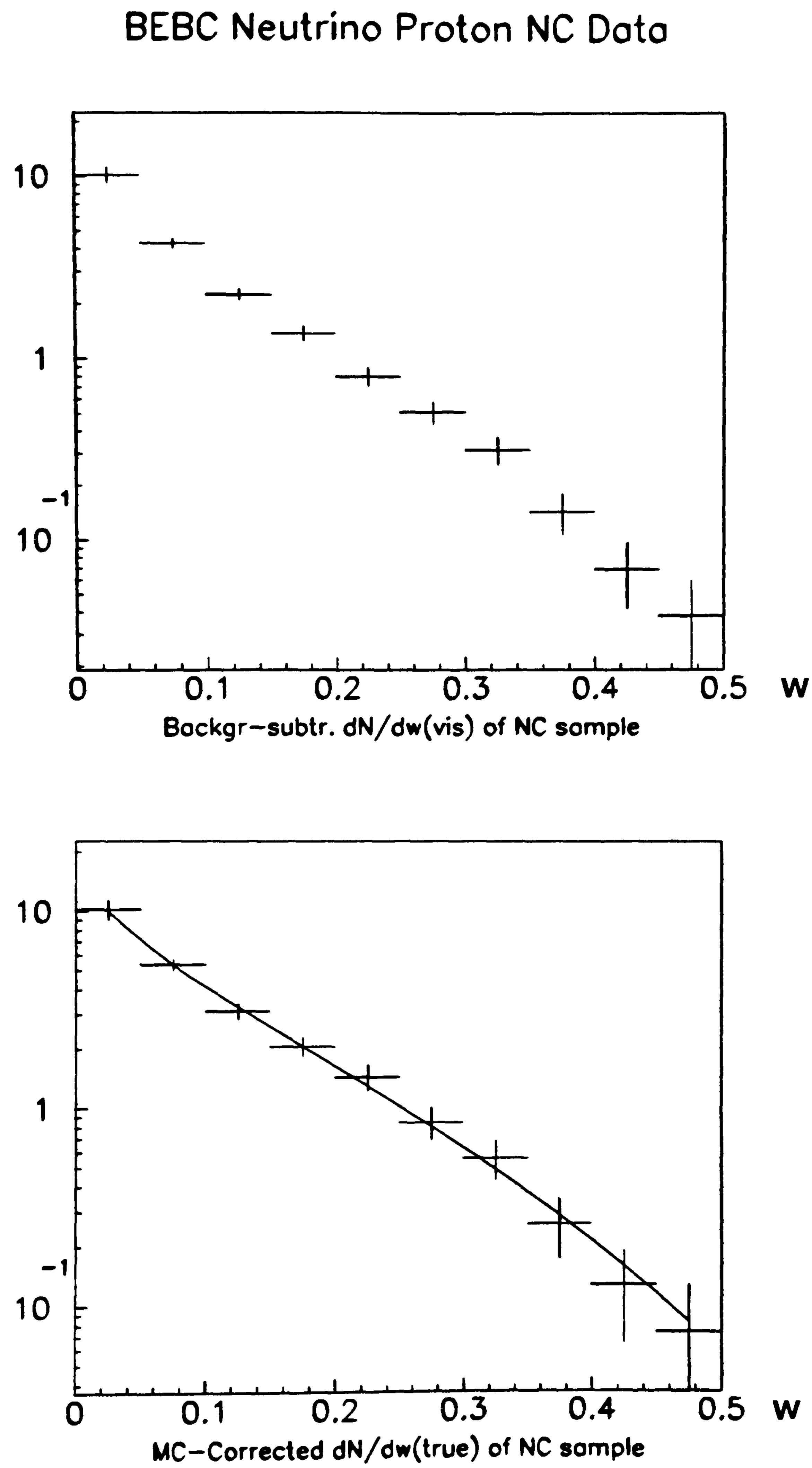

Figure 6.1: *Neutrino w distribution before and after Monte Carlo correction, fit to the parametrisation as explained in the text*

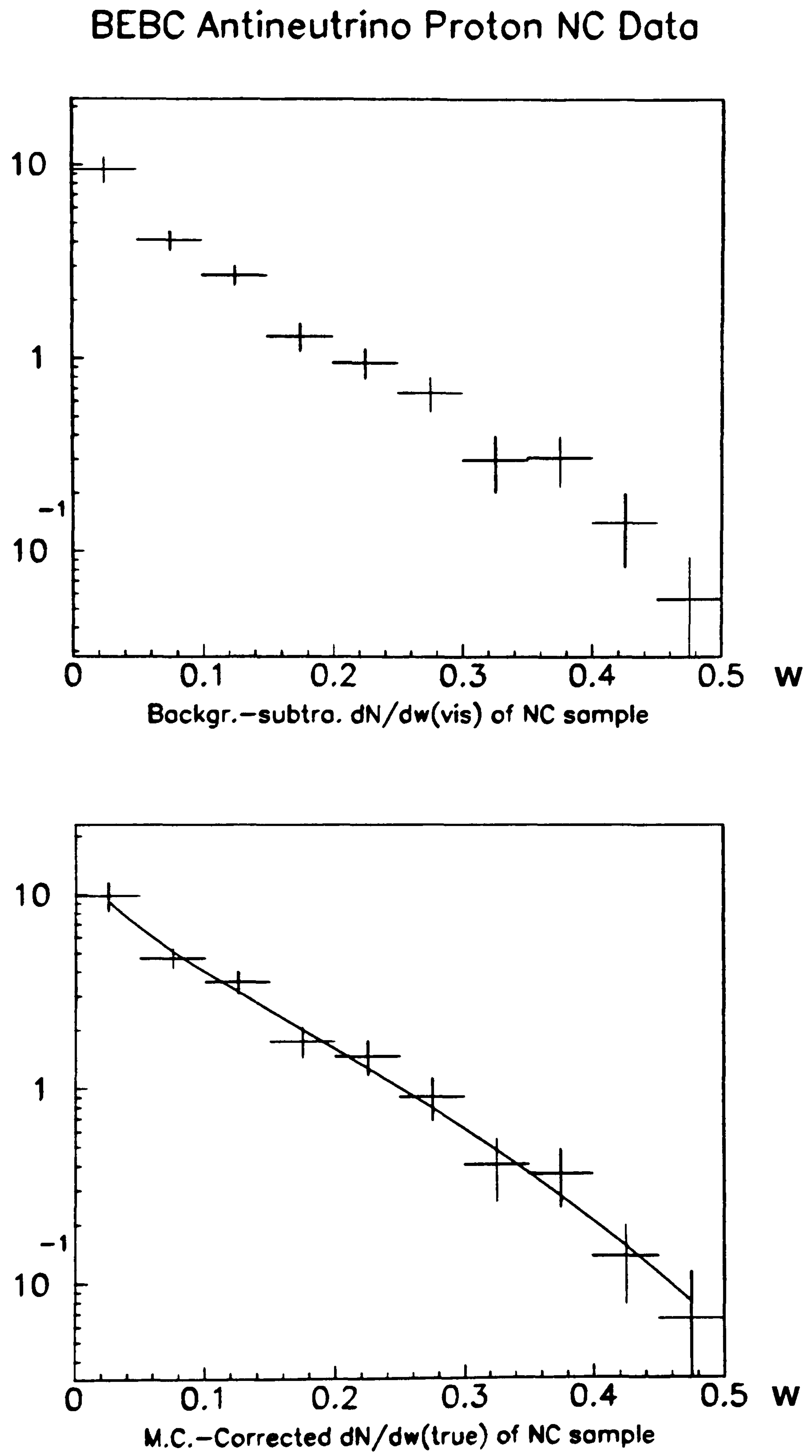

Figure 6.2: *Antineutrino w distribution before and after Monte Carlo correction, fit to the parametrisation as explained in the text*

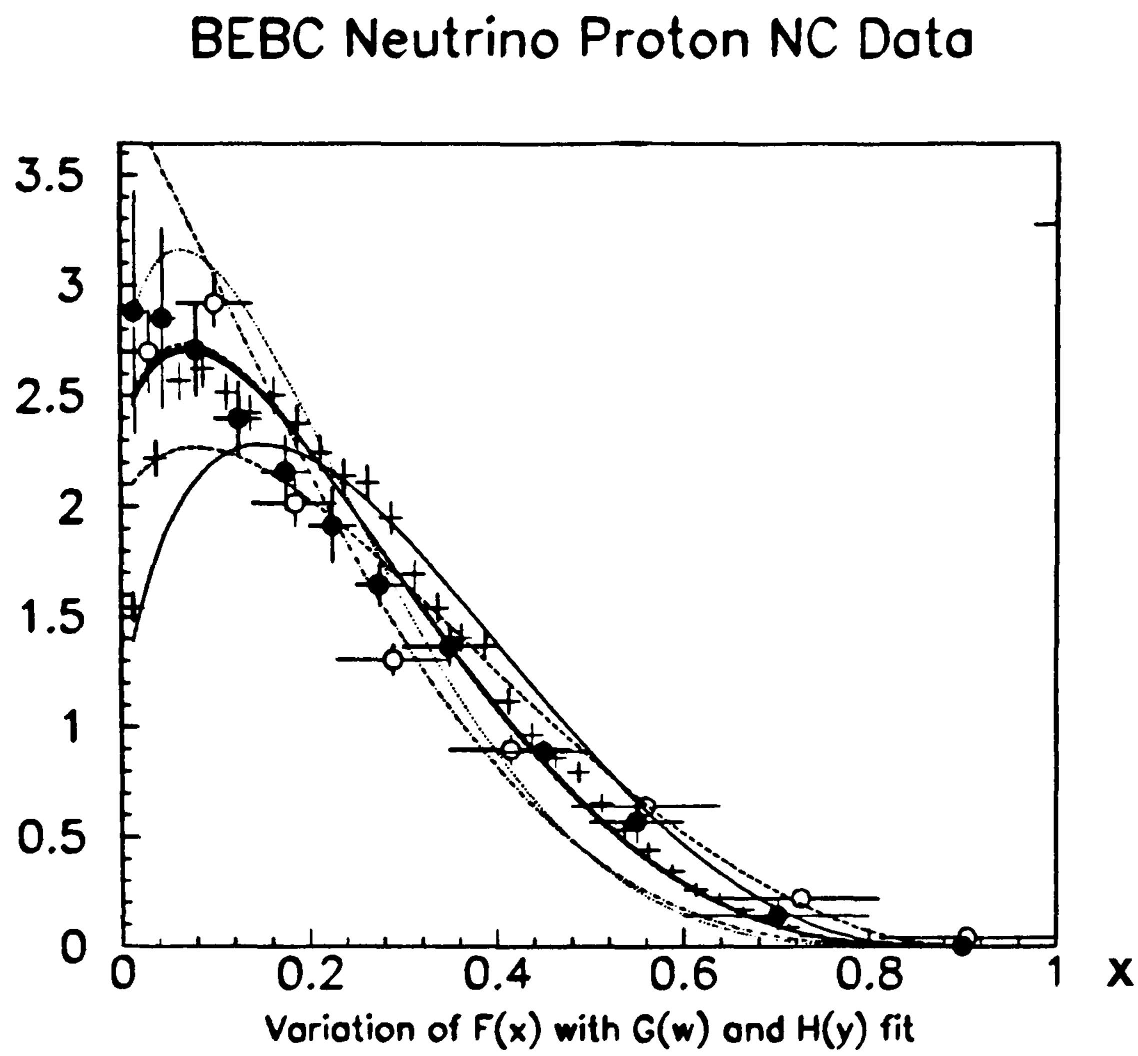

Figure 6.3: *Marginal $x_{(Bj)}$ distribution of the neutrino NC cross section and its variation with fit parameters.*

well constrained by the data, to obtain conservative estimates for the errors on the $x_{(Bj)}$ distributions. The value of w_{max} is determined through the maximum beam energy, and for a bound of 400 GeV we have to use $w_{max} = 0.80$. It was checked that the results we shall present are very weakly dependent on the exact value chosen, and we obtained all results also for the w_{max} values corresponding to lower beam energy bounds. However, even for a maximum beam energy of 240 GeV, w_{max} only decreases to 0.75. The parameters obtained were:

$$\nu: \ \lambda \pm \sigma(\lambda) = 3.47 \pm 0.89, \quad \delta \pm \sigma(\delta) = 1.12 \pm 0.39 \quad \text{and} \quad \chi^2/N_{DF} = 0.23 \tag{6.3}$$

$$\bar{\nu}: \ \lambda \pm \sigma(\lambda) = 3.65 \pm 1.18, \quad \delta \pm \sigma(\delta) = 0.99 \pm 0.55 \quad \text{and} \quad \chi^2/N_{DF} = 0.52 \tag{6.4}$$

The two-parameter fits describe the data well and are sufficiently 'elastic' to represent all its discernible features. Together with the $y_{(Bj)}$ distributions we presented in chapter 3, obtained within the cuts from the Monte Carlo, we have now all the infor-

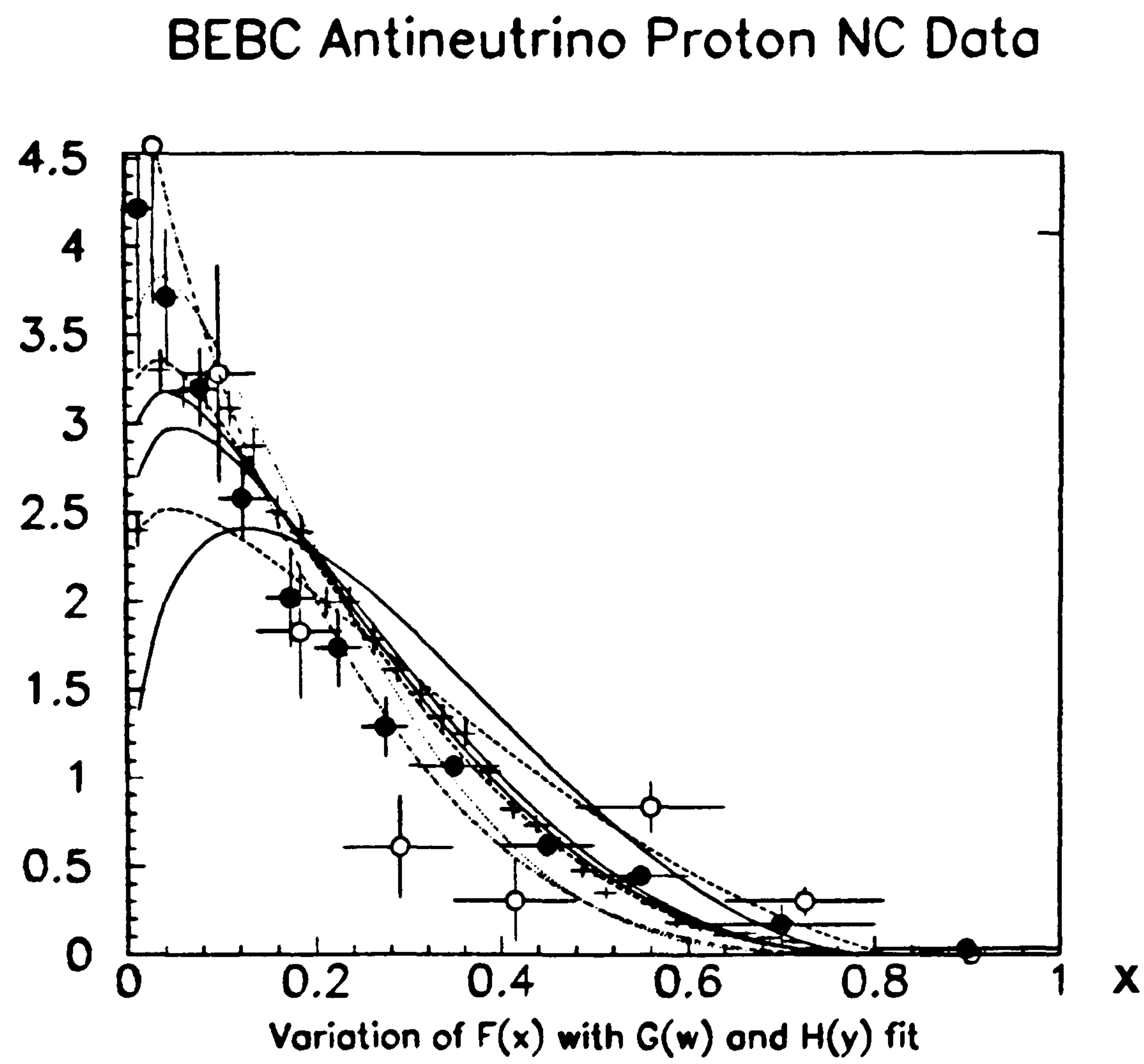

Figure 6.4: *Marginal $x_{(Bj)}$ distribution of the antineutrino NC cross section and its variation with fit parameters.*

mation at hand to calculate the $x_{(Bj)}$-dependence $F(x)$ of the cross-section. Figures 6.3, 6.4 show the solutions, equations (3.16) and (3.22), of the integral equations in chapter 3. The central (solid) line gives $F(x)$ for the central parameters of the fits to $G(w)$ and $H(y)$, the two lines (full and dashed) very close to it represent the variation with the slope parameter(s) of $H(y)$, and the two outer pairs of lines give the variation with the parameters of $G(w)$, due to $\pm\sigma_\lambda$ (dashed and dotted) and $\pm\sigma_\delta$ (dash-dotted and full), respectively. The points with error bars are the simulated $x_{(Bj)}$ distributions from a Monte Carlo sample of size of about an order of magnitude larger than the data sample. The full (open) circles are the data of the two measurements by the CHARM (FMM) experiments that we are going to explain in section 6.4, and the error bars indicate the statistical errors only.

The errors on the extracted $F(x)$ that we display through the above deviations include the statistical *and* systematic uncertainties of the data on $G(w)$ that were propagated to the fully subtracted $G(w)$ and then to the Monte Carlo corrected w distribution. Within these errors the measured and the simulated w distribution are seen to agree. The uncertainty in δ that arises mainly from the first half of the measured w region is in turn responsible for the uncertainty of $F(x)$ towards small $x_{(Bj)}$ values, and the same holds for λ and the second half of the w and $x_{(Bj)}$ regions. Strictly speaking we must be aware that we have assumed that the w distributions above $w = 0.5$ behave smoothly and follow the shape we extracted from the measured region $w < 0.5$. However, in Monte Carlo studies we observe no change in the behaviour of $G(w)$ as its argument approaches w_{max}, and on kinematical grounds it is anyhow expected that it must fall to zero with some power law. For $x > 0.5$ the uncertainty in $F(x)$ becomes comparable to the values of $F(x)$ itself, so that the implicit extrapolation can be safely regarded as justifiable within the errors. We checked that simultaneous variations of the $G(w)$ parameters, which are not independent, do not give rise to much larger uncertainties than the ones displayed. Therefore we chose to keep the individual variations with $\pm\sigma(\lambda)$ and $\pm\sigma(\delta)$ due to their lucid interpretation from above.

The remaining uncertainties arise from the exact 'choice' of w_{max}, the Monte Carlo correction and the parametrisation of $G(w)$. Their influence was estimated by changing the respective values and choosing alternative functional forms for the w distribution. The value of w_{max} was changed by $\pm$ 5%, and the Monte Carlo factors $f_{MC} = 1 + c_{MC}$ were altered to represent a worse resolution in w, by systematically increasing the c_{MC} by 20% . We employed an exponential fit, finite at the origin, and the power law

$$G(w) = cst \; (w_{max} - w)^{\lambda} \; / \; w^{\delta} \tag{6.5}$$

which is more strongly diverging for $w \to 0$ than (6.2). Each of these systematic

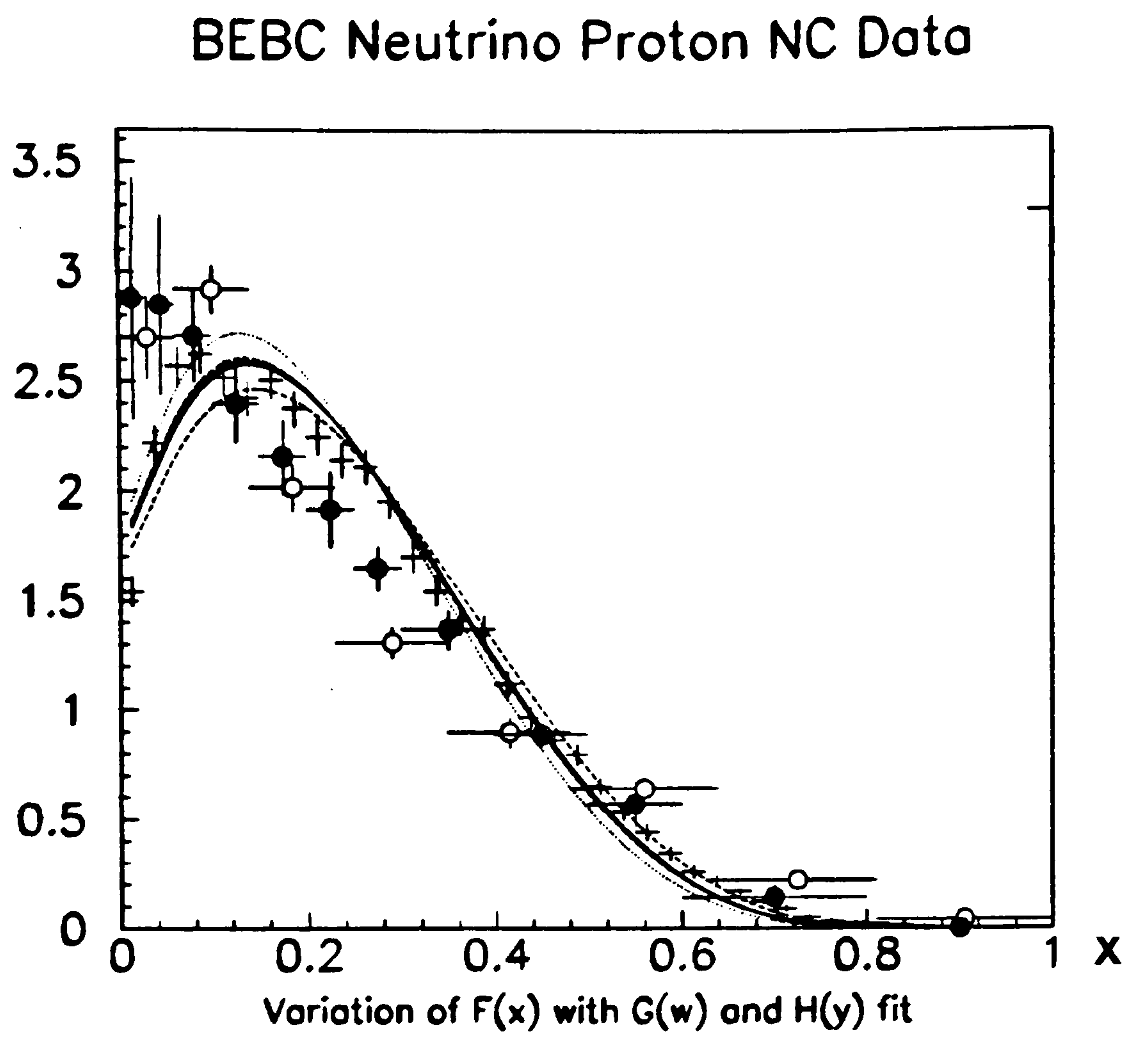

Figure 6.5: *Neutrino NC $x_{(Bj)}$ distribution using a power law for $G(w)$*

effects was found to be smaller than the variations of $F(x)$ with respect to the parameters describing $G(w)$. The relatively largest deviation occurs for the region $w \rightarrow 0$ when we parametrise $G(w)$ by different functions. Therefore we discuss these variations in more detail below. We note that we have extracted the $x_{(Bj)}$ distribution without the use of any model or any assumed parton distribution functions, and thus no systematic errors arise due to variation of any model parameters.

Figure 6.5 shows the $x_{(Bj)}$ distribution from this power law, where the parameter δ has been fixed to a value of 0.175 ± 0.015, so that this is a one-parameter fit. From Monte Carlo studies we can infer that the data does not constrain δ to values which represent a physically sensible divergent behaviour near zero. This expected effect has to do with the fact that (6.5) changes its slope dramatically in the first bin, below the bin center. Thus we cannot expect the value of the measured and binned $G(w)$ at this center to be representative for the actual value of the w distri-

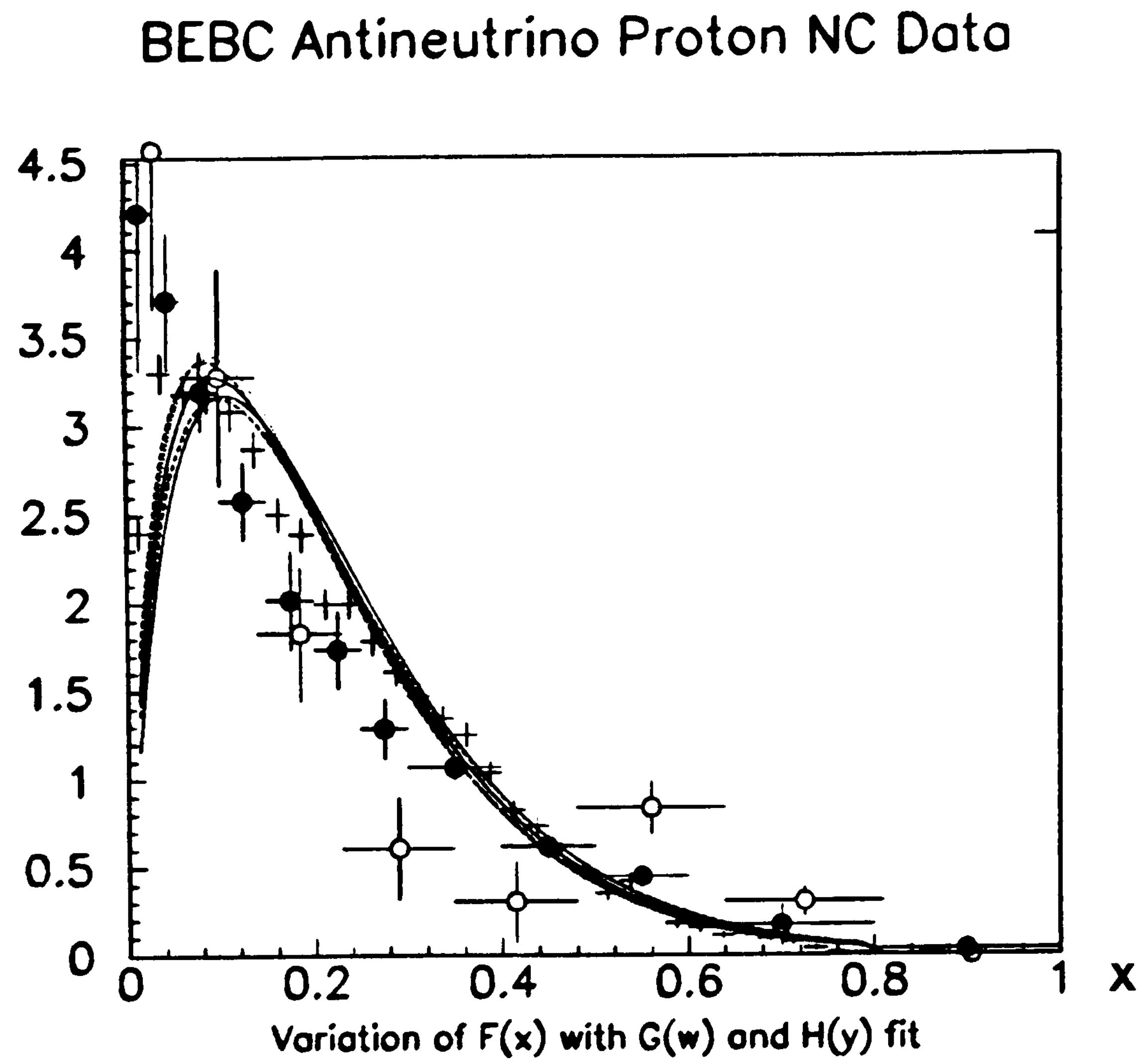

Figure 6.6: *Antineutrino NC $x_{(Bj)}$ distribution using an exponential for $G(w)$*

bution, but rather for its integral over the first bin. This distinction is pronounced enough for a chosen form (6.5) while it is marginal and could be absorbed into the errors for the parametrisation using (6.2). The latter showed us that we can extract a slope for $w \to 0$ from the measured data, even for a diverging function in the fit, and the purpose of using (6.5) is rather to display the stability of the result against the use of a different (more strongly diverging) parametrisation. We observe further that the resulting $x_{(Bj)}$ distribution is stable within the errors against the exchange of (6.2) by a simple exponential fit, that is finite at the origin. This proves that we are not imposing a priori information, while parametrising the w distributions, that could preselect a pronounced feature of the $x_{(Bj)}$ distributions. It is in line with our procedure of merely representing the shape of the observed w distribution by some convenient smooth function.

The BEBC hydrogen collaboration WA21, this experiment, has measured

[77] the proton structure functions and found them well described by the LUND Monte Carlo. The agreement between the NC $x_{(Bj)}$ distributions extracted here and the simulated ones indicates that we see no evidence for a different proton structure in NC and CC interactions. The same consistency was found by the two groups whose data is compared to ours in section 6.4. Our result confirms the concept of parton universality in NC and CC interactions for the first time for neutrino and antineutrino scattering off a free proton.

6.3 Normalisation to the Total Cross-sections

So far we have normalised the extracted $x_{(Bj)}$ distributions to unity, or equivalently, to the total number of corrected events. In order to obtain a physically meaningful absolute scale, we calculate here the total cross section from the known flux shape [38]. The determination of an absolute normalisation of the total flux of neutrinos into the detector is difficult for a wide-band beam. We shall proceed in the same way as was done for the absolute cross section for the CC channel, published in [78], and apply identical selection criteria, different from the ones used in chapter 5 for the NC analysis. We first normalise the known beam flux shape using the observed corrected number of right helicity (anti)neutrino CC events and the published cross section slopes for hydrogen, for identical selection criteria and beam energy interval $20 < E < 300\ GeV$. The slopes were obtained from the cross section ratios for hydrogen *relative* to neon that were determined with the same detector and beam conditions, and from the isoscalar-corrected *absolute* cross sections in neon which were taken from a (revised) measurement in the narrow-band beam at CERN [79].

We can write for the observed and expected number of CC events

$$N^{CC} \approx \ < N^{CC} > \ = \int dE\ n_P \sigma^{expt}(E) \Phi(E) \tag{6.6}$$

Beam Energy Interval $\Delta E/GeV$	ν Flux $[\Delta E \cdot \phi(E)]/m^{-2}$ per muon in gap 2	$\bar{\nu}$ Flux $[\Delta E \cdot \phi(E)]/m^{-2}$ per muon in gap 2
0-5	$0.130 \cdot 10^{-1}$	$0.258 \cdot 10^{-1}$
5-10	$0.261 \cdot 10^{-1}$	$0.515 \cdot 10^{-1}$
10-15	$0.513 \cdot 10^{-1}$	$1.010 \cdot 10^{-1}$
15-20	$0.375 \cdot 10^{-1}$	$0.728 \cdot 10^{-1}$
20-25	$0.388 \cdot 10^{-1}$	$0.534 \cdot 10^{-1}$
25-30	$0.267 \cdot 10^{-1}$	$0.341 \cdot 10^{-1}$
30-40	$0.337 \cdot 10^{-1}$	$0.362 \cdot 10^{-1}$
40-50	$0.169 \cdot 10^{-1}$	$0.158 \cdot 10^{-1}$
50-60	$0.102 \cdot 10^{-1}$	$0.816 \cdot 10^{-2}$
60-70	$0.629 \cdot 10^{-2}$	$0.444 \cdot 10^{-2}$
70-80	$0.526 \cdot 10^{-2}$	$0.326 \cdot 10^{-2}$
80-90	$0.413 \cdot 10^{-2}$	$0.219 \cdot 10^{-2}$
90-100	$0.340 \cdot 10^{-2}$	$0.156 \cdot 10^{-2}$
100-120	$0.451 \cdot 10^{-2}$	$0.170 \cdot 10^{-2}$
120-140	$0.240 \cdot 10^{-2}$	$0.702 \cdot 10^{-3}$
140-160	$0.121 \cdot 10^{-2}$	$0.271 \cdot 10^{-3}$
160-180	$0.575 \cdot 10^{-3}$	$0.993 \cdot 10^{-4}$
180-200	$0.288 \cdot 10^{-3}$	$0.354 \cdot 10^{-4}$
200-220	$0.142 \cdot 10^{-3}$	$0.112 \cdot 10^{-4}$
220-240	$0.663 \cdot 10^{-4}$	$0.304 \cdot 10^{-5}$
240-260	$0.319 \cdot 10^{-4}$	$0.737 \cdot 10^{-6}$
260-280	$0.121 \cdot 10^{-4}$	$0.123 \cdot 10^{-6}$
280-300	$0.277 \cdot 10^{-5}$	$0.900 \cdot 10^{-8}$
$0 < E < 300$:		
$\sum [\Delta E \cdot \phi(E)]$	$2.830 \cdot 10^{-1}$	$4.130 \cdot 10^{-1}$
$\sum [E\, \Delta E \cdot \phi(E)]$	8.56	8.75
$20 < E < 300$:		
$\sum [\Delta E \cdot \phi(E)]$	$1.550 \cdot 10^{-1}$	$1.620 \cdot 10^{-1}$
$\sum [E\, \Delta E \cdot \phi(E)]$	7.09	5.78

Table 6.1: *Flux shape for neutrino and antineutrino beam, per muon crossing the beam monitoring system in gap 2, per m^2.*

respectively, where $\Phi(E) = c_\phi \phi(E)$ is the integrated luminosity as a function of the beam energy E, with dimension $m^{-2}GeV^{-1}$, n_P is the number of protons in the target, and the values of $\Delta E \cdot \phi(E)$ are given in table 6.1. For the measured cross section $\sigma^{expt}(E)$ *per proton* we have

$$\sigma^{expt}(E) = \sigma_0^{expt} \cdot E \tag{6.7}$$

with a constant σ_0^{expt}. No significant dependence on E was found for σ_0^{expt}. Thus the proportionality factor can be calculated from the seen CC event number and the measured cross section slope, both evaluated for the same kinematical region, where the beam energy lies between $20 < E < 300$ GeV, via

$$c_\phi n_P = \frac{N^{CC}}{\sigma_0^{expt}} \left(\int_{20}^{300} dE \; E \cdot \phi(E) \right)^{-1} \tag{6.8}$$

Details about the selections of CC events were as in [78], i.e. muons of the correct charge were required to have a momentum of at least 5 GeV and originate from a vertex in the overlap of the fiducial volumes of the hydrogen and the neon collaborations. Corrections for scanning efficiency, EMI acceptance, NC background to the CC class, and low momentum muons have been calculated and found consistent with the published values. The beam energy was estimated with a transverse momentum balance method that uses the p_T of the muon and charged hadron jet averaged over the sample of events with 3 or more prongs:

$$E^{est} = p_L^\mu + \frac{< p_T^\mu >}{< p_T^{CH} >} \, p_L^{CH} \tag{6.9}$$

On integrating $\Phi(E) = c_\phi \phi(E)$ one obtains the total flux Φ'_{tot}, of (anti)neutrinos with energies between 20 and 300 GeV, and it follows that Φ'_{tot} is the ratio N^{CC}/σ_0 divided by the average beam energy $< E >_{\Phi'} \neq < E >_{CC}$ (the former is $E^{(2)}/E^{(1)}$ whereas the latter is $E^{(1)}/E^{(0)}$, where $E^{(n)} \equiv \int_{20}^{300} dE \; E^n \cdot E\phi(E)$). We obtained an average beam energy of 45.8 (35.7) GeV in the (anti)neutrino case, from the unnormalised flux values. The published cross section slopes in hydrogen are

$$\sigma_0(\nu) = (0.474 \pm 0.029) \cdot 10^{-38}\ cm^2/GeV \tag{6.10}$$

$$\sigma_0(\overline{\nu}) = (0.500 \pm 0.032) \cdot 10^{-38}\ cm^2/GeV \tag{6.11}$$

In the data sample we found 6943.3 (6437.9) events after all corrections, where the 1-prong fraction in the antineutrino sample is 22.5% [64]. Thus the proportionality constant as determined from the CC channel is

$$\nu: \qquad c_\Phi n_P = (2066.0 \pm 233.0) \cdot 10^{38} \tag{6.12}$$

$$\overline{\nu}: \qquad c_\Phi n_P = (2227.6 \pm 367.6) \cdot 10^{38} \tag{6.13}$$

For the NC sample within the cuts $E_H > 7.5 GeV$ and $W_H > 3.0 GeV/c^2$ we observed 2650 (1226) events after all corrections. The flux-averaged cross sections corresponding to the complete wide-band flux is then

$$\nu: \qquad \sigma^{NC} = (4.53 \pm 0.60) \cdot 10^{-38} cm^2 \tag{6.14}$$

$$\overline{\nu}: \qquad \sigma^{NC} = (1.33 \pm 0.26) \cdot 10^{-38} cm^2 \tag{6.15}$$

where we added linearly the statistical and systematic errors which were estimated to be 10% for the neutrino case, and 15% for the antineutrino case to allow for an additional uncertainty due to the one-prong correction.

6.4 Comparison to Results of other Experiments

We now compare the obtained $x_{(Bj)}$ distributions to the results of the two main other experiments that have investigated the NC nucleon structure, namely the CERN-Hamburg-Amsterdam-Rome-Moscow (CHARM) [42], [43] and the Fermilab-MIT-Michigan (FMM) [75] group. Both these heavy target experiments used the unfolding method outlined above to correct for the resolution effects and to regain any fine structure that would be bound to be smeared out. The price one pays for this is that in addition to the sensitivity to a local fine structure that represents a real effect in the data, also the statistical fluctuations are magnified by the unfolding procedure. To control such oscillations either a regularisation or a truncation has to be performed, and CHARM (FMM) chose the former (latter) alternative. In both cases, the measured distribution S in the kinematic variables E_H, θ_H and the radial distance of the event vertex relative to the beam axis, r_v, is compared with an expected distribution $\tilde{S}$ that is expressed [76] as a convolution of a resolution transform R and a hypothetical $x_{(Bj)}$ distribution $F_\pm$, as well as a background distribution S^b, as

$$\begin{aligned} \tilde{S}(E_H,\theta_H,r_v) &= \int dx\ R(E_H,\theta_H,r_v;x)F_\pm(x)\ +\ S^b(E_H,\theta_H,r_v) \qquad (6.16)\\ &\equiv R * F_\pm\ +\ S^b \\ \text{with} \quad \frac{d\sigma}{dx} &\equiv \frac{G_F^2 s}{2\pi}F_\pm(x), \qquad (6.17) \end{aligned}$$

where +(-) refers to the (anti)neutrino case. FMM discretises the integration and works with matrix deconvolutions, so that R represents the resolution in $x_{(Bj)}$ as reconstructed by (6.2). Thus they are able to carry out the comparison directly with the corrected (but smeared) $x_{(Bj)}$ distribution $\tilde{S}(\tilde{x}(E_H,\theta_H,r_v))$, which do show a reasonable behaviour, and indicate that the recontruction of $x_{(Bj)}$ is not meaningless, despite the large uncertainties we commented on above. This is not automatically to be expected, since in principle the observed smeared $x_{(Bj)}$ distribution can extend to unphysical values, for instance $x > 1$.

The calculation of the resolution transform R is done with a full Monte Carlo simulation of the beam, detector, data selection, and has to correct for target non-isoscalarity, radiative corrections, and charm production. At the same step the $x_{(Bj)}$ distributions are implicitly corrected for their Q^2-dependence, choosing a power law $\sim (Q^2/Q_0^2)^{a(x)}$ separately for the scaling violations of the sea- and valence-quark distributions (or for F_2 and F_3). No cut is imposed ensuring that only events outside the resonance region are considered. Both groups reference their results with respect to $Q_0^2 = 10\ GeV^2/c^2$. This means that for the low $x_{(Bj)}$ region very few events with a Q^2 value near the chosen Q_0^2 have ocurred, because the overall mean Q^2 is comparable to Q_0^2 and the mean Q^2 for a fixed $x_{(Bj)}$ decreases proportionally with $x_{(Bj)}$.

The results are (corrected) for the case of an isoscalar target, and we emphasised that they refer to the nucleons being probed while in a nuclear environment. For these reasons our results will not be directly comparable to those of the two experiments In addition the cuts on the data sample that we have used are different from those employed by the heavy target experiments, in particular our requirement on the invariant hadronic mass exceeding a minimum value of $W_{cut}^2 = 3.0\ GeV^2/c^2$.

The CHARM and FMM results are included in the figures by full and open circles, respectively. Despite the different kinematical region, nucleon environment and target isoscalarity, their $F_\pm$ are in fair agreement with our result, within the errors displayed. However, we can discern some different tendencies when our 'central' $x_{(Bj)}$ distributions are compared with the other results, particularly for the antineutrino case. The main difference is in the low $x_{(Bj)}$ region, where an implicit correction to a constant $Q^2 = 10GeV^2/c^2$ leads to about 50% larger values. This is expected from the known Q^2 dependence of the $x_{(Bj)}$ distributions, which is strongest at low $x_{(Bj)}$. The opposite situation occurs at large $x_{(Bj)}$, since due to our cut in W the minimum Q^2, and hence also the average Q^2, is larger than $10GeV^2/c^2$, as explained in chapter 5. Thus $F_\pm$ is smaller since the $dF_\pm/d\ln(Q^2/\Lambda^2)$ is negative at large $x_{(Bj)}$. Taking these considerations into account, we can state that our result for free protons agrees with the two existing measurements of the proton $x_{(Bj)}$ distribution using heavy targets, within the respective errors of the experiments.

Chapter 7

Conclusions

In the work presented here we have addressed the problem of extracting the neutral current $x_{(Bj)}$ distributions for neutrino and antineutrino scattering off protons that are not bound into a nucleus. We were faced with the immeasurability of the scaling variable $x_{(Bj)}$ which is the relevant piece of information about the momentum composition of the proton. Having identified the kinematical variable $w = p_T^2/(2p_L M_N)$, that depends on the hadronic three-momentum only, as a dimensionless ratio that can be reconstructed with sufficient resolution on average, we went on to show that it is related to the scaling variables by $w = x(1-y)$ in the Bjorken limit, that is in the kinematical region where $x_{(Bj)}$ can be associated with the momentum fraction (relative to the proton) of the scattered parton prior to the interaction.

It was then proven that it is possible to deduce information about the (anti)neutrino proton cross section $x_{(Bj)}$-dependence by measuring the w distributions and using the known helicity structure of the deep inelastic cross section, modified by the standard cuts. It turned out that with these cuts, which have to be imposed to ensure we are investigating the deep inelastic region, the conditional $y_{(Bj)}$-distributions for fixed $x_{(Bj)}$ are approximately independent of $x_{(Bj)}$. After we have developed a general model-independent relation between the $x_{(Bj)}$ and w distributions in form of an integral equation, this independence allowed an analytic solution for the $x_{(Bj)}$ distribution without any constraint about the form of the measured distribution in w. We illustrated the applicability of the method for small data samples, as well as the fact that in the limit of large statistics (which meant over 10000 events), it reproduces correctly the true $x_{(Bj)}$ dependence of the cross section. This proves that the assumption of *quasi*-independence of the conditional $y_{(Bj)}$ distributions is sufficient for the method to work.

The data collected with the BEBC hydrogen experiment in the two runs after the Internal Picket Fence had been installed has been analysed and we extracted a neutral current event sample. The high efficiency of muon detection by the External Muon Identifier in connection with the IPF, for muons with momenta above some 3 GeV, as well as the possibility to flag upstream hadronic activity in the event timeslot, enabled us to correct reliably for the inherent misclassifications and contaminations in the sample. The 3.5 T magnetic field yielded accurate momentum measurements which, together with the detailed optical information of the bubble chamber photos, are responsible for the sufficient resolution in the angle and transverse momentum of the hadronic system that includes reconstructed V^0's and a few γ conversions. We were thus able to measure the NC distribution in w and correct it, using the LUND fragmentation model and a detailed detector simulation, for the effects of resolution and the cuts imposed. The final corrected w distribution is obtained for the kinematical domain specified by $E_H = \nu + M_N \geq 7.5$ GeV and $W_{(H)} \geq 3.0\ GeV^2/c^2$, to remove the resonance region. Good agreement is found between the observed and the simulated w distributions.

The method developed in chapter 3 then allowed the $x_{(Bj)}$-dependence of the NC cross section on free protons to be determined, for the first time. We described the shape of the measured w distributions by simple one- and two-parameter functions, assuming a smooth behaviour on scales smaller than the resolution in w.

It has been shown that the results are stable with respect to the choice of different parametrisations. The resulting $x_{(Bj)}$ distributions agree within the errors with those expected on the grounds of parton universality. We thus find no indication of the proton momentum structure in weak neutral current scattering to be different from the charged current or electromagnetic case.

Our method did not assume any particular form of the cross section $y_{(Bj)}$-dependence, it was only required to be known within the kinematic region given by the cuts used, and to satisfy the conditon of quasi-independence on $x_{(Bj)}$. On the other hand, if we use the usual $y_{(Bj)}$-dependence that follows from the general principles of Lorentz-invariance and time-reversal symmetry, we are able to extablish a direct link between the NC structure functions and the w-dependence of the cross section. Since this functional relation is holding pointwise, one can obtain information about the NC structure functions for argument values equal to the measured w values. The w distribution grows fast for decreasing $w \rightarrow 0$, so that small arguments can be reached if the resolution in $\log w$ is sufficient. We also pointed out that, when seen in the parton framework, the relations obtained refer to parton distributions that are not weighted by the parton momentum fraction. The integral over the structure function F_3, for instance, is found to be related to the difference of the neutrino and antineutrino w distribution of cross section at the origin. It is noteworthy that these implications do not hold similarly for the charged current channel, and we traced this to the fact that the neutrino and antineutrino NC scattering are connected through crossing symmetry. Although the NC channel in deep inelastic scattering on protons and heavy targets has been harder to access than its CC equivalent so far, it can thus be argued that it seems to be worthy of further investigation.

Philosophy is such an impertinently litigious lady, that a man had as good be engaged in lawsuits, as have to do with her. I found it so formerly, and now I am no sooner come near her again, but she gives me warning.

(I. Newton to E. Halley, June 20, 1686)

Bibliography

[1] W. Pauli, letter to a meeting of radioactivity experts in Tübingen, December 4, 1930, repr. in 'W. Pauli, collected scientific papers', Eds. R. Kronig and V. Weisskopf, Vol.2, p. 1313, Interscience, New York 1964

[2] W. Pauli, letter to P. M. S. Blackett, April 19, 1933, repr. in 'Wolfgang Pauli, scientific correspondence', Eds. A. Hermann, K. von Meyenn, V. Weisskopf, Vol 2, P. 158, Springer, New York 1979

[3] E. Fermi, Ric. Scient. 4, p. 491, 1934;
E. Fermi, Nuov. Cim. 11, p. 1, 1934;
E. Fermi, Zeitschr. f. Phys. 88, p. 161, 1934.

[4] W. Heisenberg, Zeitschr. f. Phys. 77, p. 1, 1932; 78, P.156, 1932.

[5] H. Yukawa and S. Sakata, Proc. Phys. Math. Soc. Japan 17, p. 467, 1935.

[6] L. Alvarez, Phys. Rev. 54, p. 486, 1938.

[7] F. Reines and C. Cowan, Phys. Rev. 92, p. 830, 1953,
and C. Cowan et. al., Science 124, p. 103, 1956.

[8] C. S. Wu et. al., Phys. Rev. 105., p.1413. 1957.

[9] T. D. Lee and C. N. Yang, Phys. Rev. 104, p.254, 1956

[10] J. Sakurai, Nuovo Cim. 7, p.649, 1958.
E. C. G. Sudarshan and R. E. Marshak, Phys. Rev. 109, p. 1860, 1958;
M. Gell-Mann and R. P. Feynman, Phys. Rev. 109, p.193, 1958.

[11] S. S. Gershtein and I. B. Zel'dovich, Soviet.Phys. JETP 2, p.576, 1056

[12] C. N. Yang and R. L. Mills, Phys. Rev. 95, p. 631; 96, p. 191, 1954.

[13] M. Gell-Mann, Caltech. Report CTSL-20, 1961; Phys. Rev. 125, p. 1067, 1962; Phys. Lett. 8, p. 214, 1964
G. Zweig, CERN Report 8419/TH-401, 1964.

[14] S. L. Glashow, Nucl. Phys. 22, p.579, (1961)

[15] S. Weinberg, Phys Rev. Lett. 19, p.1264, (1967).
A. Salam, Proc. 8th Nobel Symp., p.367, ed. N. Svartholm (Almquist and Wiksell, Stockhom, 1968)
G. t'Hooft, Nucl. Phys. B33, p.173, (1971), B35, p.167, (1971)
S. L. Glashow, J. Iliopoulos and L. Maiani, Phys. Rev. D2, p.1285, (1970)
S. Weinberg, Phys. Rev. D5, p.1412, (1972)

[16] F. Dyson, Physics Today, June 1965

[17] P. W. Higgs, Phys. Lett. 12, p. 132, 1964, Phys. Rev. Lett. 13, p. 508, 1964; and Phys. Rev. 145, p. 1156, 1966;
F. Englert and R. Brout, Phys Rev. Lett. 13, p321, 1964;
T. W. B. Kibble, Phys. Rev. 155, p. 1554, 1967

[18] M. Kobayashi and T. Maskawa, Progr. Theor. Phys. 49, p. 652, 1973

[19] S. van der Meer, CERN/ISR-PO/772-31, 1972.
D. Möhl, G. Petrucci, L. Thorndahl and S. van der Meer, Phys. Rep 58, p. 83, 1980.

[20] UA1 collaboration, G. Arnison et. al., Phys. Lett. B122, p. 103, 1983;
UA2 collaboration, M. Banner et. al., Phys. Lett. B122, p. 476, 1983.

[21] R. P. Feynman, Phys Rev. Lett. 23, p. 1415, 1969
R. P. Feynman, Photon-Hadron Interactions, Benjamin 1972.

[22] R. L. Jaffe and C. H. Llewellyn Smith, Phys. Rev. D7, p.2506, 1973

[23] C. H. Llewellyn Smith, Phys. Rep. 3, p.262, 1972

[24] E. D. Bloom et. el.,Phys. Rev. Lett. 23, p. 930, 1969
M. Breidenbach et. al., Phys. Rev. Lett. 23, p.935, 1969

[25] F. J. Hasert et. al., Phys. Lett. 46B, p. 121, 1973;
F. J. Hasert et. al., Phys. Lett. 46B, p. 138, 1973;
G. Myatt, Proc. of the 6th Intnl. Symp. on Electron and Photon Interactions at High Energies 1973, ed. H. Rollnik and W. Pfeil, North Holland, p. 389, 1973.

[26] C. G. Callan and D. J. Gross, Phys. Rev. Lett. 21, p. 311, 1968

[27] M. Glück, E. Hoffmann and E. Reya, Z. Phys. C 13, p. 119, 1982.

[28] T. Eichten et. al., Phys. Lett. B46, p.274, 1973

[29] G. Horlitz, S. Wolff and G. Harigel, Nucl. Inst. Meth. 117, p. 115, 1974

[30] C. Brand et. al., Nucl. Inst. Meth. 136, p. 485, 1976
R. Beuselinck et. al., Nucl. Inst. Meth. 154, p. 445, 1978
C. Brand et. al., CERN/EF 77-3, 1977

[31] H. Foeth et. al., Nucl. Inst. Meth. A176, p.203, 1980
C. Brand et. al., CERN/EF 81-13, 1981 H. Foeth et. al., Nucl. Inst. Meth. A253, p. 245, 1987

[32] F. Bruyant, "GEOMPAM", CERN HYDRA Application Library (1974)

[33] H. Klein and L. Pape, "USBEMI", CERN HYDRA application library (1978)
H. Klein and L. Pape, "THIRA", CERN HYDRA application library (1978)

[34] S. J. Towers, Oxford D.Phil. thesis (1985)
E. Hoffmann et. al., "DCIDPICK V7.01", CERN HYDRA application library (1986)

[35] L. Pape, "KBASIC", CERN HYDRA application library (1976), modified by H. Klein and S. O'Neale (1986)

[36] G. Kellner and L. Pape, "EMIANA", CERN HYDRA application library (1980)
"SYNTH" program modified by E. Hoffmann, R. Jones and H. Klein (1986)

[37] G. Harigel (ed.), BEBC Users' Handbook, CERN 1979 and updates.

[38] H. M. Heijne, CERN/EF/BEAM 77-1, 1977
H. Burmeister, CERN/EP/NBU 79-9, 1979

[39] G. Myatt, Rep. Progr. Phys. 45 (1982) 1; L.M. Sehgal, in: Progr. in Particle and Nuclear Physics 14 (1985) 1.

[40] F. Jacquet and A. Blondel, in: Proc. of the Study of an *ep* Facility for Europe, DESY 79-48 (1979) 393.

[41] M. G. Bowler and S. L. Lloyd, Nucl. Inst. Meth. A240, p.300, 1985.

[42] CHARM Collab., M. Jonker et al., Phys. Lett. 128 B (1983) 117.

[43] CHARM Collab., J.V. Allaby et al., Phys. Lett. 213 B (1988) 554.

[44] V. Blobel, Lectures given at the 1984 CERN school of computing, DESY 84-118 (1984)

[45] G. Myatt, CERN report ECFA 72-4 vol. II (1972) 117.

[46] H.G. Heilmann, BEBC Hydrogen Collabn. intnl. report WA21-int-1 (1978).

[47] G. Ingelman: LUND Monte Carlo for Deep Inelastic Lepton Nucleon Scatterin, version 4.3, April 1983; T. Sjøstrand, Comp. Phys. Comm. 27 (1982) 243; B. Andersson et al., Z. Phys. C 1 (1979) 105; Z. Phys. C 3 (1980) 223; the LUND Monte Carlo has been adapted to the BEBC experiment WA21 by W. Wittek et al., Max-Planck-Institut für Physik und Astrophysik, München F.R.G. .

[48] H. P. Borner, Nucl. Inst. Meth. A293, p. 545, 1990;
H. P. Borner, BEBC Hydrogen Collabn., WA21 internal report, 1989.

[49] A. H. Mueller, Phys. Rev. D9, p. 963, (1974);
H. D. Politzer, Phys. Lett. 70B, p.430, (1977)

[50] R. K. Ellis, H. Georgi, M. Machacek, H. D. Politzer, G. G. Ross, Nucl. Phys. B152, 285, (1979)

[51] J. Feltesse, in: Proc. of the 1989 Intnl. Symp. on Lepton and Photon Interactions at High Energies, ed. M. Riordan, World Scientific 1990, p. 13, and references therein

[52] J. Morfin, W. K. Tung, Fermilab preprint Conf-89/26, and Proceedings of the 1988 Summer Study on HEP in the 1990s, Snowmass

[53] J. D. Bjorken, Phys. Rev. 179, p. 1547, (1969)

[54] F. E. Close, An Introduction to Quarks and Partons, p. 236, London: Academic Press (1979);
I. J. R. Aitchison and A. J. G. Hey, Gauge Theories in Particle Physics, Bristol and Philadelphia: Adam Hilger, 2nd ed. (1989)

[55] I. Hinchliffe and C. H. Llewellyn-Smith, Nucl. Phys. B128, p. 93, (1977)

[56] S. D. Conte, C. de Boor, Elementary Numerical Analysis, Mc Graw-Hill, (1981)

[57] CHARM Collabn., J. Allaby et al., Phys. Lett. B213, p.554, (1988);
FMM Collabn., F. E. Taylor, in: The Santa Fe (APS DPF) Meeting, 1984, ed. T Goldman and M. M. Nieto, World Scientific 1985, p. 263

[58] M. L. Goldberger and M. Gell-Mann, unpublished;
M. L. Goldberger, in Proc. of the 6th Annual Rochester Conf., 1956, ed. J. Ballam et. al., Interscience, N.Y., p. I-7;
D. I. Olive, Phys. Rev. 135, p. B745, 1964

[59] E. Byckling and K. Kajantie, 'Particle Kinematics', Wiley, London (1973), also in 'Review of Particle Properties', Phys. Lett. B204, (1988)

[60] H. P. Borner, to appear in the Proceedings to the 'Workshop on Hadron Structure Functions and Parton Distributions' (World Scientific), Fermilab, April 1990.

[61] B. Anderson et. al., Phys. Rep. 97, p,31, 1983.

[62] P. Allen et. al., Nucl. Phys. B214, p. 369, 1983;
H. Grässler et. al., Nucl. Phys. B223, p. 269, 1983;
G. T. Jones et. al., Z. Phys. C 25, p. 121, 1984;
G. T. Jones et. al., Z. Phys. C 27, p. 43, 1985.

[63] F. J. Hasert et. al., Phys. Lett. B46, p. 138, 1973

[64] S. Towers, Oxford D. Phil. thesis, 1985

[65] H. Foeth et. al., Nucl. Inst. Meth. A253, p. 245, 1987

[66] J. Mittendorfer, WA21 Collaboration Internal Report, 1984

[67] G Jones et. al., Z. Phys. C46, p. 25, 1990 E. Hoffmann, Ph. D. thesis Munich, 1989

[68] R. W. L. Jones, Ph. D. thesis Birmingham, 1988

[69] S. Burke, Ph. D. thesis London, 1988.

[70] M. Parker, Ph. D. thesis London, 1983.

[71] E. Hoffmann, Ph. D. thesis Munich, 1989.

[72] G. Jones et. al., WA21 collaboration, to be published

[73] BEBC Collaboration, J. Guy et. al., CERN/EP 89-76, 1989.

[74] EMC Collaboration, J. J. Aubert et. al., Phys. Lett. B123, p. 275, 1983; Nucl. Phys. B293, p. 740, 1987.

[75] FMM Collaboration, T. S. Mattison et. al., MIT preprint 1989;
T. S. Mattison, Ph.D. Thesis, MIT 1986

[76] CHARM Collabaration, M. Jonker et. al., Phys. Lett. B128, p. 117, 1983.

[77] P. N. Shotton, Oxford D. Phil. thesis, 1985

[78] BEBC WA21 and WA59 Collaborations, M. Aderholz et. el., Phys. Lett. B 173, p. 211, 1986
P. N. Shotton, W. Venus and H. Wachsmuth, CERN/EP/NBU 85-2

[79] P. Bosetti et. al., Phys. Lett. B 110, p. 167, 1982.